The University Of Sheffield.

Effects of mechanical properties of the environment on cell migration

Natasha Cowley

A thesis submitted in partial fulfilment of the requirements for the degree of Doctor of Philosophy

Department of Physics and Astronomy
Faculty of Science
The University of Sheffield

19th July 2021

Declaration of Authorship

I, Natasha Cowley, confirm that this thesis is my own work. I am aware of the University's Guidance on the Use of Unfair Means (www.sheffield.ac.uk/ssid/unfair-means). This work has not been previously been presented for an award at this, or any other, university.

Appendix B contains work presented in [1].

Signed: 

Date: 19/07/2021

THE UNIVERSITY OF SHEFFIELD

Abstract

Faculty of Science
Department of Physics and Astronomy

Doctor of Philosophy

Effects of mechanical properties of the environment on cell migration

by Natasha Cowley

Cell migration is central to many important biological processes such as wound healing and immune response. It is also prominent in many pathological processes such as cancer metastasis, vascular disease or osteoporosis. Migrating cells experience a wide variety of external environments. We investigate how mechanical properties of the external environment affect cell motility and behaviour. In particular we look at how rigidity and confining geometry play a role. We investigate the mechanical response of materials with different rigidities to cell generated forces.

We model a cell as a viscous droplet with an active contractile boundary analogous to the acto-myosin cortex. Using the immersed boundary method to numerically solve the model equations, we analyse the results in terms of hydrodynamic force moments. We show that a viscosity difference between the droplet and external fluid leads to shape changes and a reduced activity threshold for droplet motion.

We then explore the effects of confinement on an active droplet in a channel. We find that confinement changes the steady state shape of the droplet and reduces the translational velocity of the droplet. The act of confining a droplet in a channel greater than the diameter of the droplet can also lead to the onset of oscillatory swimming between the walls. We investigate this behaviour as a function of channel properties.

To investigate a deformable confining environment, we use two models, an elastic spring lattice and a neo-Hookean material. We use these to investigate the effects of environmental rigidity on droplet motion. We find that the deformability of the channel walls has an effect on droplet velocity and trajectory, and that wall deformation is inversely proportional to the deformation of the droplet. We also find that the stiffness of the external material affects whether droplets can pass through constrictions or not.

Our results have implications for cell migration in varied environments and the model we have developed will be of use in investigating this in specific biological contexts.

Acknowledgements

Undertaking a PhD, with what turned out to be undiagnosed ADHD, and writing my thesis during the pandemic has been a Sysiphean task. In the vein of, 'it takes a village...' so many people helped and supported me through the last few years, and I wouldn't have finished this thesis without them.

Firstly, I must thank my supervisor, Rhoda Hawkins, for her unwavering support and advocacy. I don't think this has been an easy process for either of us, I'm not sure many people could have got me over the finish line! I've really enjoyed working with Rhoda and I look forward to working with her again on future collaborations. Secondly, Carl Whitfield whose work provided a foundation for this project. He was also incredibly generous with his time, answering my questions towards the beginning of the project.

Thanks also to my office mates at various times in the PhD, Ian Estabrook, James Bradford, Jon Hall and Naruemon Rueangkham, for the PhD camaraderie and useful theoretical discussions. Extra thanks to Jon for reading through my thesis chapters.

Thanks to the University of Sheffield and EPSRC for my initial PhD funding, to EPSRC and Insigneo for additional funding. I would also like to acknowledge the CRUK project I was attached to and my colleagues on that for imparting their expertise on cancer biology.

Outside of academic acknowledgements I have had the support of an amazing group of friends: Ellie Dougherty, who always has time for me, even when she was writing up her own PhD thesis.

Jenny Hughes, Dawn 'Bob' Fletcher, Tom Pritchard, Mel Dando and Steve Woolass for 100s of dinners, lunches, coffees, venting sessions, supply of wine. There is not enough thanks I can give here, I would not have finished the PhD without them, and my life would be a lot more depressing. Extra thanks to Bob for proof reading large chunks of my thesis.

My parents, Fiona and Graham Cowley, have always supported me unconditionally in my life goals, and the PhD is no exception. They've had to listen to numerous phone calls of me stressing out about my project, my life, my career choices. They've also helped me financially at times which I am eternally grateful for.

Additionally the following people have been there for me during the pandemic and really helped get the thesis over the line: Tilda Graham, Alice Halsted, Sophie Hinchliffe, Jem Nash and Claire Patterson.

I would probably be remiss in not mentioning Sheffield Steel Roller Derby which provided a great stress outlet over the years and also introduced me to so many of the people who made this PhD possible.

Contents

Chapter 1

Introduction

In this chapter we provide a non-exhaustive overview of the biological systems relevent to this thesis. The project is concerned with the mechanical aspects of cell migration and the effect of the environment. This project was motivated by breast cancer metastasis and as such we provide an overview of the hallmarks of cancer cells and mechanical changes they undergo. We also detail some existing models for migrating cells.

1.1 Cell Biology

1.1.1 Cytoskeleton

The cytoskeleton is an internal structure within eukaryotic cells comprising of filamentous proteins, which form networks within the cell, along with numerous associated proteins, including regulatory proteins and motor proteins. The cytoskeleton has a number of roles within the cell but its main functions are transport and organisation of cell contents, and generating forces which control the motion and shape of the cell [2].

1.1.1.1 Actin

Actin is the most common protein in eukaryotic cells, comprising up to 5% of the total protein mass in non-muscle cells, and 10% in muscle cells [3]. Actin filaments are made up of monomers called G-actin (globular actin). These subunits join to make protofilaments which intertwine to give an actin filament known as F-actin. F-actin is polar in nature, consisting of barbed/plus end and the pointed/minus end. Though polymerisation and depolymerisation can occur from both ends, the net rate of polymerisation is higher at the barbed and and the net rate of depolymerisation is higher at the pointed end. When these rates are equal we have a situation known as 'treadmilling'.

Actin can form a wide variety of different structures, which have different functions within the cell. Branched actin networks and actin bundles can exert forces on the cell membrane, creating protrusions. Cortical (non-aligned) networks form below the cell membrane and is stressed in multiple directions, by contractile forces generated by myosin motors (introduced in 1.1.1.3), which bind to actin filaments. Stress fibres consist of an anti-parallel arrangement of actin fibres cross-linked with myosin and generate contractile forces used in many cell processes [2].

1.1.1.2 Other filaments

There are numerous other filaments in the cytoskeleton which we will briefly discuss although they are less relevant to cell migration than actin.

Microtubules are rigid filaments which are made of a dimer tublin. They generally comprise of 13 protofilaments forming a hollow tube. They are extremely dynamic and can quickly grow and shrink to explore space. They generally have one end attached to the centrosome and are involved in mitosis as well as intracellular transport [4].

Intermediate filaments are a diverse family of filaments in the cytoskeleton. Their in the cell is not entirely clear [5], although they seem to assemble as a response to mechanical stress [6]. Intermediate filaments are less stiff than actin or microtubles and have a shorter persistence length [7]. They are also apolar, unlike the other filaments in the cytoskeleton and have no associated motor proteins. Intermediate filaments are hierarchical in structure and the most complex cytoskeletal filaments in terms of assembly [8]. Some common types of intermediate filaments found in cells are vimentin and cytokeratin and nuclear lamins. Recent work shows that they play a larger role in migration than previously thought. This is largely in modulating forces within the cell. Intermediate filament networks can help control the distribution of forces in the cell and act protectively, for example preventing damaging deformation of the nucleus. Intermediate filaments also regulate key processes in focal adhesions which are crucial for some modes of migration [9].

1.1.1.3 Motors

There are 3 types of cytoskeletal molecular motors: myosins, which walk along actin filaments, and kinesins and dyneins which move along microtubules. These motor proteins convert chemical energy into mechanical forces by the hydrolysis of ATP (adenosine triphosphate) which induces a conformational change in the protein complex. Motors can also be classified by their type of motion. Processive motors are motors which remain attached to the filament for a long time before detaching, and non-processive motors which remain connected for a much shorter time, generally one 'step'. Processive motors tend to work individually while non-processive ones tend to work in teams [10].

Although there are a whole family of myosin motors, from here on in we will focus on myosin II. Myosin II motors have a tail and 2 heads which bind to actin filaments [4]. They move along an actin filament towards the plus end [10]. Single myosin II motors are non-processive and will detatch after a step. In the cytoskeleton several myosins will bind together into mini-filaments which act processively .

1.1.1.4 The cortex

We are interested in the cell cortex as it plays an important role in cell morphology. This is important for processes such as differentiation, mitosis and cell migration [11].

The acto-myosin cortex is an isotropic disordered structure located just below the cell membrane. It's thickness is dependent on cell state, but has been measured to be roughly 200 nm [12]. For short timescales the cortex behaves as an elastic shell, but due to polymerisation and depolymerisation in the actin network along with transient crosslinks, for longer timescales it behaves like a viscous fluid. For reference, it takes about a minute for all the cortical actin to turn over [13].

Myosin motors attached to the actin network generate tension in the cortex through contractile forces. Gradients in cortex tension are what lead to shape changes and to cortical flows, which are important for cell migration.

1.1.2 Active Processes in Cells

Active matter is a vast area of study which includes a wide variety of non-equilibrium condensed systems. They are characterised by self-driven units which consume energy at a local level converting it to forces, collectively generating coordinated motion [14]. The cytoskeleton contains many active processes related to cell motility, most importantly actin polymerisation and acto-myosin contraction.

1.1.2.1 Actin polymerisation and force generation

G-actin contains one monomer of ATP. When it binds with the F-actin filament the ATP is hydrolysed, releasing energy and an inorganic phosphate,leaving an F-actin bound ADP (adenosine diphosphate)[15]:

$$\mathrm{ATP} + \mathrm{H_2O} \rightleftharpoons \mathrm{ADP} + \mathrm{P_i} + \mathrm{H^+} \tag{1.1}$$

ATP hydrolysis modulates the filament's dynamics as well as the binding affinity of several actin associated filaments [16].When a G-actin depolymerises from the filament, its ADP doesn't recombine with a free phosphate, rather it exchanges it for an ATP in solution. Thus actin is constantly consuming ATP and is an ATPase.

Actin networks can generate forces via polymerisation, this is believed to be responsible for the membrane protrusions in the initial stages of cell motion [17]. Many theories have been proposed to explain the mechanism of force generation by polymerisation. The model which fits best with experimental evidence is the elastic Brownian ratchet proposed by Peskin [18] and developed by Mogilner and Oster [19].

In the elastic Brownian ratchet mechanism an actin filament is modelled as a polymerising elastic rod. As the the rod polymerises it's Brownian motion impinges on the membrane exerting a force. In order to add a monomer to the tip a gap of $\delta \cos\theta$ must be created by thermal fluctuations between the tip and the membrane. Where δ is half the size of an actin monomer and θ is the angle of approach of the filament to the membrane. A monomer can then diffuse into this gap to extend the filament.

1.1.2.2 Motor-filament contraction

Contractility of actin-myosin networks is a consequence of stresses actively generated by myosin motors [20]. It has been demonstrated *in vitro* that disordered actin bundles can contract from just the addition of myosin and ATP [21]. While there has been some success in describing contraction in the cytoskeleton using continuum hydrodynamics such as modelling it as active polar gel, the precise mechanism at the microscopic level is still unclear, however models have been proposed.

Myosin can cause relative sliding between actin filaments. As actin is a polar filament, the relative orientation of the filaments in the network affects the degree of sliding. The polarity of the actin filaments dictates the direction of forces exerted by molecular motors on the filament [22]. Kruse and Jülicher [23] look at active filament bundles as a minimal, one-dimensional model of contraction. Stress fibres contain filament bundles and generate contractile forces [4]. They consist of a bundle of aligned polar filaments connected by active cross-links which are mobile and create relative forces between the filaments. In the model [23], pairs of hard rods are connected by a

motor which translates to the plus end of each filament. This results in relative sliding of the rods for anti-parallel bundles (figure 1.1 (a)). In this situation they are equally likely to contract or extend. For polar bundles (figure 1.1 (b)), shows that, assuming motors take longer to detach from filament tips, the rods undergo relative contraction creating an active tension in the bundle.

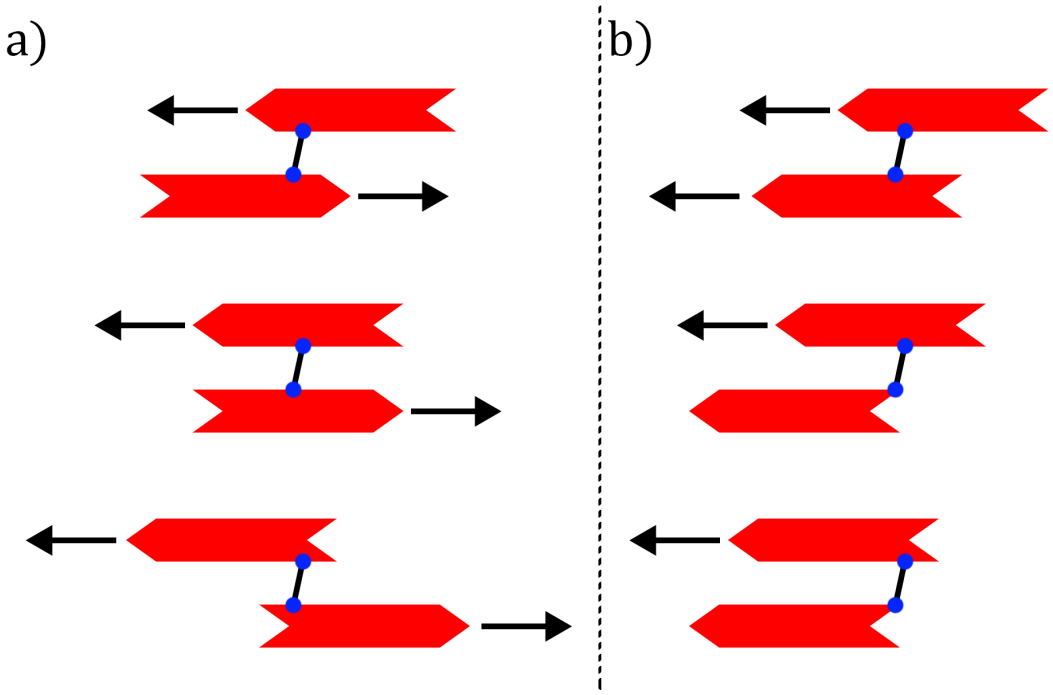

FIGURE 1.1: Possible configurations of relative sliding filaments by motor proteins (a) anti-parallel filaments and (b) parallel filaments. The forces from motors exerted on filaments are indicated by the black arrows. In (a) if the motor is bound long enough the filaments will slide past each other until their plus ends are together. In (b) the plus ends can be brought together if the motor remains bound to the filament plus end.

It was proposed by Carlsson [24] that if filaments were treadmilling the anti-parallel configuration in figure 1.1(a) could be maintained. Furthermore as net polymerisation will occur at the plus end, on average the filaments will move closer rather than further away from each other, resulting in a contraction.

Lenz et al. [25] propose a mechanism for contractility in anti-parallel organised filaments. In order to break the symmetry between the likelihood of contraction vs extension, they model anti-parallel bundles attached by a combination of fast and slow motors. These motors induce stresses within each bundle, when a fast motor is behind a slower motor this causes compression, the opposite causes tension. Actin responds non-linearly and buckles under compression but resists extension. This breaks the contractile extensile symmetry [26]. Liverpool et al. [27] and Hawkins et al. [28] propose a similar model, without buckling. Anti-parallel filaments can be thought of as two linear springs in series. The section in front of the motor towards the plus end of each filament will experience compression, and the section behind will experience extension. The elastic constant of the filament bundle is symmetric, but due to motor

stepping the lengths of the sections are different. This causes an effective difference in spring constant. This leads to an over all contraction in the bundle.

Contractility in disordered actin networks and networks with no orientational order, e.g. the cell cortex, has been observed [29]–[31]. Actin filaments have non-linear, force dependant elasticity. Applying non-linear elasticity to computer models in 3D [32], over all contraction of the network is observed in line with experimental results [20].

1.1.2.3 Active polar gel model for acto-myosin networks

The cytoskeleton can be considered as an active elastic polymer gel for short time scales and an active liquid crystal for longer ones [33], [34], [35]. Where length scales are larger than the mesh size of the gel and the relevant time scales are longer than the conformational relaxation time for actin, a hydrodynamic theory can be developed [35]. On this macroscopic scale the precise mechanisms underlying ATP consumption and network dynamics do not need to be considered. Using Onsager relations, which characterise a linear response close to equilibrium, Kruse et. al outline the derivation of the constitutive equations for this system [36], [37]. The fluxes in the system are found and their conjugate forces and the fluxes are expanded to linear order in terms of the forces. For this system there are 3 pairs of fluxes and forces: symmetric stress, σ_{ij} and the strain rate u_{ij}, the rate of change of polarisation $\dot{\vec{p}}$ and the molecular field $\vec{h}$, and the rate of consumption of ATP, r and the chemical potential of the hydrolysis a molecule of ATP, $\Delta\mu$.

Actin filaments are polar and can be described as semi-flexible polymers for cell length scales. The polarity of these networks can be described by a polarisation field, $\vec{p}$ which gives the local orientation of the filaments. The motion of the gel is described by the strain rate tensor, $u_{ij} = \frac{1}{2}(\partial_i v_j + \partial_j v_i)$ where v_i is the velocity field. The free energy of polarisation is given by the Frank free energy for a polar nematic liquid crystal [33] [34].

$$F_p = \int d\vec{r}\left[\frac{K_1}{2}(\nabla.\vec{p})^2 + \frac{K_2}{2}[\vec{p}\cdot(\nabla\times\vec{p})]^2 + \frac{K_3}{2}[\vec{p}\times(\nabla\times\vec{p})]^2 + k\nabla\cdot\vec{p} - \frac{1}{2}h^0_{||}\vec{p}^2\right] \tag{1.2}$$

The first 3 terms correspond to splay, twist and bend deformations and K_i are positive constants. Often the twist term is neglected when modeling the actomyosin cortex as it is very thin and can be considered as a quasi two-dimensional system. k is a coefficient which describes spontaneous splay dictated by the symmetry of the polarisation field, $h^0_{||}$ is a Lagrange multiplier which ensures the polarisation is a unit vector. In the one-constant approximation$K_1 = K_3 = K$.
The molecular (or orientational) field $\vec{h}$ is the field conjugate to $\vec{p}$ and is defined as:

$$\vec{h} = -\frac{\delta F_p}{\delta \vec{p}} \tag{1.3}$$

From conservation laws (density and momentum are the two conserved quantities in an active gel), the entropy production rate, $\dot{S}$ can be written as:

$$T\dot{S} = -\frac{dF}{dt} = \int d\vec{r}\sigma_{ik}u_{kj} + P_i h_i + r\Delta\mu \tag{1.4}$$

From equation (1.4) using the Onsager approach the following general constitutive equations can be written.
The first equation,

$$2\eta u_{ij} = \left(1 + \tau\frac{D}{Dt}\right)\left\{\sigma_{ij} + \zeta\Delta\mu\left(p_i p_j - \frac{1}{3}p^2\delta_{ij}\right) + \tau A_{ij} - \frac{\nu_1}{2}\left(p_i h_j + p_j h_i - \frac{2}{3}h_k p_k \delta_{ij}\right)\right\} \tag{1.5}$$

which relates the strain rate to the stress, must respect the symmetries of a polar gel, as well as time reversal symmetry which allows the distinction between dissipative (associated with energy dissipation) and reactive (elastic) components of the flux. The dynamics of the convected Maxwell model are used, however to ensure rotational and translational invariance the co-rotational time derivative is used:

$$\frac{D}{Dt}\sigma_{ij} = \left(\frac{\partial}{\partial t} + v_k\frac{\partial}{\partial r_k}\right)\sigma_{ij} + [\omega_{ik}\sigma_{kj} + \omega_{jk}\sigma ki], \tag{1.6}$$

ω is the vorticity tensor, $w_{ij} = \frac{1}{2}(\partial_i v_j - \partial_j v_i)$. Only one viscoelastic relaxation time, τ is used although experiments have shown that the cytoskeleton may contain a broad distribution of relaxation times [38], here τ is the longest relaxation time in the system. The tensor A_{ij} describes reactive non-linear terms to the lowest order derived from the geometry of the flow field common to non-linear viscoeleastic models [39]. σ_{ij} is the symmetric part of the stress tensor and η is the shear viscosity. The other reactive parameters are ν_1 which couples the polarisation and stress, describing the polarisation in a shear flow, and ζ which couples the activity in the gel with the stress. The sign of ζ determines whether the stress is contractile or extensile. It has been seen experimentally that the internal stresses in the actin cytoskeleton are contractile so a negative sign is imposed.

The second constitutive equation,

$$\frac{Dp_i}{Dt} = \frac{1}{\gamma_1}\left(1 + \tau\frac{D}{Dt}\right)h_i + \lambda_1 p_i\Delta\mu - \nu_1 u_{ij}p_j + \bar{\nu}_1 u_{kk}p_i, \tag{1.7}$$

concerns the rate of change of polarisation $\dot{\vec{p}} = D\vec{p}/Dt$ where again the co-rotational derivative is used. Here γ_1 is the rotational viscosity which describes the dissipation due to rotation of polarisation. $\bar{\nu}_1$ gives the polarisation in a compressional flow rather than a shear flow. λ_1 characterises an active term which if positive tends to align the filaments.

Finally the last equation,

$$r = \Lambda\Delta\mu + \zeta p_i p_j v_{ij} + \bar{\zeta}v_{ii} + \lambda_1 p_i h_i \tag{1.8}$$

gives the rate of consumption of ATP.

1.1.3 Extracellular Matrix

The extracellular matrix (ECM) exists outside cells in the body. The ECM is extremely varied in composition across different tissues of the body, depending on their function. For example the ECM of bone can be calcified. While the ECM is highly variable between tissues, there exist common conserved elements. The matrix part of the ECM consists of 2 main classes of molecule, glycosaminoglycans (GAGs) which are polysaccharide chains and fibrous proteins. The fibrous proteins are embedded in the GAGs which form a hydrated gel-like substance [4].

1.1.3.1 Glycosaminoglycans

GAGs are long polysaccharide chains which are extremely hydrophilic. With the exception of hyaluronic acid these chains are attached to a protein core, forming proteoglycans. Their extended form and polar nature are key to forming hydrogels and for the embedded protein matrix to withstand large compression [40].

1.1.3.2 Fibrous proteins

The mechanical properties of the ECM are particularly determined by the amount and types of protein present in the matrix, especially collagen and elastin [41]. Collagen I is the most common type of collagen and most abundant in the ECM. Collagen I forms into fibrils, which vary widely in diameter but are ~ 100 nm. These collagen fibrils form into a crosslinked network [42].

Other fibrous proteins found in the ECM are, elastin, which helps stretched tissues recoil, and fibronectin which is involved in ECM organisation and mediades cell attachments [40].

1.1.4 Breast cancer cells

Cancer cells arise from mutations in DNA of cells in normal tissue. Their abnormal behaviour derives from these mutations and altered patterns of gene expression [43]. Most cancers arise from epithelial tissue (these are classed as carcinomas). What is called breast cancer most commonly originates from secretory epithelial cells, forming an adenocarcinoma. Tumours can be benign meaning they are localised and non invasive, or malignant meaning they are invasive and metastatic. Nearly all deaths from cancer are a result of metastatic tumours [44].

Metastatic secondary tumours are formed when cancer cells break off from the primary tumour and travel through the blood vessels or lymphatic system to colonise new sites. Breast cancer is a type of cancer very prone to metastasis, and frequently colonises bone tissue [45]. The series of events leading to secondary tumour fomation is called the invasion-metastasis cascade, and has six steps [44].

1. Localised invasion, where carcinoma cells breach the basement membrane.
2. Intravasion, where cells enter the the blood vessels or lymphatic system.
3. Transport through this system.
4. Extravasion, cells exiting the vessels into the tissue.
5. Formation of dormant micrometastases.
6. Colonisation, where some of the dormant micrometastases acquire the ability to

form macroscopic metastases.

To acquire motility epithelial cells must reduce their adhesion to the basement membrane and attachments to neighbouring cells, as well as shedding many of their epithelial phenotypes. This happens by a process known as the epithelial mesenchymal transition (EMT). This process is also seen in wound healing and during embryogenesis. Mesenchymal cells are cells which embryologially derive from the mesoderm. Under EMT epithelial cells acquire phenotypes of mesenchymal cells [44].

During EMT many changes occur. Primarily cells become more invasive and motile, losing cell polarity and gaining a fibroblast-like spindly shape. There is a decrease in expression of E-cadherin, which is a transmembrane protein that forms attachments with neighbouring cells. Decrease in E-cadherin seems to increase the invasiveness of cells, while experimentally re-expressing it in invasive tumour cells has been shown to suppress invasiveness [46]. In EMT E-cadherin is replaced by N-cadherin which forms weaker cell-cell attachments, assisting cell motility. Metastatic cells will also have a reduced expression of keratin (an intermediate filament family) and an increase in vimentin (a different family of intermediate filaments). Vimentin expression correlates with invasive phenotypes of epithelial cancers [47], and can promote motility even in the presence of E-cadherin [48]. Furthermore, cells without keratin demonstrate more invasiveness and are around 60 % more deformable than those with keratin [49]. Cells which undergo EMT also express a variety of other proteins associated with mesenchymal cells, including proteases which can degrade extracellular matrix proteins assisting motion [50].

Cancer cells can also undergo mesenchymal-amoeboid transition which is an environmentally stimulated transition in migration type. Unlike EMT this is a rapid reactionary change to the surrounding environment [51] we discuss these types of migration further in section 1.2

The mechanisms governing the metastasis and invasiveness of cancer cells are incredibly complex and not yet fully understood. However it is clear that mechanical properties of cancer cells are involved in their migration.

1.2 Cell Migration

Cell migration plays a vital role in many processes within the body. From gastrulation and the development of the nervous system in embryogenesis, to wound healing and inflammatory response in adults. It is also prominent in many pathological processes such as cancer metastasis, vascular disease or osteoporosis. Consequently understanding cell migration is vital to developing treatments.

1.2.1 Migration in 2D

There are 3 key steps for cell motion on a substrate:

1. *Protrusion*, driven by actin polymerisation.
2. *Adhesion*, formation of focal contacts with the substrate.
3. *Retraction*, adhesions are released and the rear retracts. [4].

Cells moving on a substrate exhibit a crawling type motion. Initially the cell will polarise, inducing a clear spatial asymmetry between the front and the rear of the cell. This has been observed happening spontaneously in experiments, however cells may also respond to gradients of chemotractants or other microscopic non-uniformities [52]. Cells extend protrusions, generally sheet-like lamellipodia or finger-like filopodia, in the direction of motion. These projections of the membrane are very actin rich and thought to be driven by actin polymerisation [17].
Focal adhesions connect the actin cortex and stress fibres to the substrate allowing the cell to generate traction. Contractile forces generated by myosin translocate the cell body forwards and the rear adhesions are broken allowing the cell to move forwards[52].

1.2.2 Migration in 3D

While cell motility is often studied on rigid, flat substrates, in vivo cells commonly move in more complex and confined geometries. In confinement in the cellular environment or extracellular matrix proteins, or in embedded in gels, mechanisms of motion differ [53]. In 3D confinement specific adhesion to the environment becomes less important and we see that cells can move without adhesion [54].

The two main types of migration in 3D are mesenchymal and amoeboid migration [55]. The type of migration undertaken by the cell is highly dependent on the surrounding environment and a cell can switch rapidly between migration strategies. Perhaps the most obvious difference between these modes is that mesenchymal migration is highly dependant on focal adhesions where as amoeboid motion can occur independently of any specific adhesion.

1.2.2.1 Mesenchymal migration

Mesenchymal migration makes use of focal adhesions and protrusions from the leading edge of the cell. This mode of migration is most reminiscent of the crawling type migration of cells on 2d surfaces. Mesenchymally migrating cells tend to be elongated along the axis of migration, and actin stress fibres within the cell tend to align with the fibres in the ECM. These cells often remodel the ECM using matrix metalloproteinases (MMPs) which degrade the collagen matrix. In terms of intracellular organisation, mesenchymal cells tend to have the nucleus behind the microtubule organising centre (MTOC) and many of the organelles. The relative position of the nucleus and MTOC is often used as a measure of cell polarity, although it's not yet known what controls this order. Mesenchymal cells having the MTOC towards the front of the cell allows for better control of the proteolytic processes degrading the matrix [55].

1.2.2.2 Amoeboid Migration

This is the type of migration we will be exploring in this thesis. It is characterised by a rounded cell shape and low adhesion with the surrounding. Unlike mesenchymal cells, cells which move using amoeboid migration do not degrade the matrix and instead deform and move through existing gaps in the ECM. They also do not tend to form focal adhesions with the substrate. Also differently to mesenchymal migration, in amoeboid cell the nucleus is located in front of the MTOC [55].
As amoeboid cells do not use focal adhesions to move another mechanism is required. Acto-myosin contraction at the rear of the cell induces a flow in the cortex to the rear of the cell [56]. This propels the cell forwards as a consequence of friction with the confining environment [57], [58].

1.2.2.3 Other migration modes

Lobopoial motion has elements of both amoeboid and mesenchymal migration [59]. Difference in intracellular pressure creates a leading edge protrusion called a lobopodia. Concurrently, the cell adheres to and pulls on the ECM. Nuclear pistoning is used to generate pressure at the front of the cell [55].

Another observed method of migration is 'chimneying' [54]. This is where highly confined cells push outwards against the confining medium, building up friction allowing the cell to then protrude forwards. Hawkins et al. [60] propose a mechanism, independent of myosin contractility, where polymerisation against the cell membrane, leads to a build up of viscous friction against the channel wall and a dense region at the rear of the cell, corresponding to the uropod prevents retrograde flow. These elements combined lead to motion.

Some specific cells have swimming specific structures like flagella which drive the cell, this is beyond the scope of this thesis.

1.2.2.4 Switching between modes

The largest determining factors of the mode of migration a cell uses are the amount of confinement it is under and the ability of the cell to adhere to the environment. Additionally, changes to the cells themselves can also trigger a change in migratory behaviours. For example, inhibiting MMPs triggers the cell to adopt an amoeboid strategy[55].

Determinants of motion can be categorised into properties of the cell and properties of the surrounding environment. Cell based factors which favour amoeboid migration are a lack of functioning integrins, as this precludes the cell from using focal adhesions [54]. Other cell properties which can trigger a switch to amoeboid motion are increased myosin contractility in the cortex [61], and the inhibition of proteases [55]. For external factors, the biggest trigger away from mesenchymal motion is the strong confinement of a cell. Cells confined by a material which is difficult to adhere to also triggers a switch to amoeboid motion. The elastic response of the environment may also affect the mode of migration. For example cells have been seen to migrate lobobodially when there was a linear relationship between ECM deformation and applied stress, but switched to a lamellipodial mesenchymal mode when the response becomes non-linear [59].

1.2.3 Swimming Cell migration

For swimmers in the low Reynolds number regime, where viscous forces dominate, the migration mechanism must break time-reversal symmetry to move, this is due to the lack of time dependence in the Stokes equations. This is known as the Scallop theorem [62]. Objects swimming in this regime must also be constantly generating propulsion forces to maintain motion.

1.2.3.1 Squirmers

This model was introduced by Lighthill in 1952 as a simple model for a swimming sphere [63]. A spherical particle undergoes small amplitude oscillations at it's surface either radial or tangential. Assuming axisymmetry, the Stokes equations are solved, using Lamb's general solution for Stokes flow[64], with prescribed boundary conditions to capture the surface oscillations [65]:

$$v_r(R,\theta,t) = \sum_{n=0}^{\infty} A_n(t) P_n(\cos\theta) \tag{1.9}$$

$$v_\theta(R,\theta,t) = \sum_{n=1}^{\infty} B_n(t) V_n(\theta) \tag{1.10}$$

Here R is the radius of the sphere, A_n and B_n are coefficients which are a fucntion of time, $P_n(\cos\theta)$ are Legendre polynomials and V_n is defined as:

$$V_n = \frac{2}{n(n+1)} \frac{\partial P_n(\cos\theta)}{\partial \theta} \tag{1.11}$$

The full solution in the reference frame of the sphere is[63]:

$$v_r = A_0 \frac{R^2}{r^2} + \frac{2}{3}(A_1 + B_1)\frac{R^3}{r^3} P_1 + \sum_{n=2}^{\infty} \left(n \frac{R^n}{2r^n} - \left(\frac{n}{2} - 1\right) \frac{R^{n+2}}{r^{n+2}} \right) A_n P_n \tag{1.12}$$

$$v_\theta = \frac{1}{3}(A_1 + B_1)\frac{R^3}{r^3} V_1 + \sum_{n=2}^{\infty} \left(n \frac{R^{n+2}}{2r^{n+2}} - \left(\frac{n}{2} - 1\right) \frac{R^n}{r^n} \right) B_n V_n \tag{1.13}$$

Where $P_n = P_n(\cos\theta)$ and $V_n = V_n(\theta)$.

Squirmers are classified into pushers and pullers. A parameter known as the squirming parameter, β is defined:

$$\beta = \frac{B_2}{|B_1|} \tag{1.14}$$

where B_1 and B_2 are coefficients of the tangential velocity of the sphere, V_θ at the surface, R. The Stokes flow singularity associated with B_1 is the source dipole, which is relevant to translational motion, and B_2 is associated with the force dipole[66]. If β is positive the droplet is a puller, if β is negative the droplet is a pusher, and is $\beta = 0$ then the droplet is a neutral squirmer. Another definition of a pusher or a puller is from the sign of the force dipole, negative for puller and positive for pushers [65].

1.2.4 Active droplets

There have been numerous models of active droplets to model cell migration. The active nature of the droplet changes between models. Some model a cell as a droplet of active polar gel, as described in section 1.1.2.3: [67], [68],[69] or active nematic gels [70],[71]. Another approach is to model just the cortex using active gel theory, with passive internal fluid. Here myosin can diffuse on and off the boundary and is also advected with cortical flow [58], [72], [73].

There are parallels between active shell/boundary models of cell migration and

Marangoni droplets. Marangoni droplets are droplets which are propelled by a gradient in surface tension. The surface gradient here is mediated by surfactants at the interface of a droplet[74]. The flow field of such a droplet can be mapped onto that of a squirmer [75]. Most models assume a spherical droplet, but some have studied the deformation for this model of an active droplet [76] finding that droplets did deform away from a sphere, and that pusher droplets deform perpendicularly to the axis of motion. In [77] they find that for droplets more viscous than their surrounding medium, motility is enhanced.

In chapter 2 we introduce our model of an active droplet for an amoeboid migrating cell. We explore the effects of a viscosity difference between the internal and external fluid on the droplet shape and velocity. In chapter 3 we look at the effects of confinement by placing the active droplet in no-slip channels of varying width. In chapter 4 we look at how the geometry and deformability of our confining medium changes droplet migration.

Chapter 2

Characterising the motion of an active droplet in viscous fluid

We consider the case of a cell moving in a viscous fluid. We will introduce our model for a migrating cell as an active viscous droplet and investigate how changing the external and internal viscosities of the fluids affects droplet shape and velocity.

2.1 Model for Amoeboid Cell Migration

Cells are highly adaptable in their migration strategies, as discussed in section 1.2, utilising various different modes depending on the situation they are in. We are interested in the amoeboid mode of migration which is often observed in highly confined geometries [55] and is characterised by rounded cell shape, low adhesion with surroundings and is generally driven by acto-myosin contraction. We first investigate amoeboid migration in an unconfined state, before looking at the effects of confinement in chapters 3 and 4.

Building on the work of Whitfield and Hawkins [72], we model the cell as a viscous droplet with an active boundary which is analogous to the cell cortex. The dominant mechanical properties of the cell come from the cytoskeleton [2], which is viscoelastic in nature. Actin filaments can be thought of as polar rods and the cortex has been observed to be isotropic [13]. As we are concerned with length scales much larger than the average mesh size of the actin cytoskeleton, we treat the cytoskeleton as an isotropic liquid crystal. The time scales we are interested in are long compared to the conformational relaxation time of actin, we treat the cytoskeleton as a viscous fluid [35]. As our simulations and calculations are in 2D the liquid crystal assumption is irrelevant as the cortex in our model reduces to a 1D boundary. We are in the low Reynolds number regime as we are working at the micrometre length scale, with large viscosities, so our system is governed by the Stokes Equations:

$$\eta \nabla^2 \vec{v} = \nabla P - \vec{f} \tag{2.1}$$

$$\nabla \cdot \vec{v} = 0 \tag{2.2}$$

Where $\vec{v}$ is the fluid velocity, P is the pressure, $\vec{f}$ is the force density, and η is the dynamic viscosity.

We model the cell cortex as active liquid crystal dispersed on the droplet interface. In the 2D case this reduces to a concentration, $c(\vec{s})$ of active particles on a 1D boundary, where $\vec{s}$ is the coordinate along the boundary. The concentration of active particles is governed by an advection diffusion equation:

$$\frac{\partial c}{\partial t} = -\frac{\partial}{\partial s}(c\vec{V}) + D\frac{\partial^2 c}{\partial s^2} \tag{2.3}$$

Where $\vec{V} = \vec{v}(R, \theta)$ is the fluid velocity at the boundary and D is the diffusion constant along the interface. These active particles locally modify the tension, γ of the droplet:

$$\gamma = \gamma_0 - \widetilde{\zeta\Delta\mu} c(\vec{s}) \tag{2.4}$$

where γ_0 is the bare tension of the boundary and $\widetilde{\zeta\Delta\mu}$ is the effective activity, which is negative for the contractile case which we consider. This gives rise to gradients in surface tension which induce flow and propel the droplet in a 'force free' fashion. This is the same mechanism by which surfactants on droplets reduce local surface tension generating Marangoni flows propelling the droplet [78]. The force density on the boundary $\vec{F}$ is given by:

$$\vec{F} = \partial_s(\gamma\hat{\vec{\tau}}) \tag{2.5}$$

Where $\hat{\vec{\tau}}$ is the tangent unit vector to the boundary.

We implement velocity and stress boundary conditions where velocity is continuous across the boundary, and the stress condition is the force balance between the boundary force and hydrodynamic forces:

$$\vec{v}^{(int)} = \vec{v}^{(ext)}|_{r=R} \tag{2.6}$$

$$(\sigma_{ij}^{(int)} - \sigma_{ij}^{(ext)})n_j = F_i|_{r=R} \tag{2.7}$$

For the stress tensor: $\sigma_{ij} = 2\eta u_{ij} - P\delta_{ij}$, where u_{ij} is the strain rate tensor. The viscosity inside the droplet is denoted as $\eta^{(int)}$ and outside as $\eta^{(ext)}$.
The equation of motion for the boundary is given by:

$$\frac{\partial \vec{R}}{\partial t} = \vec{V} \tag{2.8}$$

2.1.1 Linear stability analysis

We perform a linear stability analysis around the homogeneous solution for the droplet, when the concentration is uniform, $c = c_0$ and the radius is constant $R = R_0$. Here we use the 2D version of Lamb's solutions for a fluid droplet [79]:

$$v_r = \begin{cases} \sum_{k=1}^{\infty} \left(\hat{\alpha}_k r^{k+1} + \hat{\beta}_k r^{k-1} \right) e^{ik\theta}, & \text{if } r < R_0 \\ \sum_{k=1}^{\infty} \left(\alpha_k r^{-k+1} + \beta_k r^{-k-1} \right) e^{ik\theta}, & \text{if } r > R_0 \end{cases} \tag{2.9}$$

$$v_\theta = \begin{cases} i \sum_{k=1}^{\infty} \left((k+2)\hat{\alpha}_k r^{k+1} + k\hat{\beta}_k r^{k-1} \right) \frac{e^{ik\theta}}{k}, & \text{if } r < R_0 \\ i \sum_{k=1}^{\infty} \left((k-2)\alpha_k r^{-k+1} + k\beta_k r^{-k-1} \right) \frac{e^{ik\theta}}{k}, & \text{if } r > R_0 \end{cases} \tag{2.10}$$

$$P = \begin{cases} \hat{P}_0 + 4\hat{\eta} \sum_{k=1}^{\infty} (k+1)\hat{\alpha}_k r^k \frac{e^{ik\theta}}{k}, & \text{if } r < R_0 \\ P_0 + 4\eta \sum_{k=1}^{\infty} (k-1)\alpha_k r^{-k} \frac{e^{ik\theta}}{k}, & \text{if } r > R_0 \end{cases} \tag{2.11}$$

We apply the perturbations of the form $g = g_0 + \delta g_k(t) e^{ik\theta}$, where $\delta g_k(t) = \delta g_k e^{st}$, and solve to linear order using boundary conditions (2.6) and (2.7) to find the values for constants $\hat{\alpha}, \hat{\beta}, \alpha$ and β, the hat, here, signifying that a quantity is inside the droplet.

$$\hat{\alpha} = -k \frac{(\widetilde{\zeta\Delta\mu} R_0 \delta c_k - (k-1)(\gamma_0 - c_0 \widetilde{\zeta\Delta\mu})\delta R_k)}{4R_0^{k+2}(\hat{\eta} + \eta)} \tag{2.12}$$

$$\hat{\beta} = k \frac{(\widetilde{\zeta\Delta\mu} R_0 \delta c_k - (k+1)(\gamma_0 - c_0 \widetilde{\zeta\Delta\mu})\delta R_k)}{4R_0^{k}(\hat{\eta} + \eta)} \tag{2.13}$$

$$\alpha = -kR_0^{k-2} \frac{(\widetilde{\zeta\Delta\mu} R_0 \delta c_k + (k+1)(\gamma_0 - c_0 \widetilde{\zeta\Delta\mu})\delta R_k)}{4(\hat{\eta} + \eta)} \tag{2.14}$$

$$\beta = kR_0^{k} \frac{(\widetilde{\zeta\Delta\mu} R_0 \delta c_k + (k-1)(\gamma_0 - c_0 \widetilde{\zeta\Delta\mu})\delta R_k)}{4(\hat{\eta} + \eta)} \tag{2.15}$$

Substituting these values in, we find an expression for the velocity at the interface, $\vec{V}$ and from there we find the equations for the rate of change of radius and concentration:

$$\frac{\partial c}{\partial t} = -k \left(\frac{\widetilde{\zeta\Delta\mu} c_0}{2R_0(\hat{\eta} + \eta)} + \frac{Dk}{R_0^2} \right) \delta c_k e^{ik\theta} \tag{2.16}$$

$$\frac{\partial R}{\partial t} = -k \frac{(\gamma_0 - \widetilde{\zeta\Delta\mu} c_0)}{2R_0(\hat{\eta} + \eta)} \delta R_k e^{ik\theta} \tag{2.17}$$

As δR_k does not appear in the equation (2.16) and δc_k does not appear in (2.17), we can see that at the linear level the deformation is not dependent on the perturbation in concentration and vice versa. Looking at the stability of the equations:

$$\frac{\partial \delta R_k(t)}{\partial t} = s\delta R_k(t) = -k \frac{(\gamma_0 - \widetilde{\zeta\Delta\mu} c_0)}{2R_0(\hat{\eta} + \eta)} \delta R_k(t) \tag{2.18}$$

Equation (2.18) shows that providing our droplet tension, $\gamma = \gamma_0 - \widetilde{\zeta\Delta\mu}c_0$, remains positive, which for a contractile active droplet it will, the droplet will be stable in a circular shape.

$$\frac{\partial \delta c_k(t)}{\partial t} = s\delta c_k(t) = -k\left(\frac{\widetilde{\zeta\Delta\mu}c_0}{2R_0(\hat{\eta}+\eta)} + \frac{Dk}{R_0^2}\right)\delta c_k(t) \tag{2.19}$$

From (2.19) we can see that the activity threshold required for the droplet to polarise into a single mode of concentration and thus for droplet motion is:

$$\widetilde{\zeta\Delta\mu} < -\frac{2D(\hat{\eta}+\eta)}{R_0 c_0} \tag{2.20}$$

At the linear level, we find that the droplet shape is stable as a circle for all perturbations and that an instability in the concentration on the boundary leads to motion above an activity threshold. In order to further investigate the complexity of this system, beyond the linear level, we numerically solve our equations.

2.2 Computational Model

Our system is highly coupled and non-linear, restricting the amount of purely analytical analysis which can be done on the system. Therefore, we solve the hydrodynamic equations numerically using finite difference methods and use the immersed boundary method developed by Peskin [80] to introduce our active boundary.

2.2.1 Solving the Hydrodynamic Equations

As our simulations are in the low Reynolds regime, we solve the Stokes equations (2.1), (2.2). We discretise the equations on a periodic staggered grid as shown in fig 2.1.

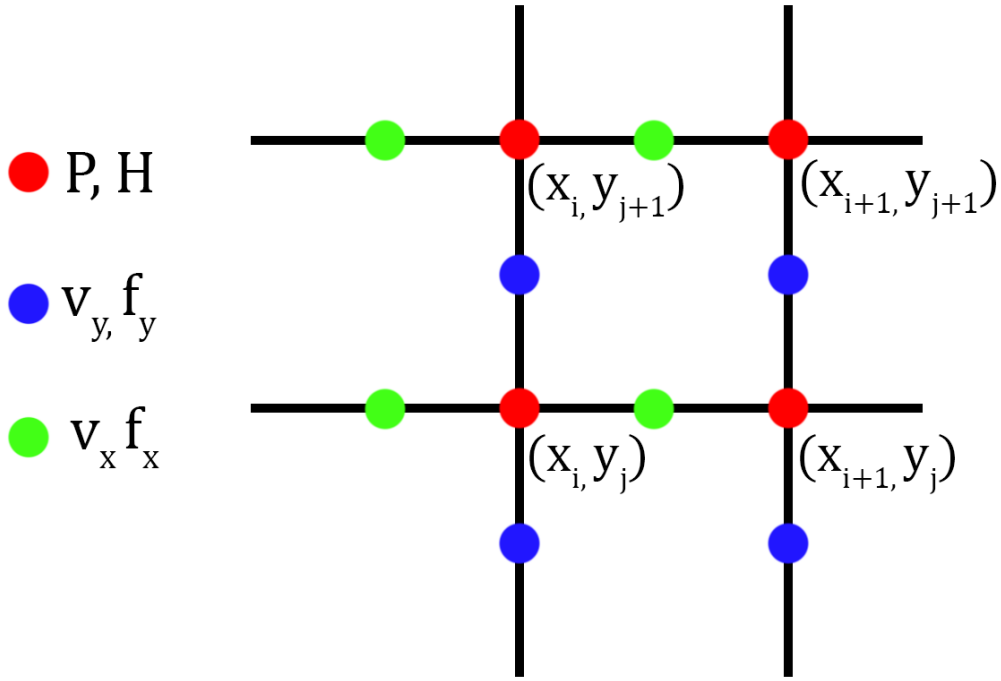

FIGURE 2.1: Diagram of the staggered grid where scalar quantities are calculated on the grid in red, x components on the green grid and y components on the blue grid.

The staggered grid is comprised of three grids, $(x_{i-1/2}, y_j)$, $(x_i, y_{j-1/2})$, and (x_i, y_j), red, green and blue respectively in figure 2.1. x_i runs from $-Lx/2$ to $(-Lx/2 + N_x h)$ whereN_x is the number of grid points in the x direction and h is the grid spacing. y_i follows the same pattern. v_x, f_x are defined on the 1st (green) grid, v_y, f_y are defined on 2nd (blue) grid and P is defined on the 3rd (red) grid.

The staggered grid is used to avoid the problem of pressure-velocity decoupling which occurs for incompressible flows [81]. Another issue which arises is the lack of an explicit equation for pressure in incompressible flow.

Projection methods were introduced to deal with the problem of enforcing incompressible flows. The incompressibility constraint, (2.2), couples velocity and pressure. This makes solving the equations with standard discretisation difficult and involves complicated boundary conditions. Projection methods were first introduced by Chorin and Temam [82], [83] in the late 1960s. The method uses a fractional step scheme. This method makes use of the Helmholtz-Hodge decomposition which states that any vector field can be split into its divergence free and irrotational parts [84]:

$$\vec{A} = \vec{A}_{\text{sol}} + \vec{A}_{\text{irrot}} = \vec{A}_{\text{sol}} + \nabla\psi \tag{2.21}$$

We solve for intermediate values of velocity, $\vec{v}^*$ and pseudo-pressure ϕ:

$$\nabla^2 \vec{v}^* = -\frac{1}{\eta}\vec{f}, \tag{2.22}$$

$$\nabla^2 \phi = \nabla \cdot \vec{v}^*, \tag{2.23}$$

where $\vec{f}$ is the total force density acting on the fluid. $\vec{v}^*$ is solved for followed by ϕ . In the case of a periodic domain discrete Fourier transforms are defined as:

$$\rho_{kl} = \frac{1}{\sqrt{N_x N_y}} \sum_{m=0}^{N_x-1} \sum_{n=0}^{N_y-1} \hat{\rho}_{mn}\, e^{-\frac{2\pi i m k}{N_x}} e^{-\frac{2\pi i n l}{N_y}} \tag{2.24}$$

$$\hat{\rho}_{mn} = \frac{1}{\sqrt{N_x N_y}} \sum_{k=0}^{N_x-1} \sum_{l=0}^{N_y-1} \rho_{kl}\, e^{\frac{2\pi i m k}{N_x}} e^{\frac{2\pi i n l}{N_y}} \tag{2.25}$$

We apply a discrete Fourier transform (DFT) to equations (2.22) and (2.23) to obtain:

$$\hat{\vec{v}}^*_{m,n} = -\frac{1}{\eta \hat{D}^2_{m,n}} \hat{\vec{f}}_{m,n} \tag{2.26}$$

$$\hat{\phi}_{m,n} = \frac{1}{\hat{D}^2_{m,n}} \left(\widehat{\nabla_h \cdot \vec{v}^*}\right)_{m,n} \tag{2.27}$$

where we solve using the transformed Laplacian:

$$\hat{D}^2_{m,n} = \left(e^{\frac{2\pi i m}{N_x}} + e^{\frac{2\pi i n}{N_y}} + e^{\frac{-2\pi i m}{N_x}} + e^{\frac{-2\pi i n}{N_y}} - 4 \right), \tag{2.28}$$

and apply inverse DFTs to obtain $\vec{v}^*$ and ϕ. Using equation (2.21) these are then corrected to $\vec{v}$ and P:

$$\vec{v} = \vec{v}^* - \nabla\phi, \tag{2.29}$$

$$P = \eta \nabla^2 \phi. \tag{2.30}$$

2.2.2 The Immersed Boundary Method

The immersed boundary method was initially developed to model fluid-structure interactions in heart valves [85]. It provides a useful way of studying fluids interacting with complex geometries. Originally devised to tackle fluid-structure interactions, the method has since been extended to model fluid-fluid interfaces laden with surfactants[86]. The basic elements of this method are a fixed, regular Cartesian grid on which the hydrodynamic equations are solved, coupled with a freely moving Lagrangian curve representing the boundary, as shown in figure 2.2. A discrete Dirac delta function is used to link the boundary variables with the bulk fluid.

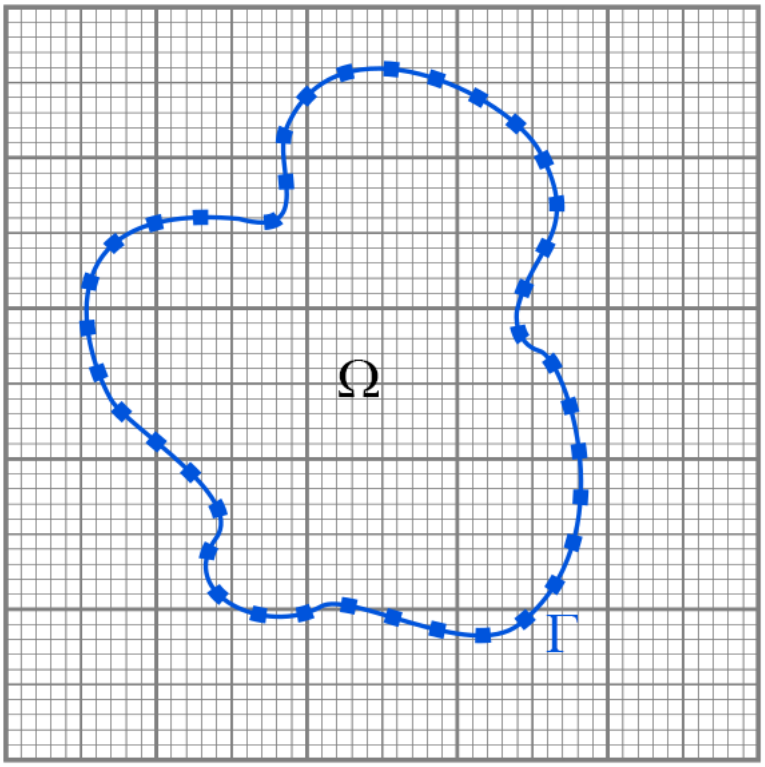

FIGURE 2.2: Diagram showing the Cartesian grid which the hydrodynamic equations are calculated on and the Lagrangian curve in blue which describes the droplet boundary.

The basic algorithm is as follows:

1. Calculate boundary forces.
2. Calculate bulk forces.
3. Solve hydrodynamic equations in bulk.
4. Calculate boundary velocity.
5. Update boundary position.
6. Add or remove boundary points if required.

The fluid domain, Ω is defined on a Cartesian grid of spacing h, with coordinates $\vec{x} = (x, y)$ and the boundary, Γ, is given in parametric form $\vec{X}(s,t), 0 \leq s \leq L_b, \vec{X}(0,t) = \vec{X}(L_b,t)$, where L_b is the length of the boundary and s is a point along the boundary.

The boundary, Γ, is discretised into a grid of points, $s_k = k\Delta s$, $k = 0...N_s$, where $N_s(t)$ is the number of points. Each point has corresponding Cartesian coordinates: (X_k, Y_k) and the offset grid at $(X_{k+1/2}, Y_{k+1/2}) = (X_{k+1} + X_k, Y_{k+1} + Y_k)/2$. The initial N_s is chosen to so $\Delta s \sim h/2$.

The force density on the boundary is given by equation (2.5). We use the convention of lowercase variable names for fluid associated quantities and capital letters for boundary associated variables. In it's discrete form, this becomes:

$$\vec{F}_{k+1} = \partial_s(\gamma_k \vec{\tau}_k) \tag{2.31}$$

$$\vec{\tau}_k = \frac{\partial_s \vec{X}_k}{|\partial_s \vec{X}_k|}. \tag{2.32}$$

Here the tangent vector $\vec{\tau}$ is defined at $\vec{X}_{k+\frac{1}{2}}$ along the curve.
The force density in the bulk is then:

$$\vec{f}(\vec{x},t) = \int_\Gamma \vec{F}(s,t)\delta(\vec{x} - \vec{X}(s,t))ds. \tag{2.33}$$

the hydrodynamic equations (2.1), (2.2), are solved on the Cartesian grid to obtain the bulk velocity. From this the velocity of the boundary is calculated:

$$\vec{V}(\vec{X}(s,t),t) = \int_\Omega \vec{v}(\vec{x},t)\delta(\vec{x} - \vec{X}(s,t))d^2\vec{x}. \tag{2.34}$$

For our discrete Dirac delta function we use a 2D numerical delta function as described in [80]:

$$\delta_h(\vec{x} - \vec{X}) = \frac{\Phi(\frac{x-X}{h})\Phi(\frac{y-Y}{h})}{h^2} \tag{2.35}$$

Where Φ is a numerical version of the one dimensional delta function and is defined as:

$$\Phi(r) = \begin{cases} \frac{(5+2r-\sqrt{-4r^2-12r-7})}{8}, & \text{if } -2 < r < -1 \\ \frac{(3+2r+\sqrt{-4r^2-4r+1})}{8}, & \text{if } -1 \leq r < 0 \\ \frac{(3-2r+\sqrt{-4r^2+4r+1})}{8}, & \text{if } 0 \leq r < 1 \\ \frac{(5-2r-\sqrt{-4r^2+12r-7})}{8}, & \text{if } 1 \leq r < 2 \\ 0, & \text{otherwise} \end{cases} \tag{2.36}$$

The boundary is then updated using the midpoint method:

$$\vec{X}_{n+1} = \vec{X}_n + \Delta t \vec{V}(t_n + \frac{\Delta t}{2}, X_n + \frac{\Delta t}{2}\vec{V}(t_n, X_n)) \tag{2.37}$$

The main advantage of the immersed boundary method is that it it reduces the amount of computational time spent on grid generation. As the Cartestian grid remains fixed it only needs to be generated once, and only the Lagrangian grid representing the boundary has to be updated at each time step. This is compared to body-conformal simulations where the grid across the entire domain must be re-generated each time step, along with a method to project the solution onto a new grid [87].

The ability of this method to handle complex geometry relatively efficiently along with it's applications to fluid-boundary and fluid-fluid interactions makes it an attractive choice when studying biological systems. Another advantage is the ability to give the boundary physical properties for example varying surface tension mediated by surfactant concentration [86].In our case of an active droplet, the tension is modified via the concentration of contractile particles attached to the boundary [79].

2.2.3 The form of the effective activity

We defined the droplet tension, γ as:

$$\gamma = \gamma_0 - \widetilde{\zeta\Delta\mu c}, \tag{2.38}$$

where the excluded volume effects preventing the active particles getting too close together are absorbed into the active term. For our simulations we must explicitly include this.

$$\gamma = \gamma_0 - \zeta\Delta\mu c - \Pi(c(\vec{s})) \tag{2.39}$$

$\Pi(c(\vec{s}))$ is a phenomenological term which is included to model excluded volume effects of the molecular motors. When constructing this term we consider that the force density on the boundary is given by $\nabla_s(\gamma\vec{\tau})$, so to yield a force in the tangential direction $\Pi(c(\vec{s}))$ must be of the following form:

$$\Pi(c(\vec{s})) = \int B(c(\vec{s}))c'(\vec{s})ds. \tag{2.40}$$

Previous versions of this model[72] implemented a quadratic term $\frac{Bc^2}{2}$, to model excluded volume effects. Excluded volume effects are only relevant when particles are close together. This motivated us to pick a new form of B which only acts when active particles are close together. We want a force in the tangential direction which is negligible below a certain concentration threshold and repulsive above it. The first obvious choice for B would be to use a Heaviside function on the concentration, however we need an integrable function for $\Pi(c(\vec{s}))$ so we look at analytic approximations of step functions. Our choice of B is:

$$B(c(\vec{s})) = A - \frac{A\sinh 20}{\cosh 20 + \cosh\frac{20c(\vec{s})}{Tc_0}}. \tag{2.41}$$

Here A is a measure of the strength of the repulsive force between particles, and Tc_0, sets the maximum concentration. We chose a threshold concentration of $2c_0$.

2.2.4 Implementing viscosity difference

In order to distinguish between the inside and outside of the cell we use a level set function $H$where:

$$\nabla H(\vec{x},t) = -\int_\Gamma \hat{\vec{n}}(s,t)\delta(\vec{x}-\vec{X})dl = \begin{cases} 1, & \text{if } \vec{x}\in\Omega_c \\ 0, & \text{otherwise} \end{cases} \tag{2.42}$$

By taking the divergence of both sides, we obtain a Poisson equation which we solve using the same FFT based method in section 2.2.1.

$$\nabla^2 H(\vec{x},t) = -\nabla\cdot\int_\Gamma \hat{\vec{n}}\delta(\vec{x}-\vec{X})dl. \tag{2.43}$$

We can use H to define the viscosity inside, $\eta^{(int)}$, and outside, $\eta^{(ext)}$ the cell:

$$\eta = \eta^{(ext)} + \Delta\eta H \tag{2.44}$$

$$\Delta\eta = \eta^{(int)} - \eta^{(ext)} \tag{2.45}$$

2.3 Model analysis

The aspects of migration we are particularly interested in are the migratory speed of the droplet and the droplet shape. Our linear stability analysis in section 2.1.1 indicates that to the linear level the deformation of the droplet does not depend on perturbations in concentration and the radius is stable for all positive values of droplet tension. It also led us to an expression for a threshold value of activity for motion. However in simulations we see both deformation and sustained motion below the calculated activity threshold when we vary the internal and external viscosities relative to one another.

We take $\eta^{(int)} = 10^4$ Pas in line with measured values of the cytoskeleton viscosity [88] as our maximum internal viscosity. However there is large variation in estimates for cytoskeleton viscosity [89], [90], so we also look at droplets with lower viscosities. We consider only cases where $\eta^{(int)} \geq \eta^{(ext)}$, as the measured viscosities of the cytoskeleton - while varied - are higher than that of the viscosity of typical surrounding environments e.g. plasma or, interstitial or transcellular fluid.

In appendix A we list the values of the simulation parameters used along side the actual values for these quantities. We include a short discussion about our chosen parameter values. Unless otherwise stated these apply for all simulations in the thesis. Additionally, for all graphs the error bars show the standard deviation of the measured value in each simulation.

2.3.1 Qualitative overview of droplet motion

Like Whitfield et al in their previous work [72],we observed that droplets which are capable of motion, when initialised with homogeneous concentration on the boundary, will polarise into a region of high concentration and a region of low to zero concentration in the presence of a small perturbation. In the interests of time we initialise our simulations with the droplet in a polarised state, with the concentration profile (as

shown in figure 2.3):

$$c(\theta) = (1 - \cos(\theta))c_0 \tag{2.46}$$

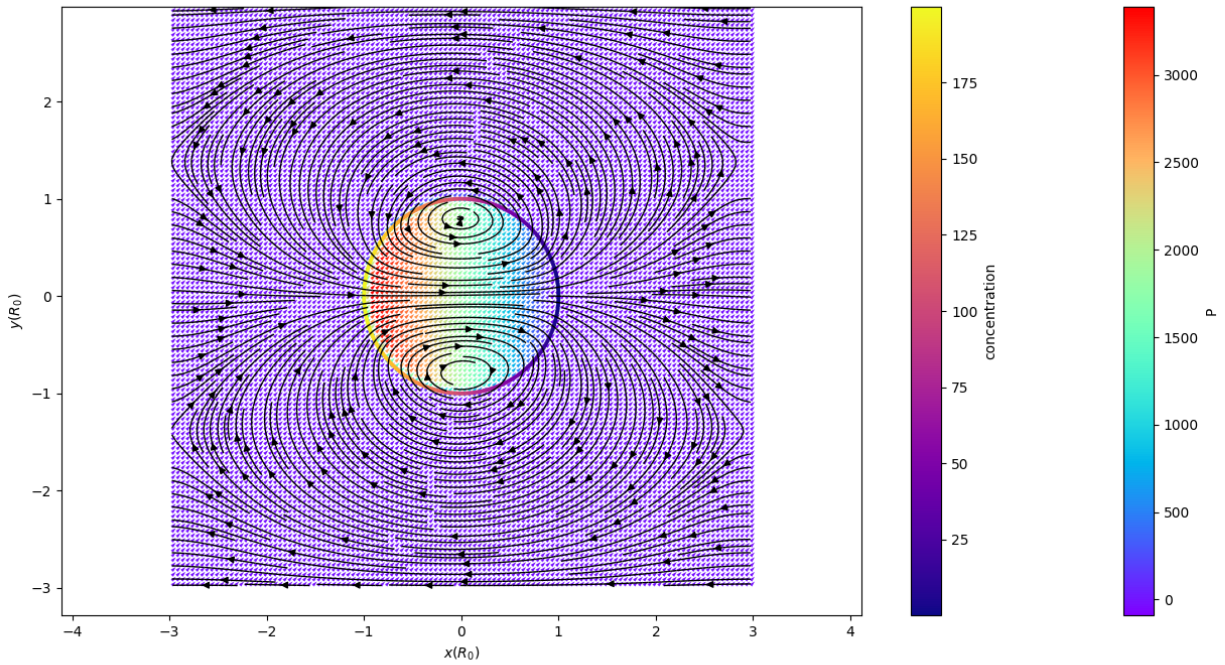

FIGURE 2.3: Example simulation snapshot, showing the active droplet in it's initial configuration, with velocity stream lines overlaid. The rainbow colour scale represents pressure, and the other colour scale denotes concentration on the boundary.

Any droplets which are not capable of sustaining motion return to a state of homogeneous concentration on the boundary and come to a halt.

For motile drops the concentration profile on the boundary takes on a tophat function like form, at steady state, with a region of no active particles at the front of the droplet and a steep gradient to a region of high concentration, which we call the active region. See figure 2.4 for a typical profile.

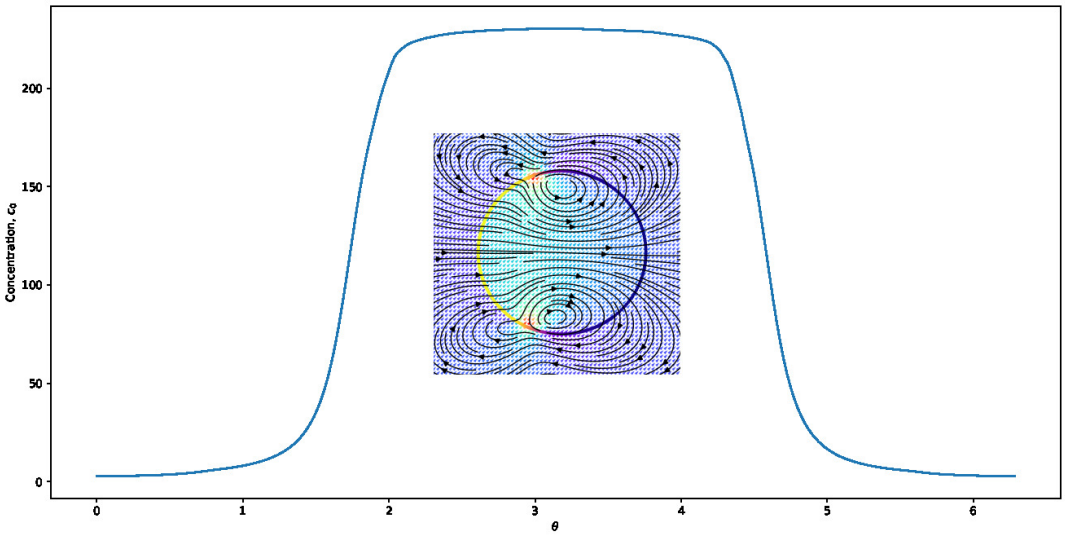

FIGURE 2.4: Example concentration profile for a droplet with $\eta^{(int)} = \eta^{(ext)} = 100, \zeta\Delta\mu = -2.0$ in simulation units. Snap shot of the simulation overlaid.

For droplets where $\eta^{(int)} = \eta^{(ext)}$ droplets maintain a circular shape, apart from at very high activities there is a very small deformation in the second Fourier mode which relates to ellipsoidal deformations. Droplets with a viscosity difference, however, deform into more complex shapes than an ellipsoid, examples are shown in figure 2.5.

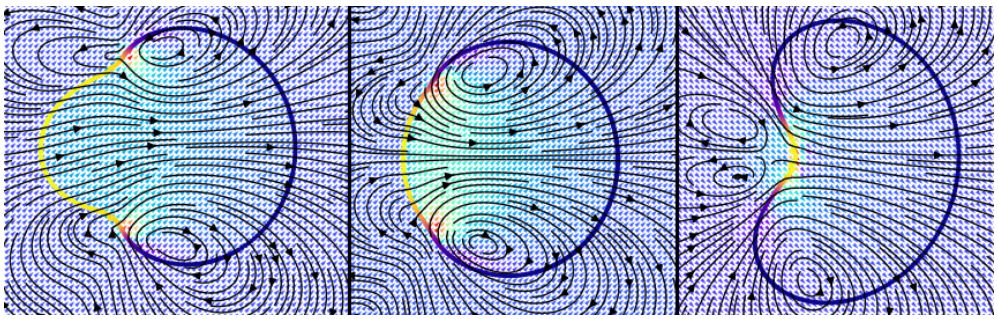

FIGURE 2.5: Examples of types of deformation we see in simulations, where aspect ratio and curvature of the active region are the main points of difference. The left hand droplet has parameters: $\eta^{(int)} = 100$, $\eta^{(ext)} = 10$, $|\zeta\Delta\mu|$=3. The middle droplet has parameters: $\eta^{(int)} = 1000$, $\eta^{(ext)} = 10$, $|\zeta\Delta\mu|$=7 and the right hand droplet has parameters:$\eta^{(int)} = 1000$, $\eta^{(ext)} = 500$, $|\zeta\Delta\mu|$=15.

We see that simulations with lower total viscosities tend to elongate along the axis of motion and droplets with higher total viscosities tend to elongate perpendicular to the axis of motion, with some notable exceptions. We also see cases of convex or concave deformation of the active region at the rear of the cell.

We also see that for droplets with a large difference in viscosity relative to their

total viscosity droplets can sustain motion below the predicted activity threshold for motion from the linear stability analysis performed in section 2.1.1 suggesting a non-linear effect dependent on the difference in viscosity between the droplet and external fluid.

To explore these results we first define hydrodynamic forc emoments for a droplet and then examine changes in velocity and shape based on viscosity differences.

2.3.2 Boundary Integral Equations and Force Moments

Here we introduce some concepts which we will use to analyse our simulation results in later sections.

We can write the velocity of a moving droplet using boundary integral formulation [91]. The velocity field at the interface of a 2D active droplet can be written as:

$$v_j(\vec{X}) = -\frac{1}{2\pi(\eta^{(int)}+\eta^{(ext)})}\int_\Gamma F_i\mathcal{G}_{ij}(\vec{x},\vec{X})ds(\vec{x}) - \frac{\eta^{(int)}-\eta^{(ext)})}{2\pi(\eta^{(int)}+\eta^{(ext)})}\int_\Gamma v_i(\vec{x})\mathcal{T}_{ijk}(\vec{x},\vec{X})n_k(\vec{x})ds(\vec{x}) \quad (2.47)$$

Where, $\mathcal{G}_{ij}$ is the Green's function for 2D Stokes flow and $\mathcal{T}_{ijk}$ is it's associated stress tensor. $\vec{n}$ is the outward pointing normal to the droplet.

The first term on the righthand side of (2.47) is called the single layer potential and the second the double layer potential (the methodology deriving from electrostatics). The single layer can be thought of as a line of point forces while the double layer corresponds to a line of force dipoles.

We can perform a multipole expansion on equation (2.47) and from this we can derive (see Appendix 2.A for more details) the force moments acting on the droplet [92]. We list the first three here.

$$F_i^{(1)} = \int_\Gamma F_i \mathrm{d}s \quad (2.48)$$

$$F_{ij}^{(2)} = \int_\Gamma F_i r_j \mathrm{d}s - (\eta^{(ext)}-\eta^{(int)})\int_\Gamma (v_j\hat{n}_i + v_i\hat{n}_j)\,\mathrm{d}s \quad (2.49)$$

$$F_{ijk}^{(3)} = \int_\Gamma F_i r_j r_k \mathrm{d}s - (\eta^{(ext)}-\eta^{(int)})\int_\Gamma (v_j\hat{n}_i + v_i\hat{n}_j) r_k \mathrm{d}s \quad (2.50)$$

Where F_i is the force density on the interface and r_i is the distance to the interface and $i = x, y$. As the droplet migrates under force free motion, $F_i^{(1)} = 0$, as expected.

Removing the isotropic part of the dipole moment from (2.49), we can split the rest into a symmetric, S_{ij} and antisymmetric T_{ij} part [92]:

$$F_{ij}^{(2)} - \frac{1}{2}F_{kk}^{(2)}\delta_{ij} = S_{ij} + T_{ij} \tag{2.51}$$

where,

$$S_{ij} = \frac{1}{2}\left(\left(F_{ij}^{(2)} - \frac{1}{2}F_{kk}^{(2)}\delta_{ij}\right) + \left(F_{ij}^{(2)} - \frac{1}{2}F_{kk}^{(2)}\delta_{ij}\right)^{T}\right) \tag{2.52}$$

The symmetric part is called the stresslet and corresponds to straining forces which act on the droplet, as shown in figure 2.6 while the antisymmetric part corresponds to rotational torques, this is zero here as $F_{xy} = F_{yx} = 0$.

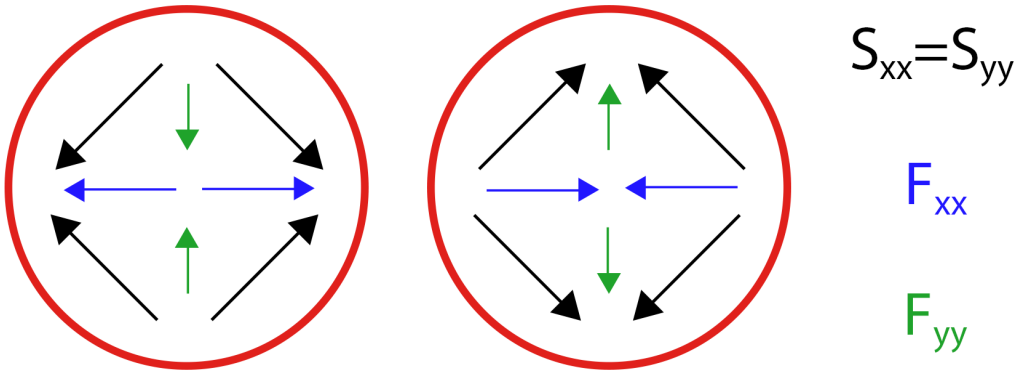

FIGURE 2.6: Diagram showing the stresslet, which is the symmetric part of the dipole moment, The stresslet,$S_{xx} = S_{yy}$ (from now on we will use S_{xx}),is shown in black, F_{xx} is shown in blue, and F_{yy} is shown in green. The left diagram is for positive S_{xx} and the right is negative S_{xx}.

The quadrupole force moment, (2.50), is associated with front back asymmetry of a swimmer [93]. To more intuitively understand quadrupole moments figure 2.7 shows the non zero force moments for a droplet where viscosities are equal (so $F_{xyx} = F_{yyx}$).

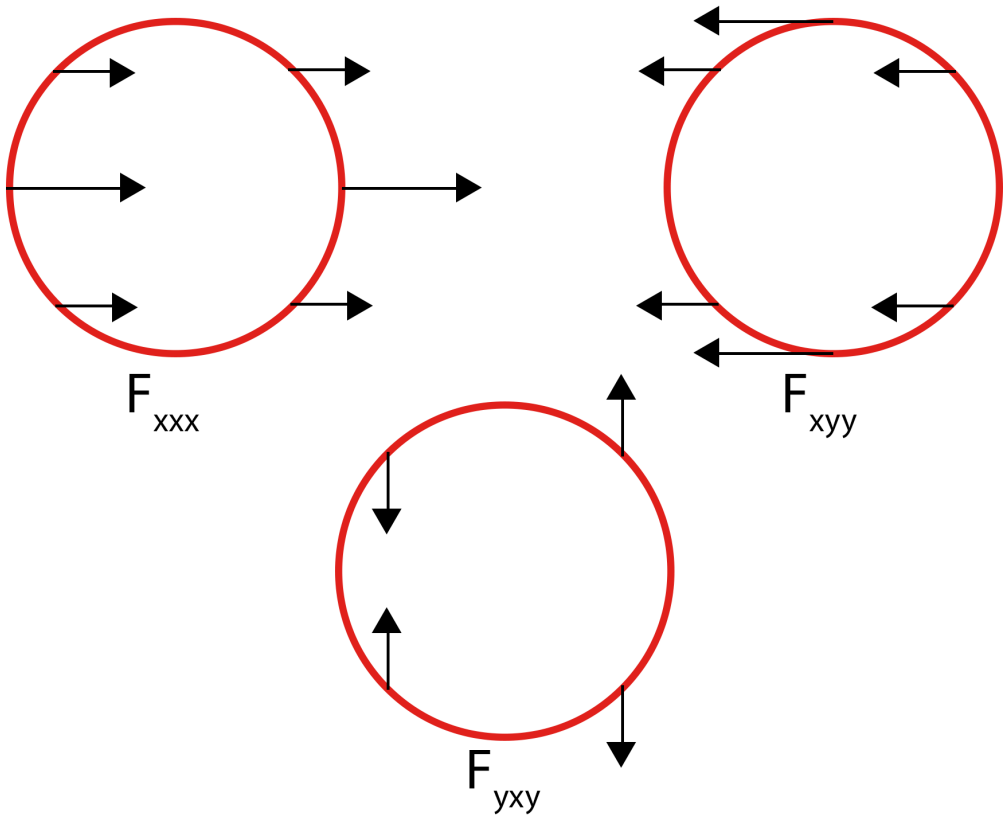

FIGURE 2.7: Cartoon of the relative directions and strength of the non-zero quadrupole moments for a droplet where $\eta^{(int)} = \eta^{(ext)}$.

We can decompose the quadrupole moment into a purely symmetric part, S_{ijk}, a purely antisymmetric part, A_{ijk} and a mixed symmetry part, N_{ijk}:

$$F^{(3)}_{ijk} = S_{ijk} + A_{ijk} + N_{ijk}. \tag{2.53}$$

As with the dipole, the symmetric part relates to deformations, the anti-symmetric part corresponds to rotation and the remaining mixed symmetry part captures the finite size of the droplet corresponding to a source dipole.

The symmetric part of the quadrupole moment, S_{ijk} is given by [94]:

$$S_{ijk} = \frac{1}{6}\left(F_{ijk} + F_{ikj} + F_{jik} + F_{jki} + F_{kij} + F_{kji}\right) \tag{2.54}$$

This leaves us with 4 unique components, S_{yyy} and S_xxy are non-zero in our case.

To extract the force moments from our simulations we realign the droplets and associated fields so that the droplet is orientated along the x-axis, and the centre of mass is at the origin, using the centre of mass velocity vector. We then calculate the force dipoles and quadrupoles acting on each droplet, using discrete versions of (2.49) and (2.50), from our simulation values on the boundary.

2.3.3 Droplet Velocity

From our linear stability analysis we show that there is a threshold for droplet motion, below which the concentration of active particles on the boundary will not polarise to allow for sustained motion. As shown in [72], when the concentration profile resolves into a single peak the droplet will move.

Due to the coupled non-linear nature of our system, finding an expression for the translational velocity of our droplet is non-trivial. The active force driving the droplet is indirectly a function of the velocity at the boundary via the concentration and in turn the cell velocity is a function of the active force. This positive feedback loop is what allows the droplet concentration to polarise and induce motion.

In order to estimate the translational velocity, $|v|$, of the droplet we take the case of an undeformable circular droplet, and look only at the first mode of velocity - which is the mode associated with translation in 2D. It should be noted that the Stokes paradox does not apply in the case of a droplet moving under a surface concentration gradient. As there is no net mechanical force on the droplet, the logarithmic term which causes issues with the boundary condition at infinity does not appear[95]. We use the same general solutions that we used for the linear stability analysis in section 2.1.1 and the following boundary conditions (in the frame of reference of the droplet):

$$\lim_{r\to\infty} \vec{v} = -|v|\mathbf{e}_x \tag{2.55}$$

$$v_r|_{r=R} = \hat{v}_r|_{r=R} = 0 \tag{2.56}$$

$$v_\theta|_{r=R} = \hat{v}_\theta|_{r=R} \tag{2.57}$$

Here hats denote variables inside the droplet, so $\vec{v}$ is the velocity field outside the droplet and $\hat{\vec{v}}$ is the velocity field inside the droplet. |v| is the translational velocity of the droplet.

Using the condition that for an active droplet:

$$(\underline{\hat{\sigma}} - \underline{\sigma}) \cdot \mathbf{e}_\theta|_{r=R} = -\frac{1}{R}\partial_\theta(\gamma_0 - \widetilde{\zeta\Delta\mu}c(\theta))|_{r=R}, \tag{2.58}$$

and making the assumption that the first mode of velocity is associated with the first mode of concentration, due to our coupled system, we reach an expression for the translational velocity of a droplet (where c_1 is the first mode of concentration).

$$|v| = \frac{-\widetilde{\zeta\Delta\mu}c_1}{4(\hat{\eta}+\eta)} \tag{2.59}$$

2.3.3.1 Internal viscosity equal to external viscosity

We first look at the case where the viscosity of the fluid in the droplet, $\eta^{(int)}$ is equal to the viscosity of the external fluid,$\eta^{(ext)}$. Using $\eta = \eta^{(int)} = \eta^{(ext)}$ in this section to denote the viscosity.

We do not, a priori, know what c_1 is in our simulations as the concentration profile is an emergent property, so we instead plot (2.59) using the initial concentration c_0

rather than c_1, against the centre of mass velocity of the droplets in figure 2.8. We also use only the contractile activity term, neglecting the excluded volume term from our active force.

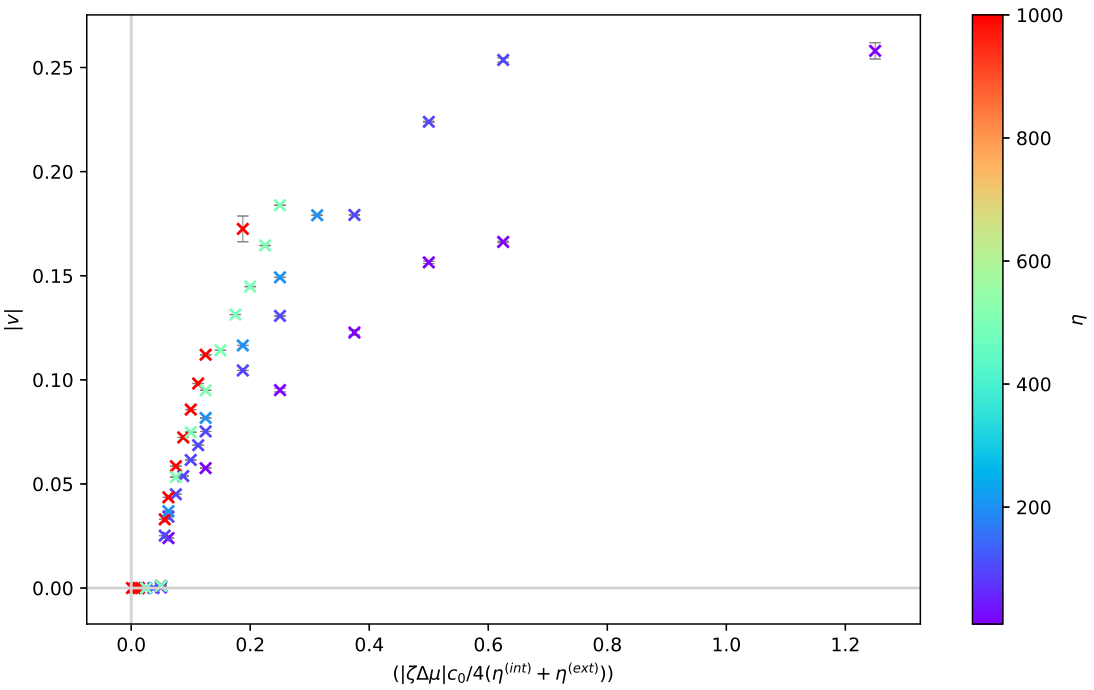

FIGURE 2.8: Plot of the centre of mass velocity from simulations, $|v|$, against $\frac{|\zeta\Delta\mu|c_0}{4(\eta^{(int)}+\eta^{(ext)})}$, for droplets where $\eta = \eta^{(int)} = \eta^{(ext)}$. The colour bar indicates the viscosity η.

In figure 2.8 we see that for different values of viscosity the curves do not collapse down onto one linear curve as predicted by the estimate, instead they seem to be a non-linear function of $\frac{|\zeta\Delta\mu|}{\eta}$. We also note that the threshold for motion is in agreement with the prediction from the linear stability analysis (2.20).

2.3.3.2 Constant total viscosity

We have already seen in the previous section, see figure 2.8,that the total viscosity in the system affects the velocity of the droplet. Here we vary the difference in viscosity between the droplet and its surroundings while keeping the total viscosity constant. We chose a constant total viscosity of $\eta = 1000$ in simulation units.

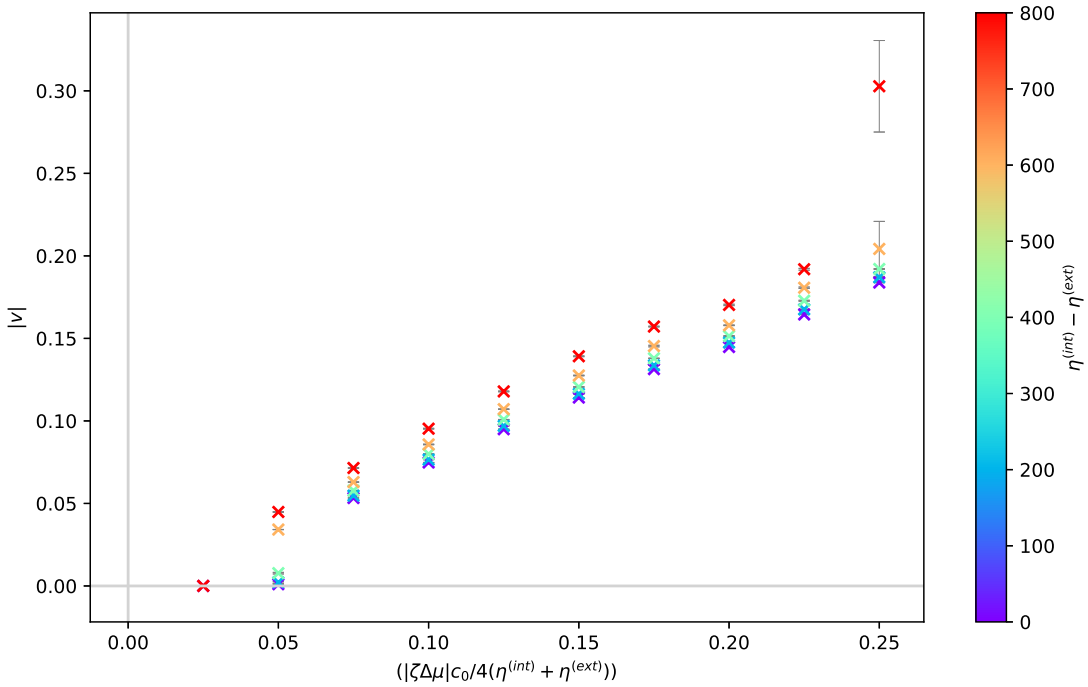

FIGURE 2.9: Plot of the centre of mass velocity, $|v|$, against $\frac{|\zeta\Delta\mu|c_0}{4(\eta^{(int)}+\eta^{(ext)})}$, where $\eta^{(int)} + \eta^{(ext)} = 1000$. The colour bar here represents the difference viscosities.

We see in figure 2.9 that, excluding the far right point for $\eta^{(int)} - \eta^{(ext)} = 800$ where significant deformation of the droplet away from a circle occurs, the centre of mass velocity for the droplets seems to be of the same form for all viscosity differences.

We recall the boundary integral equation for the velocity at a droplet boundary, (2.47). Though this is an expression for the velocity at the boundary, we have established that the translational velocity is a function of the boundary velocity. We see from (2.47) that the second term on the right hand side only exists if there is a difference in viscosities. Keeping this in mind, we try implementing a correction to figure 2.9 with a similar form.

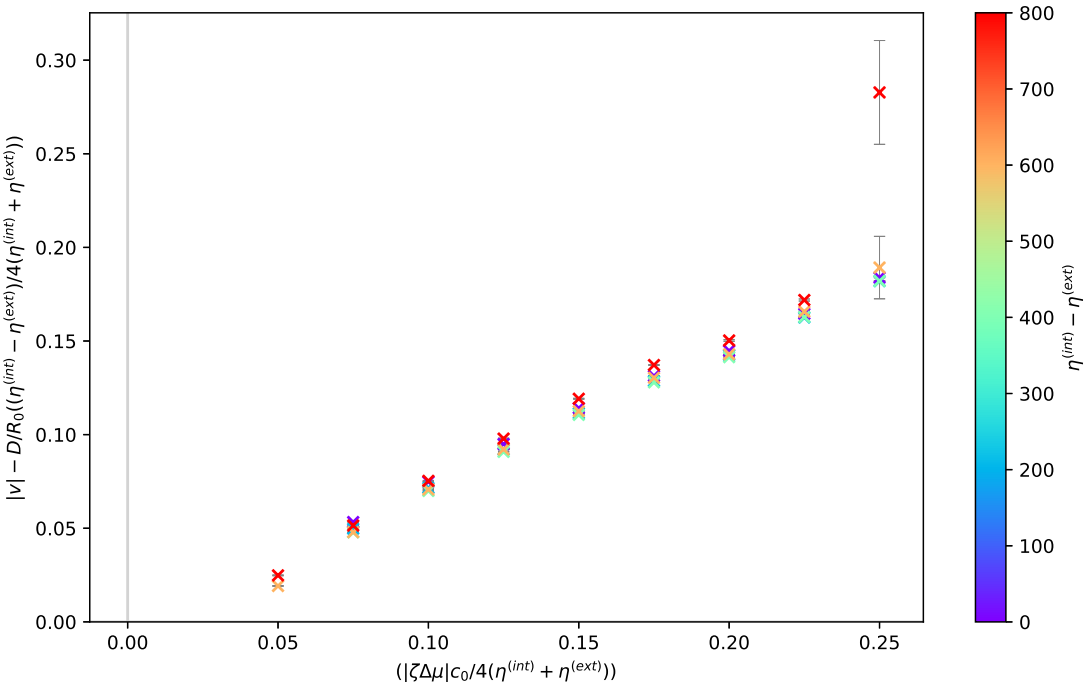

FIGURE 2.10: Plot of the centre of mass velocity, $|v|$, against $\frac{|\zeta\Delta\mu|c_0}{4(\eta^{(int)}+\eta^{(ext)})}$, where $\eta^{(int)} + \eta^{(ext)} = 1000$. The colour bar here represents the difference viscosities. We include only motile droplets and we have subtracted $\frac{D}{R_0}\frac{(\eta^{(int)}-\eta^{(ext)})}{4(\eta^{(int)}+\eta^{(ext)})}$ from $|v|$, to collapse the points to a single curve

In figure 2.10 we shift each curve (plotting only motile droplets) by $\frac{D}{R_0}\frac{(\eta^{(int)}-\eta^{(ext)})}{4(\eta^{(int)}+\eta^{(ext)})}$. This collapses the curves to one curve. There is still some small variation from the curve, this may be due to deformation away from the assumed circular shape of the droplet, or the effects of the excluded volume term in the model. As the difference in viscosities only shifts the curve, this indicates that the sum of the internal and external viscosities dictates the form of the function for droplet translational velocity rather than the difference in viscosity.

2.3.3.3 Threshold activity for motion

We see that for some droplets where we have a large contrast in viscosities that the activity threshold for migration is below that predicted in the linear stability analysis. For example in the case where $\eta^{(int)} = 1000$ and $\eta^{(ext)} = 10$ then the predicted activity threshold for migration is $\zeta\Delta\mu = -2.01$, however we see for activity $\zeta\Delta\mu = -1.0$ that the droplet moves with a steady non-zero velocity. There is also minimal deformation here.

If we think about the origins of our threshold expression, it derives from the advection-diffusion equation for the concentration of active particles. As we keep the diffusion constant the same in all our simulations, the activity plays a part in whether the droplet will polarise into a motile state via advection due to influencing the velocity at

the boundary.

Let us consider, again, the double layer term in the boundary integral equation (2.47). This term describes relative slip at the boundary of the droplet. This increases the boundary velocity, increasing the relative effect of advection compared to diffusion. This increases the value of concentration in the active region of the droplet which increases the driving active force for a given activity, thus decreasing the activity threshold for motion. This effect is also why in the previous section where the total viscosity was constant but we varied the viscosity difference, the droplets with a greater viscosity difference had a higher velocity as seen in figure 2.9.

2.3.3.4 Relating the velocity to force moments

The source dipole corresponds to the first mode of velocity, which captures the translational motion of a droplet [96]. As we have expanded the velocity of our droplet in terms of force moments the source dipole is captured as a part of the quadrupole force moment as described in section 2.3.2. If we plot this term, $|N_{xyy}|$, scaled by the viscosity, against the translational velocity of the droplet, $|v|$, we see that for $\eta^{(int)} = \eta^{(ext)}$ we get a near perfect correlation in figure 2.11. When we introduce a viscosity difference we see there is more spread in the points (figure 2.12).

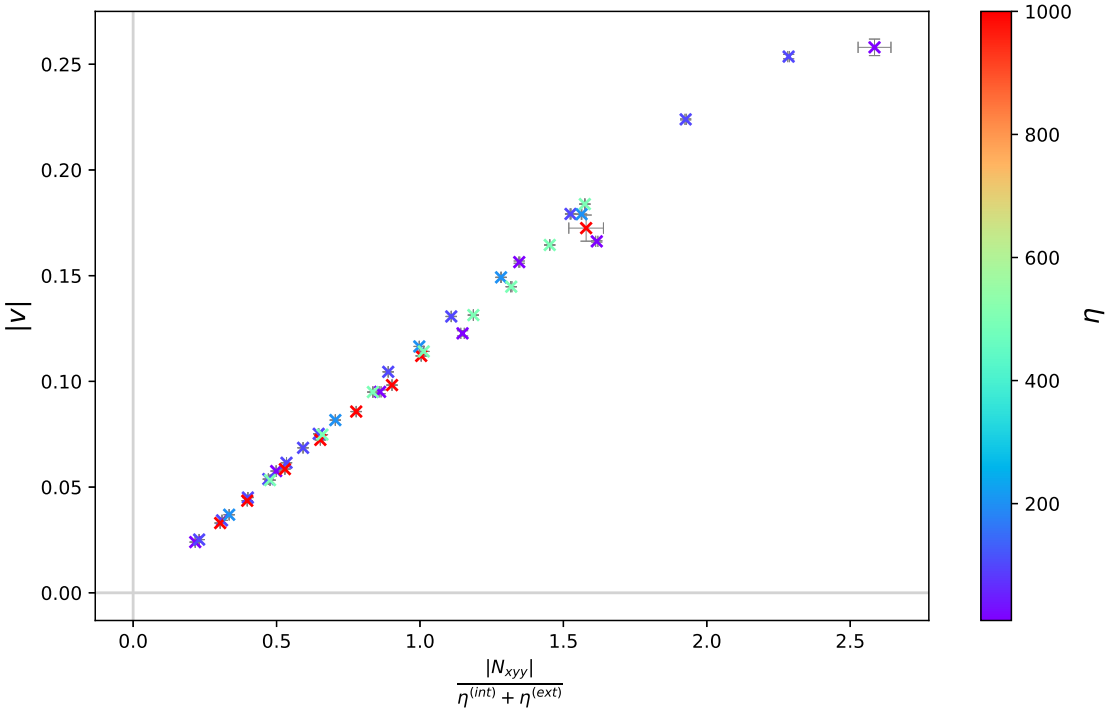

FIGURE 2.11: Plot showing the correlation between droplet centre of mass speed for droplets where $\eta^{(int)} = \eta^{(ext)}$ and $\frac{|N_{xyy}|}{\eta^{(int)}+\eta^{(ext)}}$. $|N_{xyy}|$ is the part of the quadrupole moment related to the source dipole of a droplet, see equation (2.53). The colour bar denotes viscosity, $\eta = \eta^{(int)} = \eta^{(ext)}$.

We consider the full set of droplets in figure 2.12 and see that the points no longer collapse onto a single line. Instead it seems the quanities are still linearly related but the gradient differs based on the viscosity difference for the droplets.

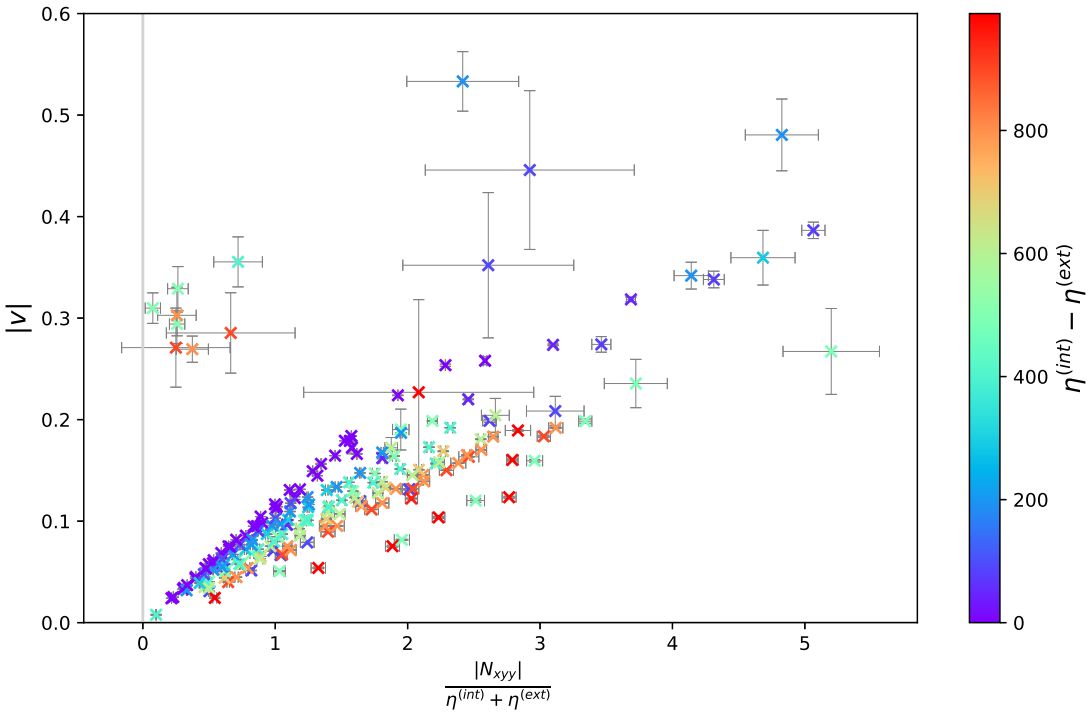

FIGURE 2.12: Plot showing the correlation between droplet centre of mass speed for all droplets and $\frac{|N_{xyy}|}{\eta^{(int)}+\eta^{(ext)}}$. $|N_{xyy}|$ is the part of the quadrupole moment related to the source dipole of a droplet. The colour bar shows the difference in viscosity.

When we have equal viscosities $|N_{xyy}| = |N_{yxy}| = |N_{yyx}|$. These components are no longer equal when we introduce a viscosity difference, since $F^{(3)}_{yxy} \neq F^{(3)}_{yyx}$, due to the second term on the right hand side of (2.50). This comes from the relative slip introduced by the double layer potential term in equation (2.47). We apply a correction to account for difference in velocity due to relative slip induced by the viscosity difference and find:

$$|v| \propto \frac{|N_{xyy}| - \frac{1}{4}(N_{yxy} - N_{yyx})]}{(\eta^{(int)} + \eta^{(ext)})}. \tag{2.60}$$

We see in figure 2.13 that this correction recovers the linear relationship we see in figure 2.11. The points which are off trend on the left of the figure above the curve correspond to droplets with an active region with negative curvature which we will discuss more in the next section.

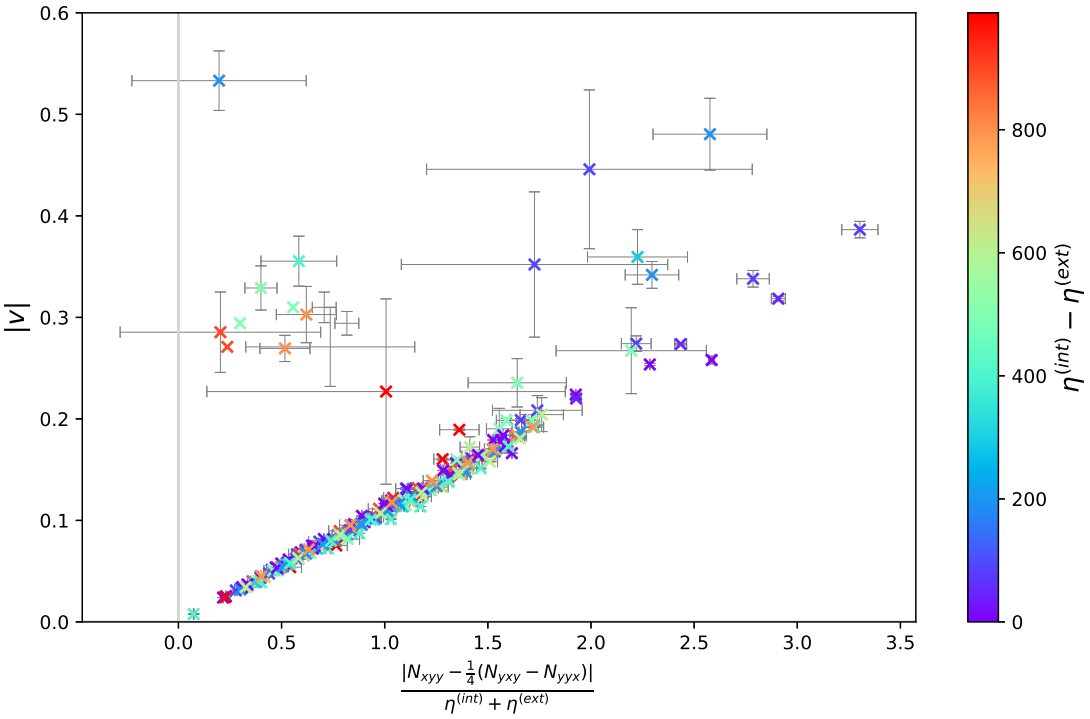

FIGURE 2.13: Plot showing the correlation between droplet centre of mass speed for all droplets and our corrected expression for the source dipole part of the quadrupole moment over viscosity, shown in equation (2.60). The colour bar shows the difference in viscosity.

2.3.4 Droplet deformation

As noted in section 2.3.1 for droplets with a contrast in viscosity to the environment we see more pronounced deformation away from a circle. The droplet shape is a consequence of the normal force balance at the boundary, so the curvature, κ, at any point will be a ratio of the normal constraint and the boundary tension:

$$\kappa = \frac{\vec{n} \cdot \Delta\underline{\underline{\sigma}} \cdot \vec{n}}{\gamma} \tag{2.61}$$

$$\sigma_{ij} = 2\eta u_{ij} - P\delta_{ij} \tag{2.62}$$

As the droplet is moving it is not just a case of balancing the pressure jump, ΔP with the tension, γ (as defined in (2.4)). There is also difference in the normal component of the strain rate tensor, u_{ij}. While the internal and external velocity fields are equal at the boundary the differential isn't necessarily. We also have an explicit difference in η which we are exploring in this section. This indicates that the larger the difference in viscosities, the greater the change in curvature compared to the base curvature of the undeformed droplet, $\kappa = 1$.

The 3 shape parameters we measure from our simulations are:

- Aspect Ratio, $\frac{a}{b}$

- Curvature of the active region, κ
- Active fraction

We extract the aspect ratio by fitting an ellipse to our droplet, where a is the radius along the axis of motion and b is the radius perpendicular to the axis of motion.

The active region is the high concentration region of the droplet boundary. As there is a fairly sharp transition between the region of high concentration and low concentration on the boundary, we define the length of the active region as the boundary length between the points of maximum and minimum gradient in concentration on the boundary. The active fraction is then the fraction of the total boundary length the active region takes up. We then extract the curvature of the active region by fitting a circle to the active region to find the radius of curvature, R_c. where $\kappa = \frac{1}{R_c}$.

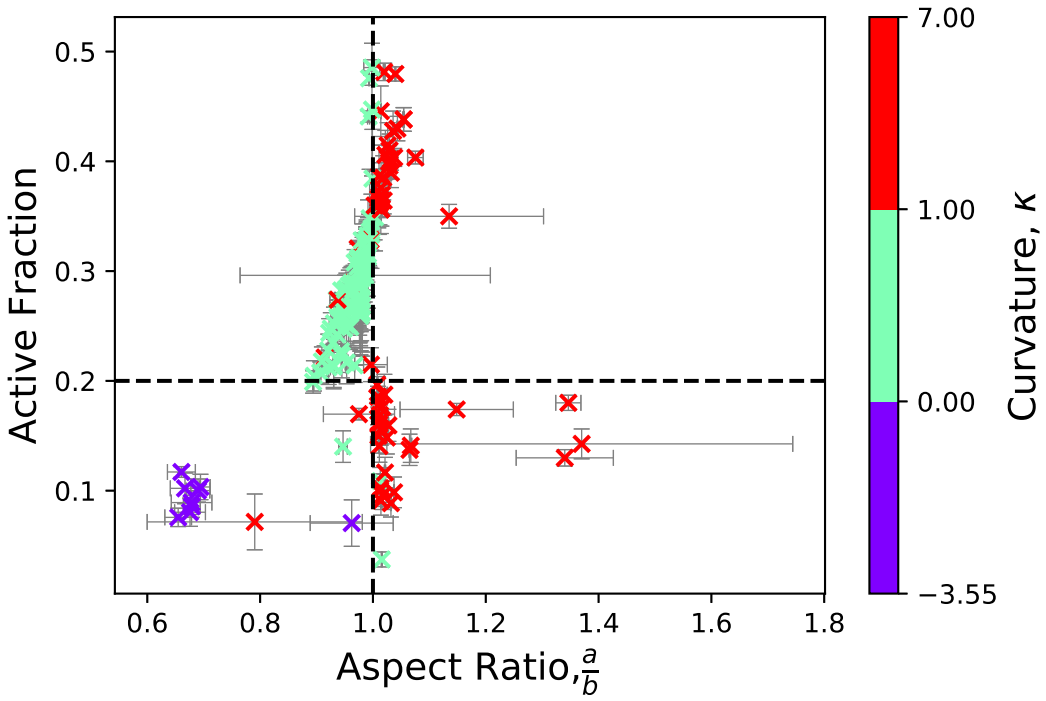

FIGURE 2.14: The active fraction, defined as the length of the active region as a fraction of the total boundary length, against the aspect ratio of the droplets. The colour bar signifies curvature of the active region, it is split into negative curvature (purple), lower curvature than a unit circle (mint) and curvature higher than a unit circle (red). The vertical dashed line at $\frac{a}{b} = 1$ is where the droplet is a circle, so divides the drops into those elongated along their axis of motion, and perpendicular to the axis of motion. The dashed horizontal line where the active fraction is 0.2 is drawn to help highlight the clusters of droplets

We initially plot these shape measures in figure 2.14, to get an overview of the data. There are 3 rough clusters. The largest cluster is the group of points where the active fraction is greater than 0.2. We will see later this is where the quadrupole is dominant over the stresslet. The purple points at the bottom left are droplets which deform like the right hand example in figure 2.5. The last cluster are points which have a

small active fraction, elongate along the axis of motion and have a highly curved active region. We can also see here that some of these point have large error bars. This is due to some droplets transitioning between different swimming modes which we discuss more in section 2.3.4.1.1.

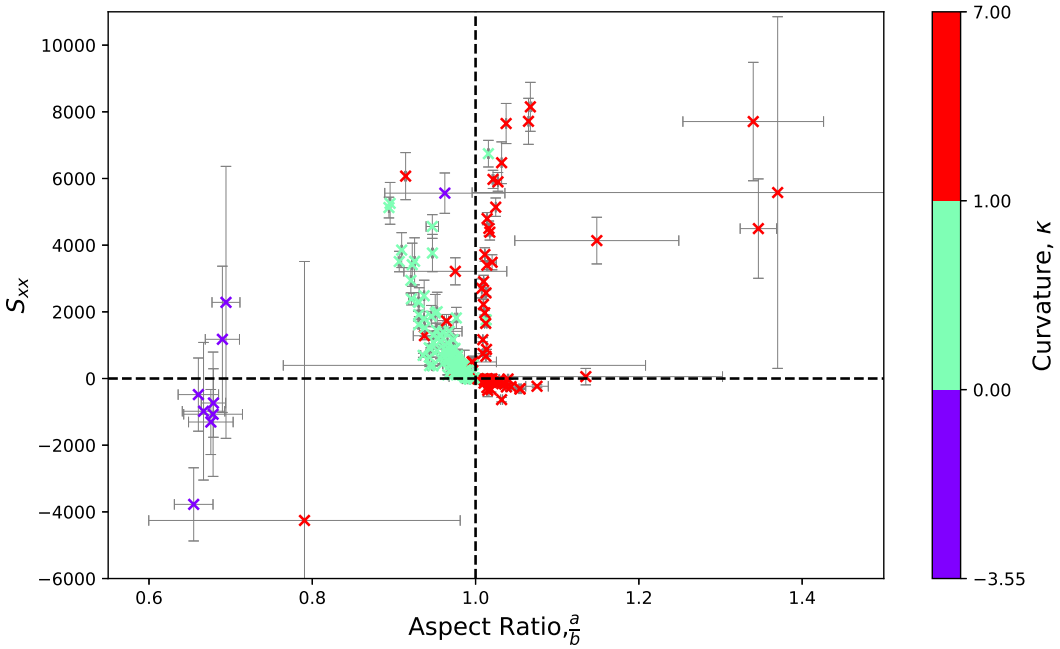

FIGURE 2.15: The stresslet, S_{xx}, against the aspect ratio of the droplets. The colour bar signifies curvature of the active region, it is split into negative curvature (purple), lower curvature than a unit circle (mint) and curvature higher than a unit circle (red). The vertical dashed line at $\frac{a}{b} = 1$ is where the droplet is a circle, so divides the drops into those elongated along their axis of motion, and perpendicular to the axis of motion. The dashed horizontal line divides the positive and negative stresslets.

We next plot the stresslet against the aspect ratio in figure 2.15. Recall from section 1.2.3.1 in the introduction that the sign of the stresslet is one way to classify squimers into pushers or pullers. We will use this terminology here where a positive stresslet corresponds to a pusher and a negative stresslet corresponds to a puller. Somewhat unintuitively, just from looking at the dipole moments, in the literature deformable squirmers elongate perpendicular to the axis of motion if they are pushers and elongate along the axis of motion if they are pullers [76]. Excluding the droplets with negative curvature, in figure 2.15 the droplets that were part of the largest cluster in figure 2.14 obey this trend, and we see a negative correlation between S_{xx} and aspect ratio. However, we also have an additional group of points, which do not obey the trend. These are pushers located in the upper right quadrant in figure 2.15, and correspond to the lower right quadrant cluster in figure 2.14. These pushers elongate along their axis of motion rather than perpendicularly as expected form looking at the dipole moments in figure 2.6. Looking at the diagram in figure 2.6, we hypothesise that the stresslet may be dominant here, and the quadrupole dominant for the main cluster behaviour. We plot figure 2.16 to investigate further.

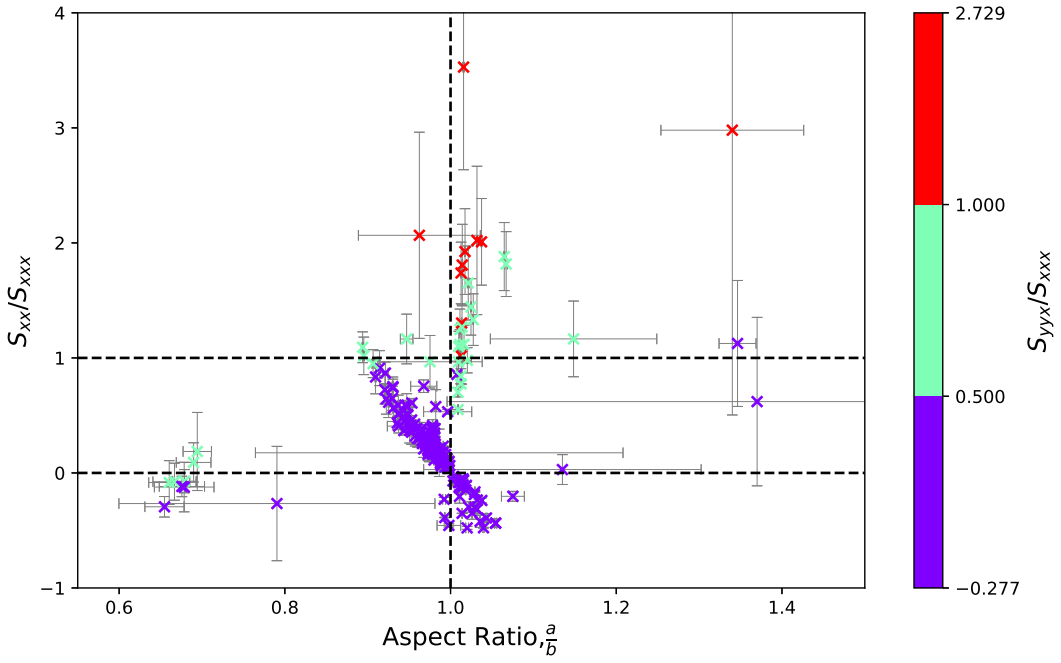

FIGURE 2.16: The ratio of the stresslet, S_{xx}, to symmetric quadrupole moment component, S_{xxx}, against the aspect ratio of the droplets. The colour bar shows the ratio of S_{yyx} and S_{xxx}, it is split into where $S_{yyx} > S_{xxx}$(red), where $S_{yyx} > \frac{1}{2}S_{xxx}$ (mint) and where $S_{xxx} > S_{yyx}$ (purple). The vertical dashed line at $\frac{a}{b} = 1$ is where the droplet is a circle, so divides the drops into those elongated along their axis of motion, and perpendicular to the axis of motion. The dashed horizontal line at zero divides pushers and pullers, the dashed horizontal line at 1 shows where $S_{xx} = S_{xxx}$.

In figure 2.16 the cluster in purple corresponds to the major cluster where the active fraction > 0.2 in figure 2.14. The points in red and mint with aspect ratio > 1 in figure 2.16 correspond to the bottom right cluster in figure 2.14 and the cluster at the bottom left in figure 2.16 is the cluster with negative curvature in figure 2.14. As expected, in figure 2.16 we see that where the symmetric quadrupole term S_{xxx} is dominant over the stresslet,S_{xx}, the droplet deforms in the opposite direction to the stresslet. When the stresslet is dominant, or when S_{yyx} is greater than $\frac{1}{2}S_{xxx}$ we see the droplets elongate along the axis of motion.

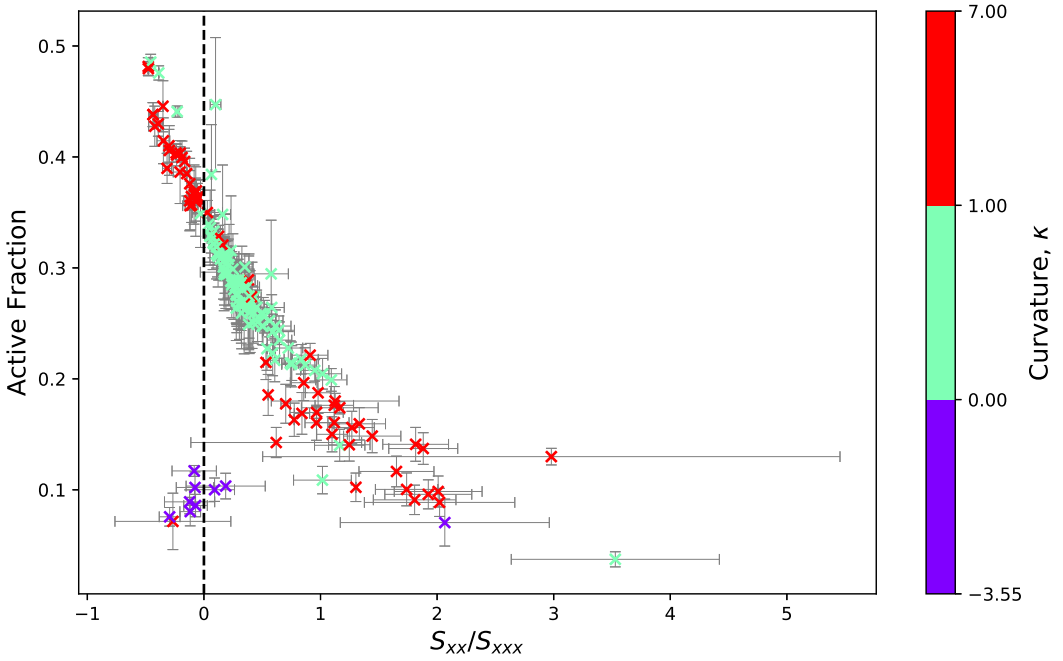

FIGURE 2.17: The active fraction plotted against the ratio of the stresslet S_{xx} to S_{xxx}. The colour bar signifies curvature of the active region, it is split into negative curvature (purple), lower curvature than a unit circle (mint) and curvature higher than a unit circle (red). The vertical dashed line at 0 divided pushers and pullers.

We next relate the length of the active region to to force moments. We see in figure 2.17 that, excluding the droplets with negative curvature deformations, the active fraction is strongly negatively correlated with the ratio of the stresslet and the symmetric quadrupole component S_{xxx}. This is regardless of the aspect ratio or curvature of the active region (provided it's not negative).

2.3.4.1 Deformation of the active region

As seen in figure 2.5, we see deformations of the active region, which gains positive or negative curvature depending on the parameters. As deformations more complicated than an ellipse only occur for droplets with a difference in external and internal viscosities we surmise that the origin of this deformation is in the second term on the right hand side of (2.50). We note that for droplets with a viscosity difference that $F_{yxy} \neq F_{yyx}$ due to this additional term.

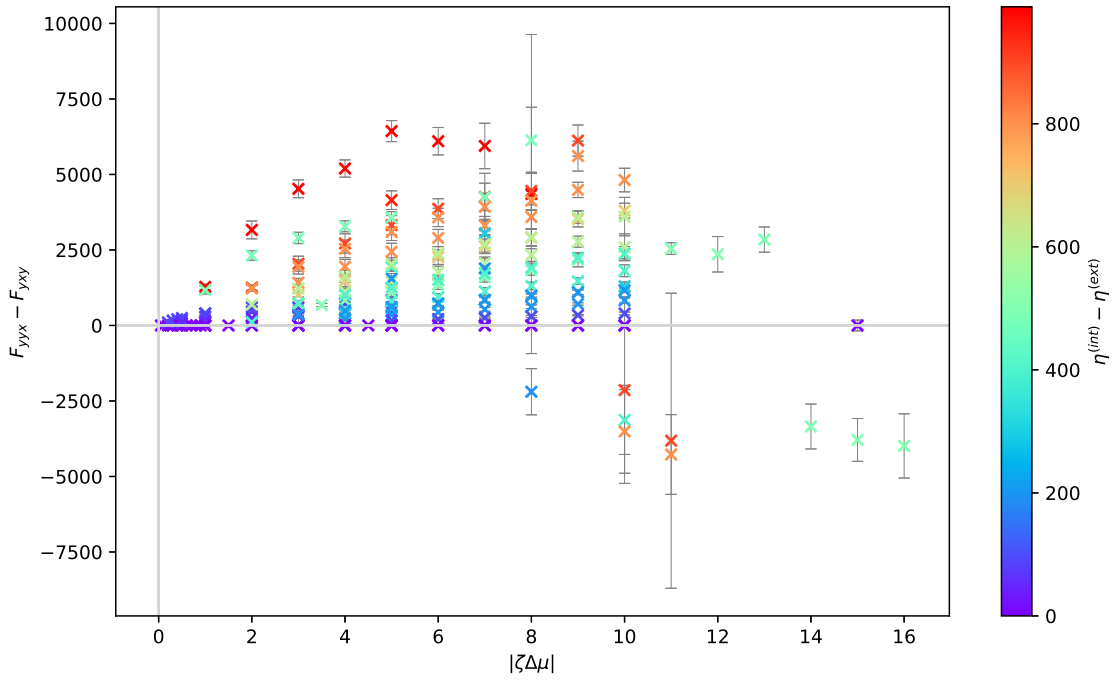

FIGURE 2.18: Plot of $F_{yyx} - F_{yxy}$ against activity. Where the colourbar denotes difference between internal and external viscosity.

In figure 2.18 we plot $F_{yyx} - F_{yxy}$ to remove the first term from $F^{(3)}_{ijk}$ defined in (2.50). Upon investigation of the data we find all of the points which are negative correspond to a region of negative curvature at the rear of the cell resulting in a kidney bean like shape as seen in the right hand picture in figure 2.5. The rest of the points have positive curvature.

In figure 2.19 we see that the vast majority of droplets show a strong positive correlation between the aspect ratio and the curvature of the active region. So we see that droplets which elongate along the axis of motion are likely to have curvature greater than 1 and vice versa for droplets which elongate perpendicular to the axis of motion.

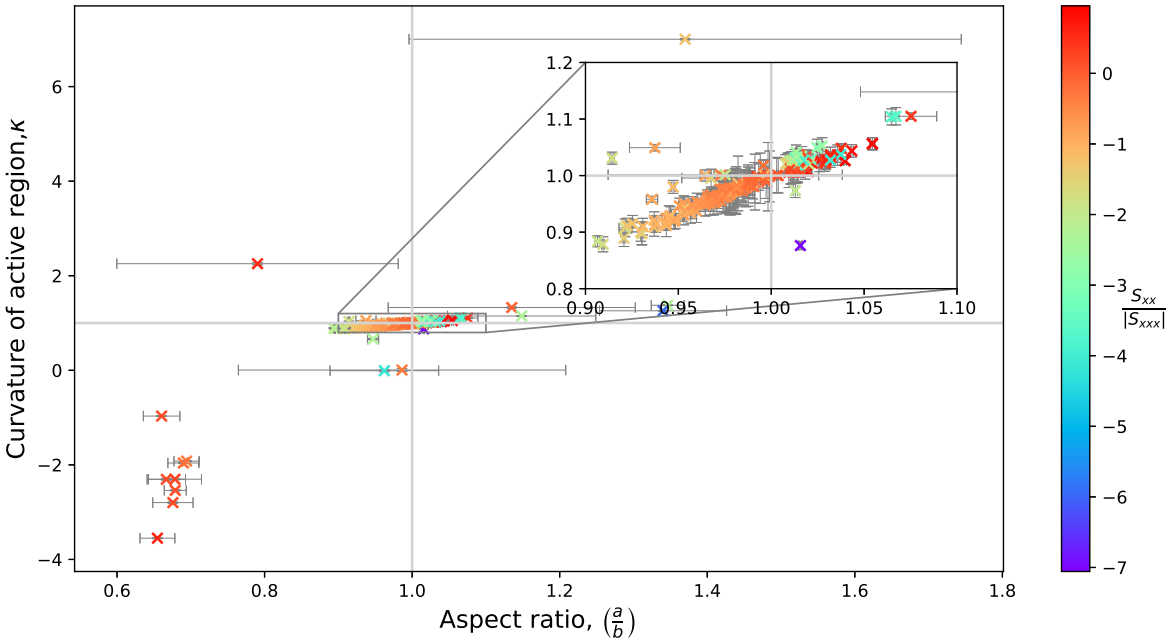

FIGURE 2.19: Plot showing the correlation between the aspect ratio and curvature of the active region. The colour bar indicates the value of $\frac{S_{xx}}{|S_{xxx}|}$ for each droplet.

The active region is where forces are being exerted on the droplet. The normal force balance here causes the departure of the active region from a circular state. Due to the area constraint on the droplet, included to model volume conservation in cells, when the active region is deformed the rest of the droplet must deform as a consequence. This helps us to understand the deformation of the quadrupole dominant droplets. If the back of the droplet is flattened due to high tension, the droplet will elongate perpendicular to the axis of motion in order to minimise the boundary length.

2.3.4.1.1 States in transition We noted at the beginning of this section that some droplets have large error bars due to switching between the three observed clusters of behaviour shown in figure 2.14. For pusher type droplets of a given viscosity difference we see a crossover in behaviour from elongated along the axis of motion to kidney bean shaped (negative curvature of active region) as the activity is increased. Some droplets transition between these states.

In figure 2.20 we plot the non-zero symmetric quadrupole moment components for a droplet which transitions between the elongated and kidney bean state over the course of a simulation. We observed in 2.3.4 that for elongated droplets the stresslet was dominant and $S_{yyx} > S_{xxx}$. We see this is the case here when the drop is in the extended phase (see figure 2.21 for the stresslet). When the droplet is in the bean state, $S_{xxx} > S_{yyx}$ and the stresslet decreases briefly changing sign.

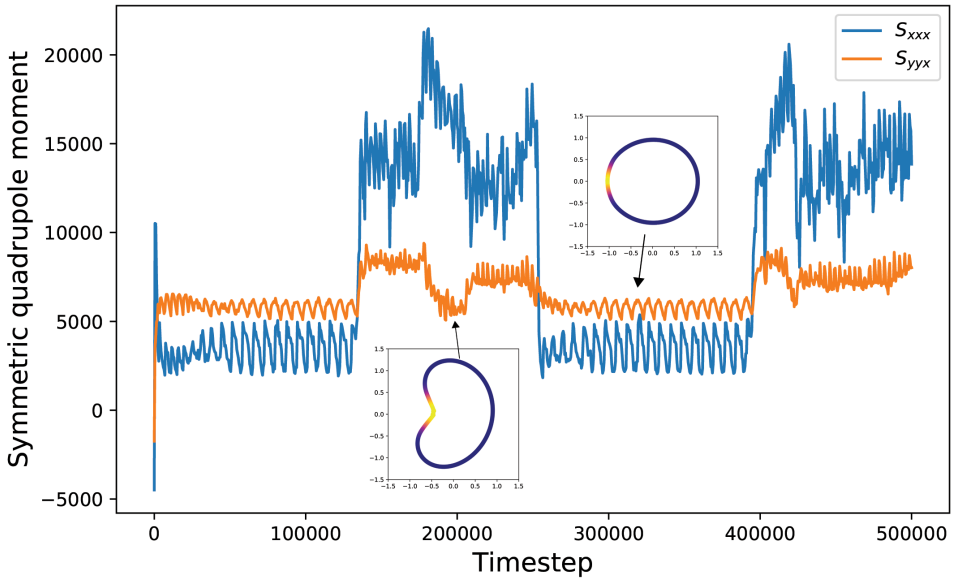

FIGURE 2.20: Plot of the symmetric quadrupole moments over the course of the simulation for a droplet with $\zeta\Delta\mu = -10$, $\eta^{(int)} = 1000$, $\eta^{(ext)} = 100$. The insets give examples of the shape at a certain time point indicated with arrows.

We see in figure 2.21 that the droplet aspect ratio and curvature change simultaneously with the stresslet. When the stresslet decreases and the quadrupole moments become dominant, the droplet deforms perpendicularly to the axis of motion rather than along it. The curvature changes sharply from positive to negative.

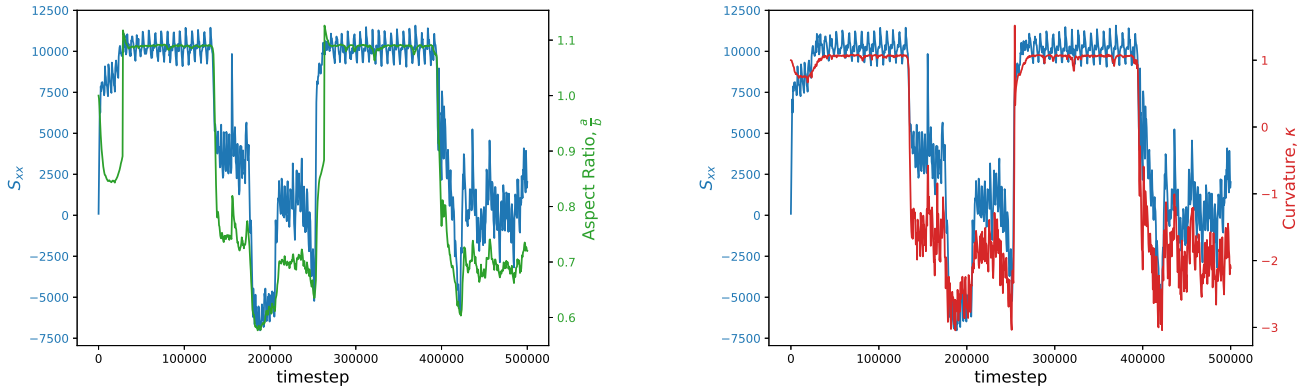

(A) (B)

FIGURE 2.21: Plots of S_{xx} super imposed with a) the aspect ratio and b) the curvature. For a droplet with $\zeta\Delta\mu = -10$, $\eta^{(int)} = 1000$, $\eta^{(ext)} = 100$.

2.3.5 Squirmer motion

As observed in [79], the motion of our model droplet can be mapped on to that of a squirmer. A squirmer is a basic model for a spherical swimmer in Stokes flow [63]. It's

velocity field is given by an expansion of Legendre polynomials. By truncating the theta component of the velocity at 2nd order it can be approximated as:

$$v_\theta(R,\theta) = B_1 \sin(\theta) + \frac{B_2}{2}\sin(2\theta) \tag{2.63}$$

The squirmer parameter is defined as: $\beta = \frac{B_2}{|B_1|}$, where B_2 is related to the force dipole and B_1 is related to the source dipole. For positive β the squirmer is classified as a puller, meaning that v_θ, is strongest at the front (as defined by the direction of the centre of mass velocity) of the droplet and so most of the propulsion comes from the front. If β is negative the reverse is true, and the droplet is classified as a pusher. For $\beta = 0$ the droplet is designated a neutral squirmer. Figure 2.22 shows example flow fields for a pusher, a puller and a squirmer.

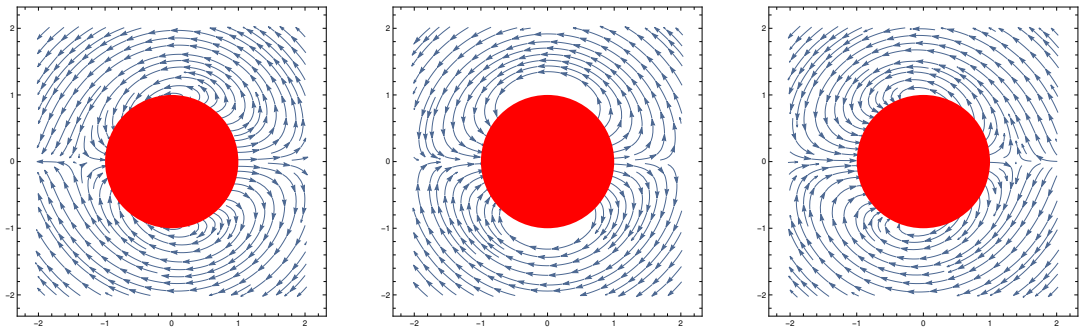

(A) Flow field for a pusher.$\beta < 0$

(B) Flow field for a neutral squirmer.$\beta = 0$

(C) Flow field for a puller. $\beta > 0$

FIGURE 2.22: Example flow fields for the different types of squirmer, generated from equation (2.63). Here, $B_1 = 1$, $B_2 = \{-1, 0, 1\}$

We can fit the boundary velocity from simulations to (2.63) to find values for B_1 and B_2 for our droplets. Plotting all droplets,in figure 2.23 we see that droplets in simulations with a lower total viscosity are more likely to be pullers while droplets with a higher total viscosity are likely to be pushers. This trend is partly due to lower viscosity droplets supporting a lower maximum activity before the droplet deforms to the extent of a topological singularity (where the boundary touches itself) which is beyond the scope of our simulations.

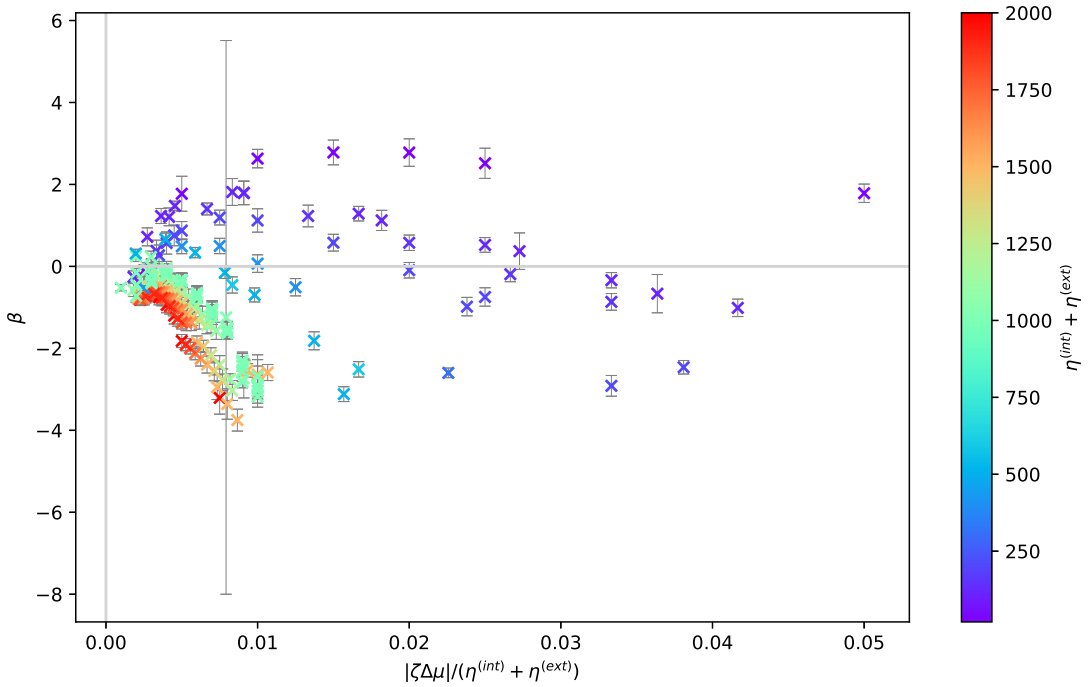

FIGURE 2.23: Plot of the squirmer parameter, β, for motile droplets, the colour bar denotes the viscosity sum.

We see in figure 2.23 that for high enough activities droplets which are pullers at lower activities become pushers. Due to the nature of our system, pullers are rare as in order for propulsion to come mostly from the front the active region must cover at least half the boundary. This requires a low activity to allow for the concentration profile to spread out so far, and if the activity is low the droplet will only be motile in lower viscosity fluids, this is why we see pullers only for lower viscosity simulations.

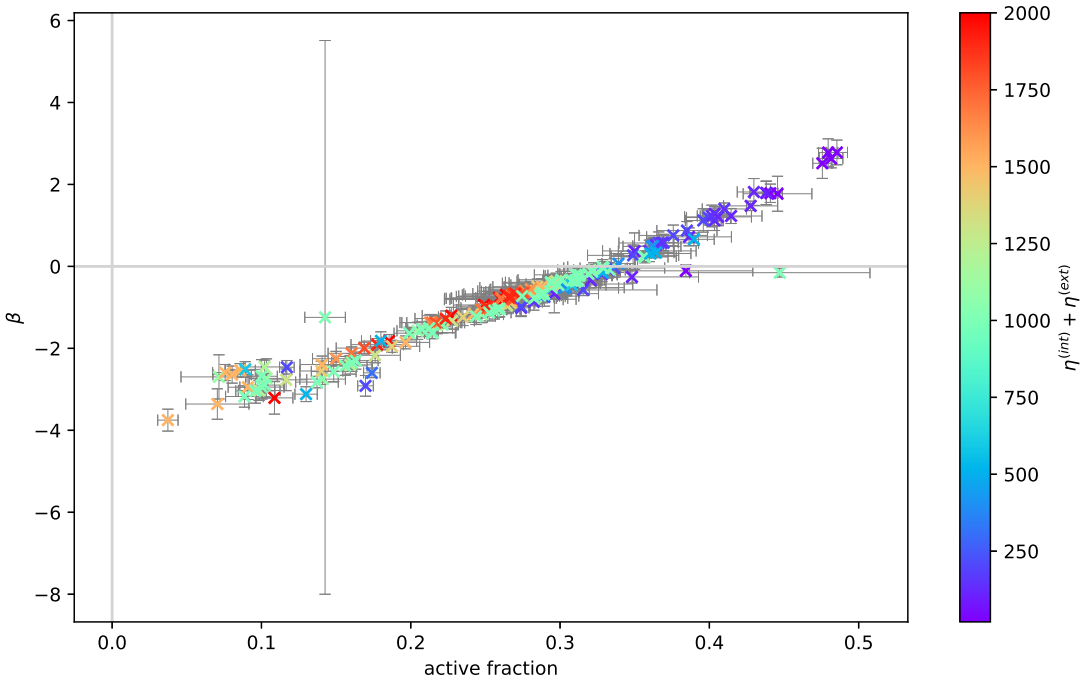

FIGURE 2.24: Plot of the squirmer parameter, β, against the active fraction of a droplet. Where the colour bar denotes the total viscosity. The graph shows a clear positive correlation.

If we plot beta against the active fraction, which is the length of the active region compared to the total boundary length, we see there is a clear correlation, figure 2.24. Both values are related to the tangential velocity at the boundary. β is constructed from coefficients found by fitting the boundary veolcity, and the active region length is a direct consequence of the advection-diffusion equation for concentration for which the advection velocity is the tangential velocity at the boundary. The points of highest force on the boundary are also at the gradient between the high and low concentration regions, so if there is a very small active region the flow at the boundary will be greatest in the rear of the droplet and it will be a pusher and vice versa.

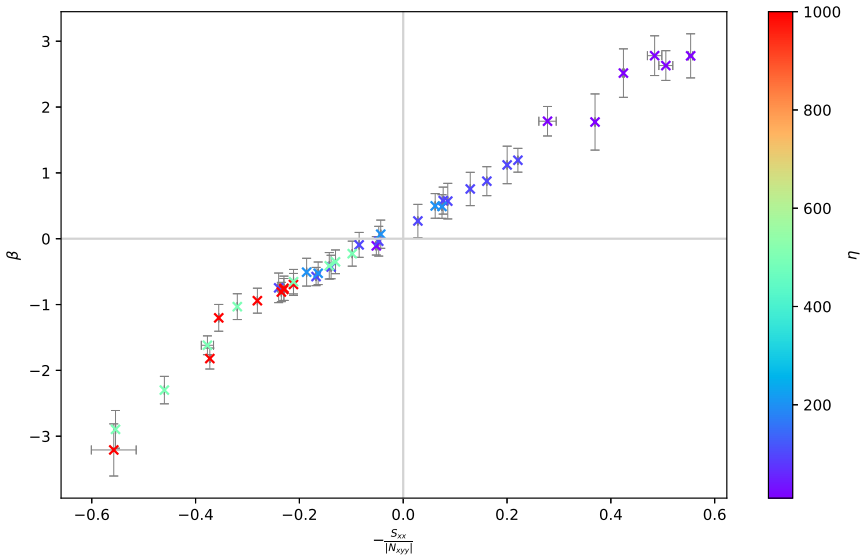

FIGURE 2.25: The squirmer parameter β, plotted against the ratio of the stresslet and the source dipole related part of the quadrupole moment $|N_{xyy}|$. The colour denotes the viscosity, $\eta = \eta^{(int)} = \eta^{(ext)}$

We can relate the squirmer parameter to force moments. From the definition of β, it is the ratio of the force dipole and source dipole [96]. In figure 2.25 we find a linear relationship between our fitted values of beta and the ratio of the stresslet and the source dipole related part of the quadrupole moment $|N_{xyy}|$. When we try applying this to droplets with a viscosity difference we find, as with the velocity in section 2.3.3.4, we need to apply a correction to our expression for β as $|N_{xyy}| \neq |N_{yxy}| \neq |N_{yyx}|$ when we have a viscosity difference. In figure 2.26 we find a linear relationship between β and the ratio of the stresslet with the corrected source dipole part of the quadrupole moment. The off-trend points in the bottom left are the droplets which are very deformed away from an ellipse.

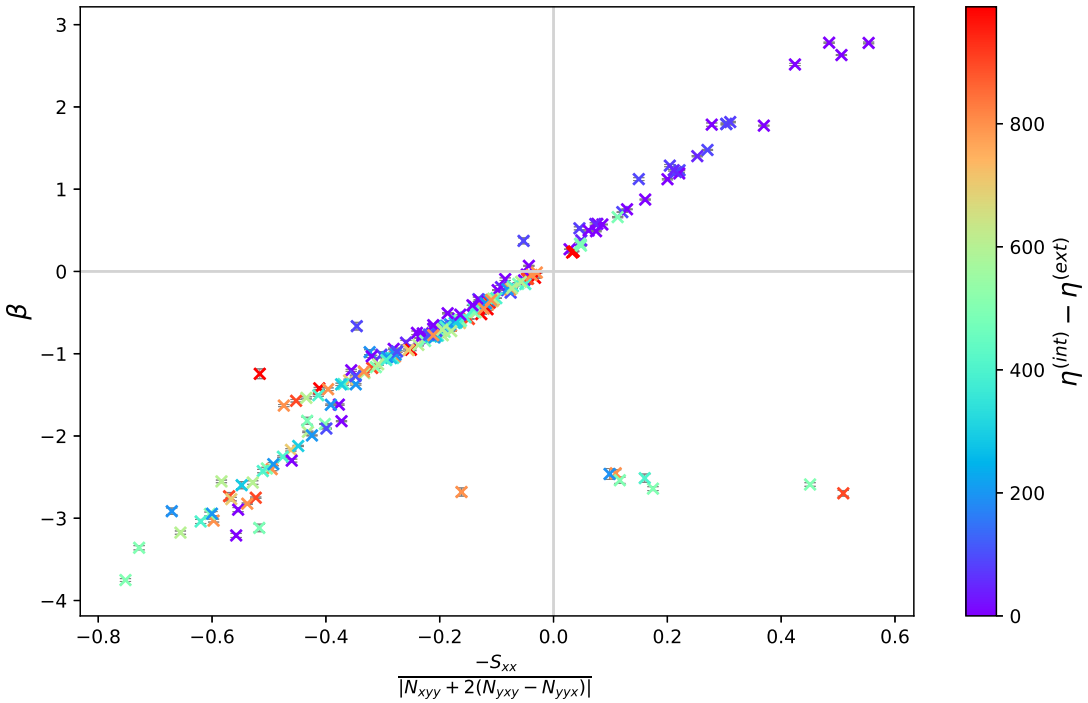

FIGURE 2.26: The squirmer parameter β, plotted against the ratio of the stresslet and the source dipole related part of the quadrupole moment corrected to account for the viscosity difference. The viscosity difference is indicated by the colour bar.

β is a useful first approximation for classifying droplet swimming types, however it is truncated at the second mode which corresponds to the force dipole and so any effects from higher order force moments are ignored. In our model the quadrupole moment plays a significant role. If we look at the flow fields we see 3 distinct patterns, shown in figure 2.27, which correspond to the pusher/puller/neutral squirmer shown in figure 2.22.

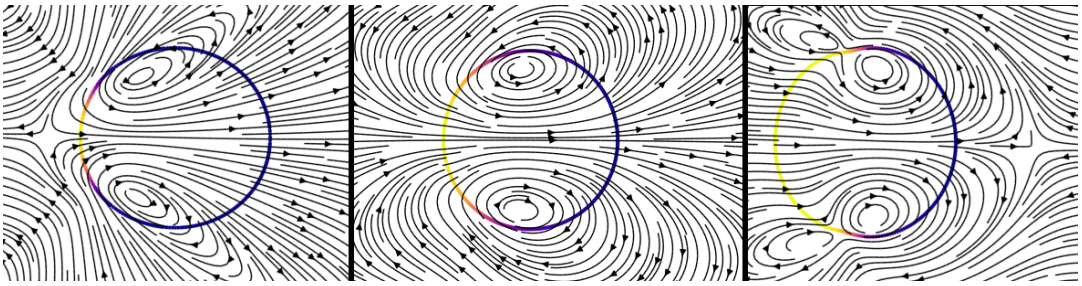

FIGURE 2.27: Example flow fields from our simulations for the different types of swimmer we see in our simulations, to the left a pusher, middle a squirmer and to the right a puller.

By looking at the flow fields in figure 2.27 we classify the swimmers based on the position of the defects in the flow field. For the squirmer where the quadrupole is dominant (middle) we see the stream lines are continuous along the axis of motion of

the droplet and any defects are offset from this axis as in the centre droplet in figure 2.27. For the extreme pusher type swimmer we see a defect in the velocity field at the rear of the droplet and for the extreme puller we see a defect at the front of the droplet, (the left and right droplets in figure 2.27 respectively). These flow fields correspond to the the deformation groups we observed. The droplets for which S_{xxx} is dominant have flow fields resembling that of the centre droplet in figure 2.27. The droplets which had a positive stresslet S_{xx} and elongated along the axis of motion have a flow field like the left hand droplet in figure 2.27 with a defect directly behind the droplet.

2.4 Summary

In this chapter we have introduced our model of an active droplet for a cell migrating under amoeboid motion. Having established the linear behaviour of the droplet we used numerical methods to examine the non-linear behaviour of our coupled system.

We varied the viscosity of the droplet and the surrounding fluid and found the relative slip between the two fluids decreases the minimum activity required for migration and also leads to deformation away from a circular shape of the droplet.

We explored how the droplets deform and the roles that the stresslet and symetric quadrupole moments play in determining whether a droplet will elongate along or perpendicular to the axis of motion. We also looked at how the length of the active region is important in determining the balance of force moments.

We then mapped the swimming behaviour of our droplets to the squirmer model for a swimmer and related the squirmer parameter, β to the force moments calculated from our simulations.

2.A Force moment derivation

Beginning with the boundary integral representation of the velocity for a 2D droplet with viscosity η_2 in a fluid with viscosity η_1. The viscosity ratio is $\lambda = \frac{\eta_2}{\eta_1}$[91].

$$v_j^{(1)}(\vec{x}_0) - v_j^{\infty}(\vec{x}_0) = -\frac{1}{4\pi\eta_1}\int_\Gamma \mathcal{G}_{ji}(\vec{x_0},\vec{X})\Delta f_i(\vec{X})\mathrm{d}s(\vec{X}) + \frac{1-\lambda}{4\pi}\int_\Gamma v_i(\vec{X})\mathcal{T}_{ijk}(\vec{X},\vec{x}_0)n_k(\vec{X})\mathrm{d}s(\vec{X}) \tag{2.64}$$

Here $\vec{v}^{\infty}$ is the ambient velocity, this is 0 in our case, $\vec{x}_0$ is a point in the ambient fluid. $\vec{X}$ is the boundary, Γ, coordinate, consistent with the rest of the thesis. $\mathcal{G}_{ij}$ is the Green's function for the Stokes equations and $\mathcal{T}_{ijk}$ is it's associated stress tensor. $\Delta f_i = (\sigma_{ij}^{(2)} - \sigma_{ij}^{(1)})n_j$ where σ_{ij} is the stress tensor and $\vec{n}$ the outward normal. In our particular case $\Delta f_i = F_i$.

The first term is called the single layer potential and represents a distribution of point forces on the boundary. The second term is called the double layer potential, this can be decomposed into 2 parts, the pressure and a viscous component. The viscous part corresponds to a distribution of point force dipoles.

We can Taylor expand the Green's function with respect to $\vec{X}$ around some point $\vec{x}_c$ near or inside the boundary, to get a multipole expansion of the velocity. We make use of the following identities:

$$\mathcal{G}_{ij}(\vec{X},\vec{x}_0) = \mathcal{G}_{ji}(\vec{x}_0,\vec{X}) \tag{2.65}$$

$$\mathcal{T}_{ijk}(\vec{X},\vec{x}_0) = -\delta_{ik}p_j + \frac{\partial\mathcal{G}_{ij}}{dX_k}(\vec{X},\vec{x}_0) + \frac{\partial\mathcal{G}_{ij}}{dX_k}(\vec{X},\vec{x}_0) \tag{2.66}$$

(p_i is the pressure vector associated with the Green's function)
Combining the expressions and collecting terms, we get:

$$v_j^{(1)}(\vec{x}_0) = -\frac{1}{4\pi\eta_1}\Big(\ \mathcal{G}_{ij}\int_\Gamma F_i\mathrm{d}s - \frac{\partial\mathcal{G}_{ij}}{\partial X_k}\int_\Gamma (X_k - x_{c,k})F_i$$

$$-\eta_1(1-\lambda)(v_i(\vec{X})n_k(\vec{X}) + v_k(\vec{X})n_i(\vec{X}))\mathrm{d}s\ \Big) + \frac{\partial^2\mathcal{G}_{ij}}{\partial X_k\partial X_l}\int_\Gamma (X_k - x_{c,k})(X_l - x_{c,l})F_i$$

$$-\eta_1(1-\lambda)((X_l - x_{c,l})(v_i(\vec{X})n_k(\vec{X}) + v_k(\vec{X})n_i(\vec{X})))\mathrm{d}s + \ldots \tag{2.67}$$

The integral parts correspond to the force moments:

$$v_j^{(1)}(\vec{x}_0) = -\frac{1}{4\pi\eta_1}\left(\mathcal{G}_{ij}F_i^{(1)} - \frac{\partial\mathcal{G}_{ij}}{\partial X_k}F_{ik}^{(2)} + \frac{\partial^2\mathcal{G}_{ij}}{\partial X_k\partial X_l}F_{ikl}^{(3)} + \ldots\right) \tag{2.68}$$

We can re write these in terms of polar coordinates, choosing $x_c = r = 0$, as we have in section 2

$$F_i^{(1)} = \int_0^{2\pi} F_i R \mathrm{d}\theta \tag{2.69}$$

$$F_{ij}^{(2)} = \int_0^{2\pi} F_i r_j R \mathrm{d}\theta - (\eta^{(ext)} - \eta^{(int)}) \int_0^{2\pi} v_j \hat{n}_i + v_i \hat{n}_j R \mathrm{d}\theta \tag{2.70}$$

$$F_{ijk}^{(3)} = \int_0^{2\pi} F_i r_j r_k R \mathrm{d}\theta - (\eta^{(ext)} - \eta^{(int)}) \int_0^{2\pi} (v_j \hat{n}_i + v_i \hat{n}_j) r_k R \mathrm{d}\theta \tag{2.71}$$

Chapter 3

The effects of confinement on an active droplet

In the chapter 2 we modelled cells confined by a viscous fluid. Here we explore confinement by solid walls. In the biological context this could be confinement in small blood or lymphatic vessels or by the extracellular matrix.

In vivo cells migrate in highly confined environments. In particular the mode of migration we are modelling, amoeboid motion, is observed when a cell is strongly confined [55]. In this chapter we will initially look at the effect of confinement by rigid walls which we model using a numerically enforced non-slip condition, in order to find a baseline behaviour to which we can compare droplets confined by deformable walls (in chapter 4).

3.1 Confinement by rigid walls

Here we confine cells using non-slip boundary conditions at the edge of our simulation domain. In order to do this we must modify our Stokes solver to account for no-slip boundaries at the channel wall, while maintain periodic boundaries in the x direction. We still use a Fourier transform based method on a staggered grid as described in section 2.2, however in the y-direction discrete sine and cosine transforms(DST, DCT) are used on the appropriate grids to enforce the no-slip boundary condition.

We follow methods from [97]. The staggered grid is set up so the boundary will be at the grid point for the y components and the scalar quantities, whereas the boundary will fall between grid points for the x components. We must also consider that we are solving, initially, for the intermediate velocity, so the no-slip boundary condition becomes:

$$\vec{v}^* = \nabla\phi, \tag{3.1}$$

as our boundary condition on ϕ is $\frac{\partial\phi}{dy} = 0$ at the wall, $\vec{v}^* = (\frac{\partial\phi}{\partial x}, 0)$. For v_y^* the boundary condition is implemented directly through the use of DSTs, but we now have an inhomogeneous boundary condition for v_x^* which we must account for. We can split v_x^* into a part which is zero at the boundary, $v_x^{*'}$, and a part which is zero everywhere except the boundary,v_x^{*B}.:

$$\nabla^2 v_x^* = \nabla^2 v_x^{*'} + \nabla^2 v_x^{*B} \tag{3.2}$$

v_x^{*B} is a known quantity and so we can take this term to the right hand side to solve the equation.As v_x^{*B} is zero everywhere except on the boundary the finite difference equation becomes:

$$v_{x\,i+1,j}^{*'} + v_{x\,i-1,j}^{*'} + v_{x\,i,j+1}^{*'} + v_{x\,i,j-1}^{*'} - 4v_{x\,i,j}^{*'} = -v_{x\,N_y,j}^{*B} + \frac{1}{\eta} f_{x_{i,j}} \tag{3.3}$$

So we are solving the equation:

$$\nabla^2 v_x^{*'} = \frac{1}{\eta} f_x - \partial_x \phi|_{y=\pm\frac{Ly}{2}} \tag{3.4}$$

Along the x direction we use an FFT, as we did in section 2.2. For Dirichlet conditions (where the value of the quantity is specified, as opposed to the value of the derivative for Neumann boundary conditions) we use a discrete sine transform (DST) in the y direction for solving for v_x^* and v_y^*. Due to the staggered grid we must use different versions for the two grids in order for the no-slip condition to be applied in the correct place. For the y grid we use DST1 to forward and backwards transform the equations. For the x grid we use DST2 to forward transform the equations and DST3 to transform back.

The discrete transformed Laplacian has a slightly different form to account for the DST in the y direction:

$$\hat{D}^2_{m,n} = \left(e^{\frac{2\pi i m}{Nx}} + e^{\frac{-2\pi i m}{Nx}} + e^{\frac{\pi i (n+1)}{(Ny-1)}} + e^{\frac{-\pi i (n+1)}{(Ny-1)}} - 4 \right). \tag{3.5}$$

To solve for the pseudo-pressure in equation (2.23) we use the boundary condition $\frac{\partial \phi}{dy} = 0$ at the boundary. As this is a Neumann boundary condition we use a discrete cosine transform (DCT) specifically DCT2 when transforming forwards and DCT3 when transforming back. The new form of the Laplacian for this case is:

$$\hat{D}^2_{m,n} = \left(e^{\frac{2\pi i m}{Nx}} + e^{\frac{-2\pi i m}{Nx}} + e^{\frac{\pi i n}{(Ny-1)}} + e^{\frac{-\pi i n}{(Ny-1})} - 4 \right). \tag{3.6}$$

For the full definition of the discrete transforms see Appendix 3.A.

3.1.1 Channel Length

By changing the y boundaries from periodic to non-slip we can confine a droplet in a channel. In the fully periodic case, increasing the simulation box size does not affect the steady state translational velocity reached by active droplets. Here we confine a droplet in a channel and vary the length of the channel to see the effect.

In a channel which is the width of the diameter of an undeformed droplet, $w = 2R_0$, there is not much room for retrograde channel flow when the droplet has deformed into a steady shape. Consequently, the droplet ends up pushing the fluid in front of it and as we have periodic boundary conditions this sets up a net flow along the channel which then interacts with the droplet itself. Alternatively, we can think of our droplet

in a periodic channel as a series of droplets which affect each other. We can view this as a model for leader-follower dynamics in a confined space.

We see, in figures 3.1 and 3.2, that as we extend the length of the channel the centre of mass velocity of the droplet can be fit with a decaying exponential function, $Ae^{-\frac{x}{b}} + c$. Here we choose to consider the case where $\eta = \eta^{(int)} = \eta^{(ext)}$ in order to focus on the channel effects. We ran a series of simulations for $|\zeta\Delta\mu| = \{2, 4, 5\}$ at $\eta = 100$ and for $|\zeta\Delta\mu| = 4$ varying $\eta = \{50, 100, 200\}$. For all of these cases the fit gave $b \sim 10$, despite different parameter values for the activity and viscosity of the droplets, implying that b is related to the geometry of the channel. The value of the plateau, given by c, is non-zero implying that the effect of self interaction (due to periodic boundaries)/interaction with other droplets decays exponentially with channel length, down to a finite speed at which the droplet would move if it were infinitely far from another droplet. A represents the the strength of the self-interaction effects.

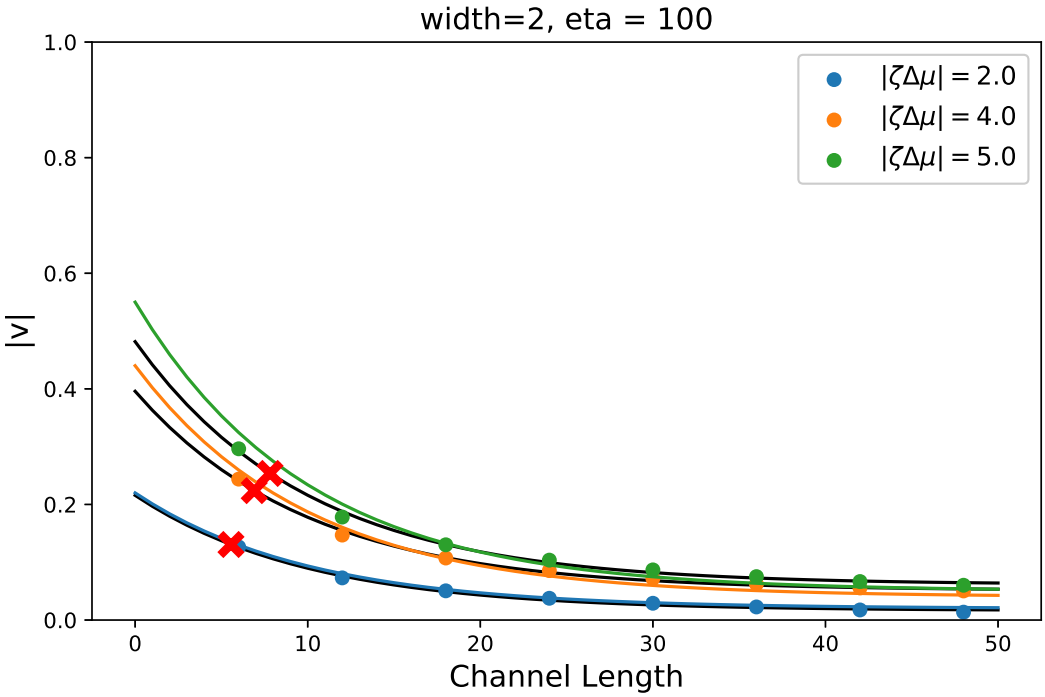

FIGURE 3.1: Centre of mass velocity of droplets with $|\zeta\Delta\mu| = \{2, 4, 5\}$ in channels of width, $w = 2R_0$ with $\eta = 100$, for varying lengths. The black lines are fits where $|v| = Ae^{-\frac{L}{10}} + c$, where $A = \{0.20, 0.34, 0.42\}$ and $c = \{0.016, 0.051, 0.061\}$. The coloured lines are our proposed analytical expression (3.7) where $A = \frac{10|\zeta\Delta\mu|}{\eta}$ and $c = \frac{|\zeta\Delta\mu|}{\eta}$. The red crosses are the steady state velocity of the droplets if they were unconfined, as we don't have a length value for these, we place them on the black fit line.

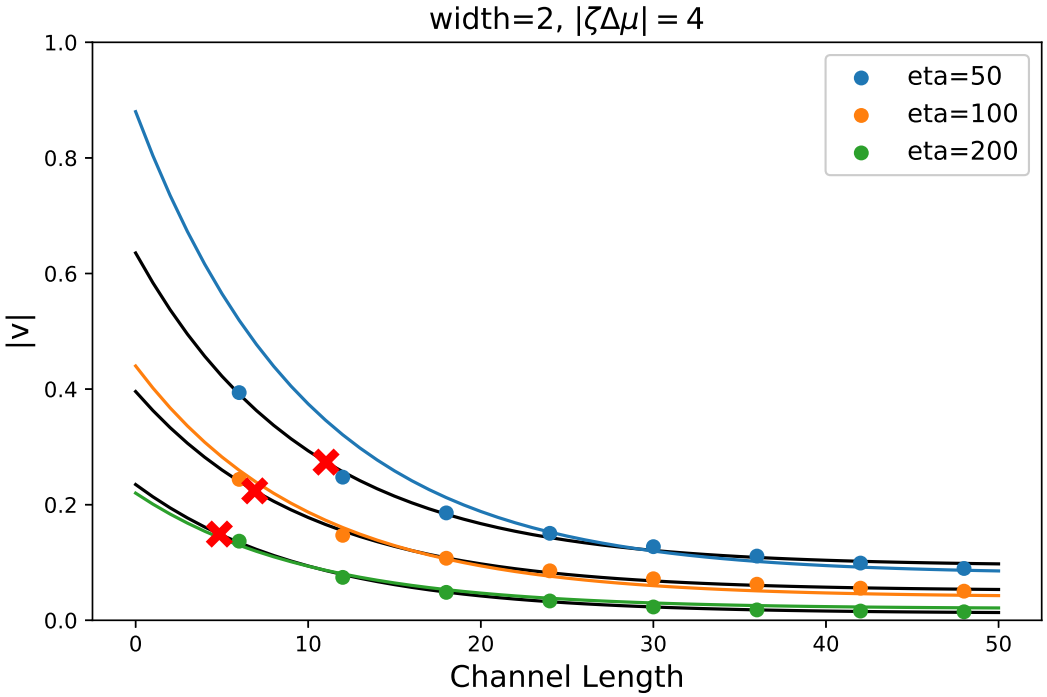

FIGURE 3.2: Centre of mass velocity of droplets with $|\zeta\Delta\mu| = 4$ and $\eta = \{50, 100, 200\}$ in channels of width, $w = 2R_0$ for varying lengths. The black lines are fits where $|v| = Ae^{-\frac{l}{10}} + c$, where $A = \{0.54, 0.34, 0.22\}$ and $c = \{0.094, 0.051, 0.012\}$. The coloured lines are our proposed analytical expression (3.7) where $A = \frac{10|\zeta\Delta\mu|}{\eta}$ and $c = \frac{|\zeta\Delta\mu|}{\eta}$. The red crosses are the steady state velocity of the droplets if they were unconfined, as we don't have a length value for these, we place them on the black fit line.

The coloured lines in figures 3.1 and 3.2 correspond to an analytical function for $|v|$, that we propose:

$$|v| = \frac{10|\zeta\Delta\mu|}{\eta} e^{-\frac{l}{10}} + \frac{|\zeta\Delta\mu|}{\eta} \tag{3.7}$$

This works well for slower droplets, but for increased activity or decreased viscosity this expression over estimates the velocity in shorter channels. As with our study of the velocity of droplets with different viscosities in chapter 2, A and c here are likely non-linear functions of η and $|\zeta\Delta\mu|$ for which the linear form (3.7) works well for small $\frac{|\zeta\Delta\mu|}{\eta}$

3.1.2 Channel Width

We next look at the effect of widening the channel. We again chose to use $\eta = \eta^{(int)} = \eta^{(ext)} = 100$ as a viscosity value in the middle of our previous range, and keeping the viscosity equal inside and outside of the droplet to focus on confinement effects. We choose to look at $\zeta\Delta\mu$={-1,-2,-3,-4,-5}, as in the unconfined case this gives us both positive and negative values of the stresslet S_{xx}, as seen in figure 3.3. For the channel length we chose $12R_0$ (unless otherwise stated), a trade off between channel length

and simulation runtime. We compare channel widths $w = \{2, 2.5, 3, 3.5, 4, 4.5, 5\}R_0$ and with the unconfined case.

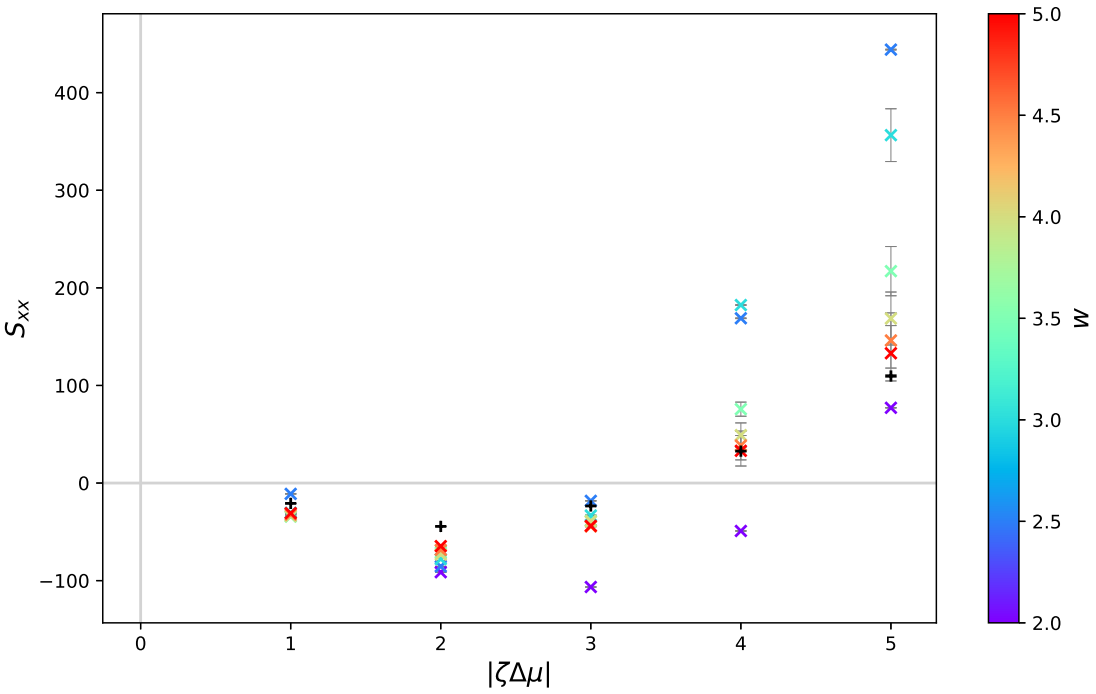

FIGURE 3.3: Stresslet for droplets with $\eta = 100$ for different activities, in channels ranging from width, $w = [2, 5]R_0$, which is indicated by the colour.Black pluses indicate the stresslet for unconfined droplets with the same parameters.

3.1.2.1 Droplet Velocity

The speed of the droplets in channels generally increases as the channel gets wider. We see in figure 3.4 that the velocity of a droplet in channels with width greater than 4 is comparable to the unconfined speed of the droplet.

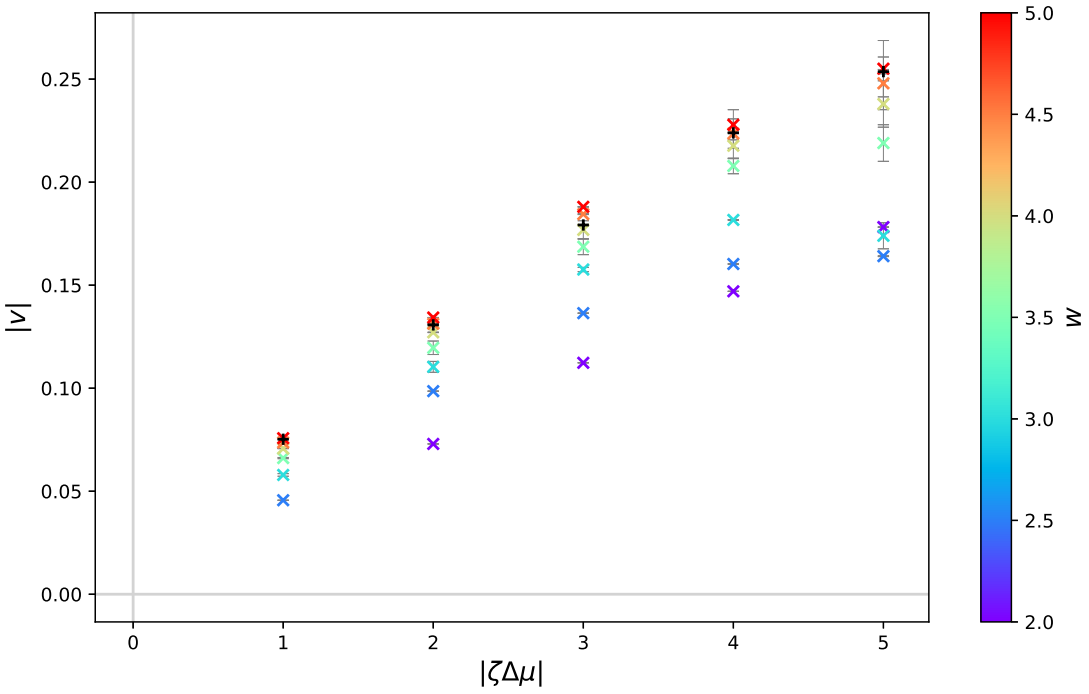

FIGURE 3.4: Speed of droplets with $\eta = 100$, in channels ranging from width, $w = [2, 5]R_0$ indicated by the colour bar. The crosses in black indicate the speed of an unconfined droplet with the same parameters.

As the channel increases in width, there is a larger gap between the droplet and the channel wall. This means there is more room for retrograde flow and so the droplet expends less energy pushing fluid in front of it, so is able to move faster. We note that droplets in channels $w = \{2.5, 3.0\}R_0$ for $|\zeta\Delta\mu| = 5$ break the trend and have lower speed. This is possibly due to their relative y-diameter compared to the channel size (see figure 3.7) , reducing space for retrograde flow and requiring the droplet to push more fluid, as they elongate perpendicular to the channel.

In 2.3.3 of the previous chapter, we saw that $|v| \propto \frac{|N_{xyy}|}{\eta^{(int)}+\eta^{(ext)}}$ for droplets with equal viscosity internally and externally. We plot this relationship again, for droplets in channels in figure 3.5. We see here that the linear correlation no longer holds, with the deviation from the unconfined case increasing with increased levels of confinement. This deviation is related to the reduced velocity due to pushing fluid when confined. Similarly, there is now also no longer a linear relationship between β and $\frac{-S_{xx}}{|N_{xyy}|}$.

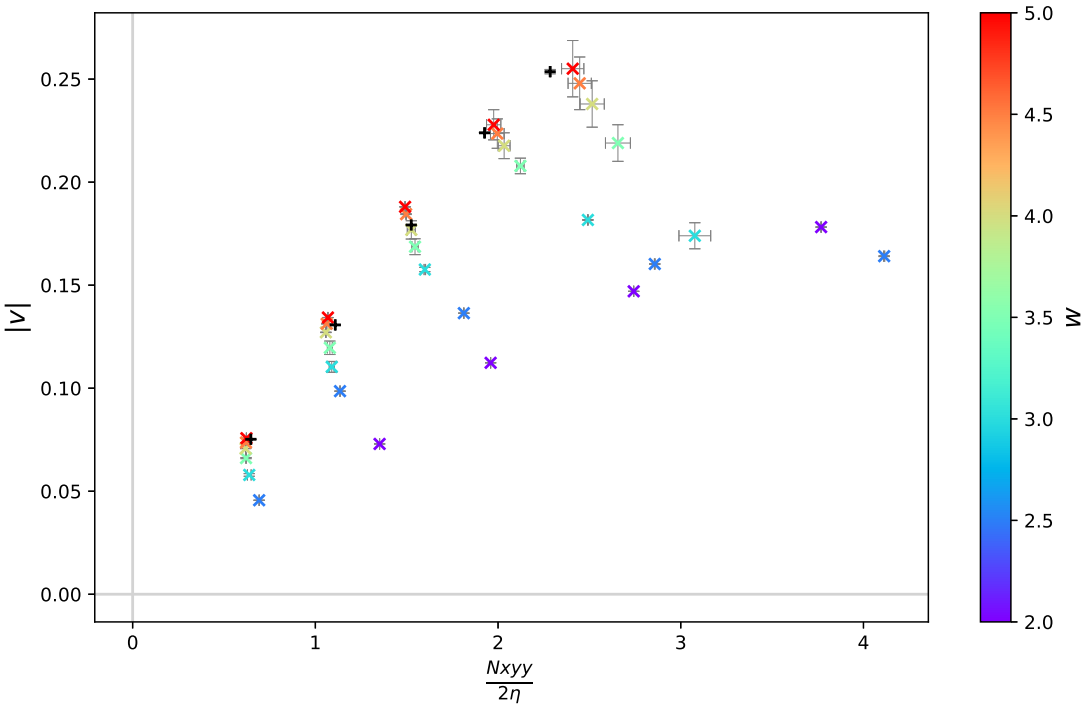

FIGURE 3.5: Speed of droplets with $\eta = 100$, in channels ranging from width, $w = [2, 5]R_0$ indicated by the colour bar. Plotted against $\frac{|N_{xyy}|}{2\eta}$, the part of the quadrupole moment associated with the source dipole. The crosses in black indicate the speed of an unconfined droplet with the same parameters.

3.1.2.2 Droplet shape

For the unconfined case we see all the droplets in our parameter range have a shape very close to a circle (see the black crosses in figure 3.6). We plot the aspect ratio of the droplets in channels against their activities in figure 3.6. The aspect ratio is calculated by fitting an ellipse to the droplet and taking the ratio of the radii, where a is the x-radius and b is the y-radius.

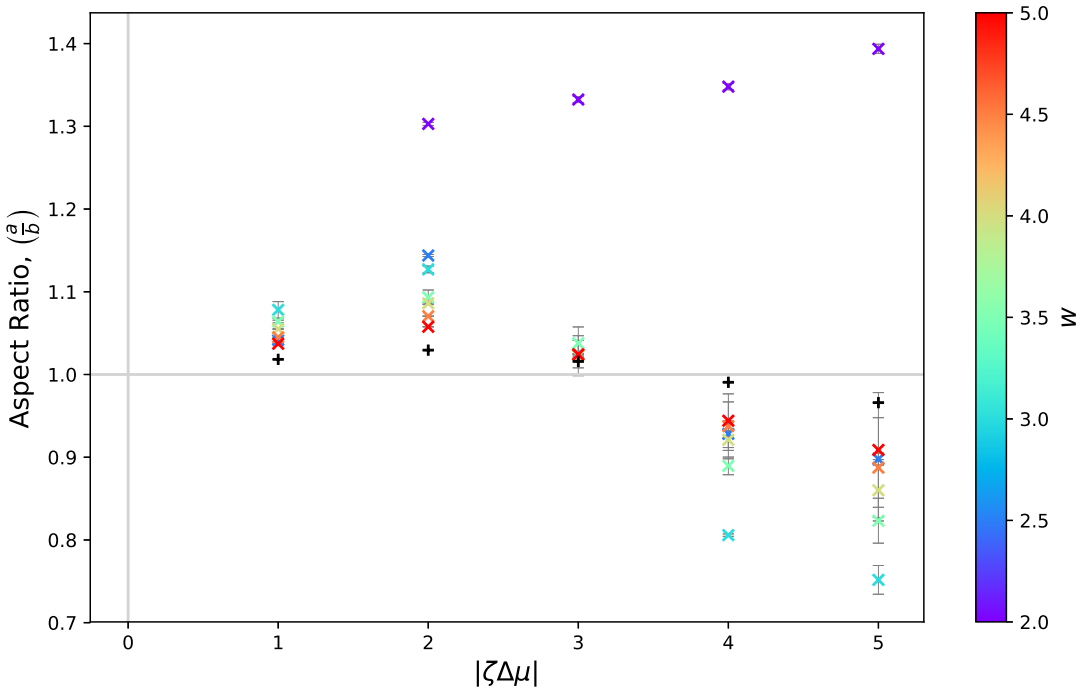

FIGURE 3.6: Aspect ratio of droplets with $\eta = 100$, varying in activity, in channels ranging from width, $w = [2, 5]R_0$, The crosses in black indicate the aspect ratio of an unconfined droplet with the same parameters. The grey line indicates the aspect ratio of a circle, where $a = b$.

In the narrowest channel, $w = 2R_0$, where the width is equal to the diameter of the undeformed droplet we see a fairly dramatic lengthening of the droplet, this is due to the additional induced flow along the channel. As there is no room for retrograde flow past the droplet, the droplet pushes the fluid in front of it, setting up a flow along the periodic channel. Any potential deformation perpendicular to the direction of motion is suppressed by the channel geometry. So, due to the area constraint on the droplet, implemented to model volume conservation in cells, any deformation, for example the change in curvature of the active region, must lead to a lengthening of the droplet along the channel.

As the channel gets wider, and the effect of the droplet pushing fluid is reduced, we see the droplet reducing in length. The droplet shape tends towards the unconfined shape as the channel width increases. As we saw in section 2.3.4 for droplets where the quadrupole was dominant over the stresslet, we see droplets with a negative stresslet (positive β/ puller) elongating along the direction of motion, and droplets with a positive stresslet (negative β/ pusher) elongating perpendicular to the axis of motion, where permitted by geometric constraints. In figure 3.7 we show examples of the droplet shape taken when the droplet is in the centre of the channel and rotated to be aligned along the axis for comparison. We exclude the droplet with $|\zeta\Delta\mu| = 1.0$ in the width $2R_0$ channel as it is non-motile.

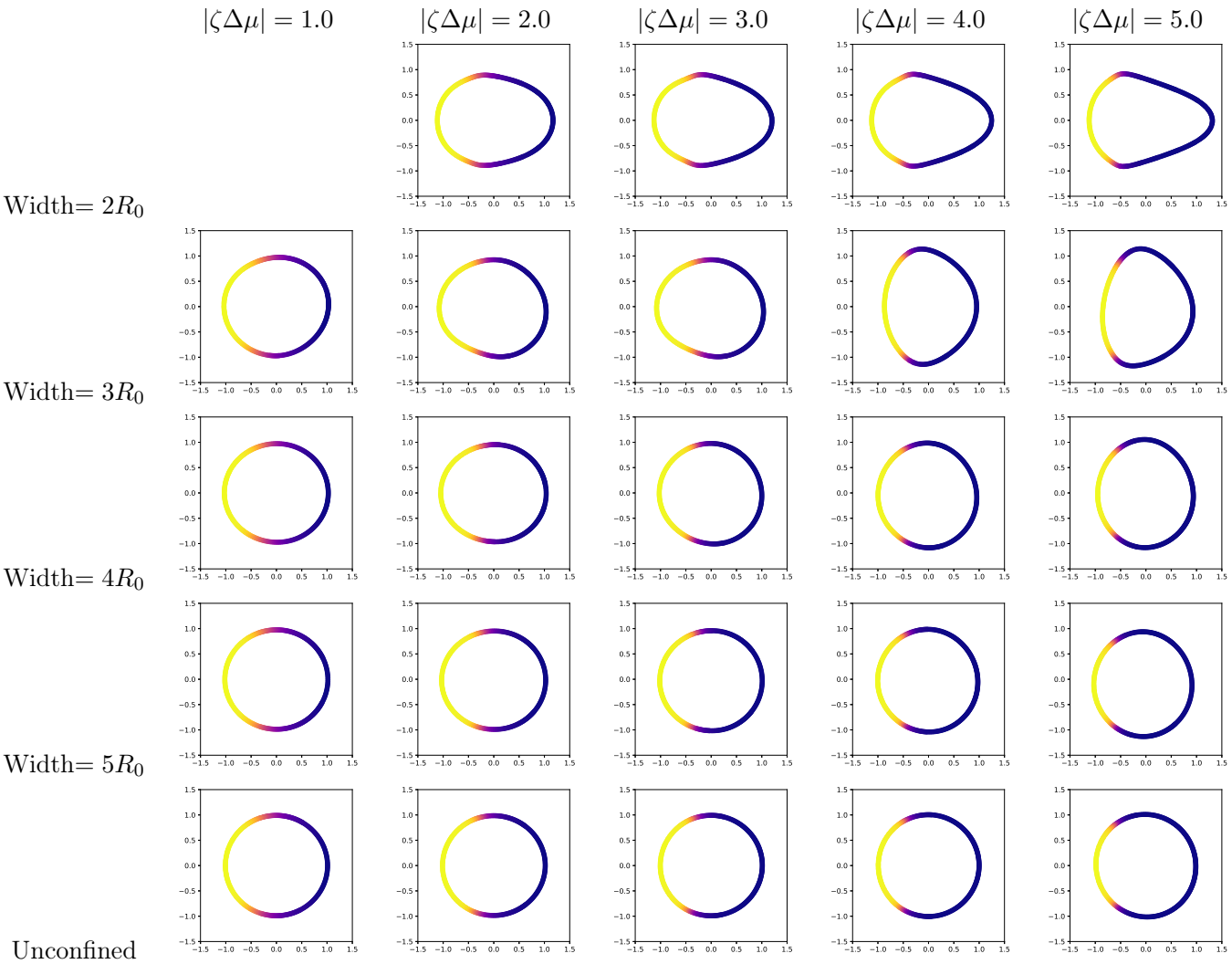

FIGURE 3.7: Typical droplet shape when situated in the centre of channels width= $\{2, 3, 4, 5\}R_0$ and for unconfined droplets. Droplets are re-orientated along the x-axis for comparison. the droplet with $|\zeta\Delta\mu| = 1.0$ in the width= $2R_0$ channel was non-motile, so has not been included here.

We can also look at how the channel width affects the curvature of the active region, κ. We define the active region as the part of the droplet which has high concentration of active particles, measured between the maximum and minimum gradient in concentration. We measure the curvature of this region by fitting a circle to it using a least-squares fitting method. We see in figure 3.8 that for channels with $w > 2R_0$, when the stresslet, S_{xx} is negative, as shown in figure 3.3 the active region has higher curvature and if it is positive the active region has decreased curvature, compared to a circle, flattening out the back. This fits with observations made in chapter 2.

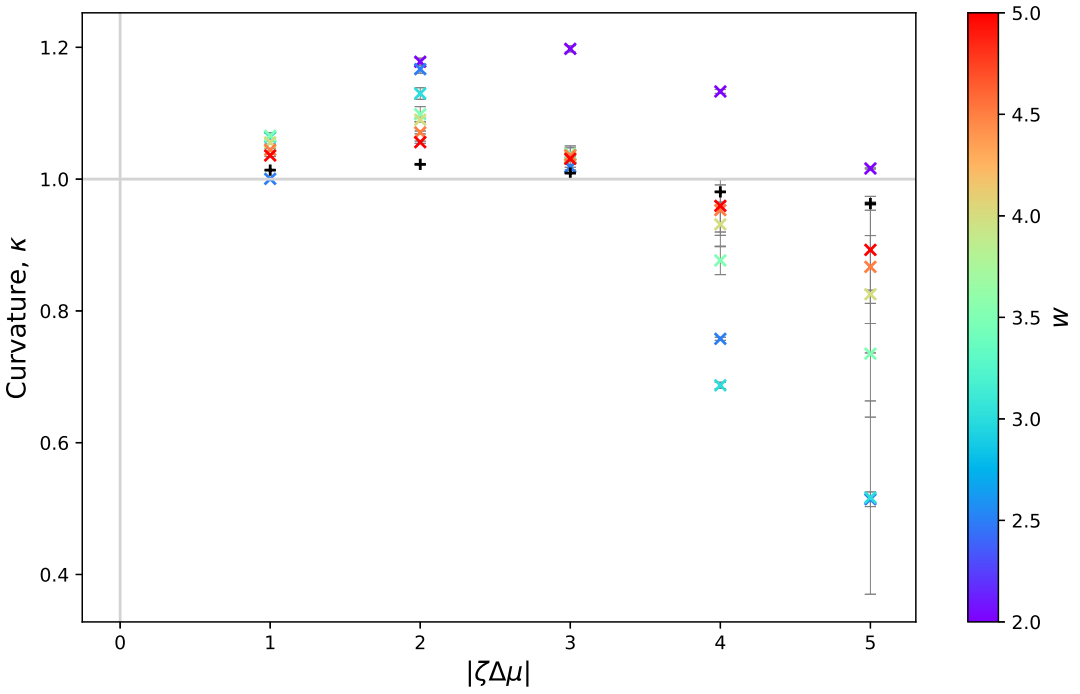

FIGURE 3.8: Curvature of the active region of droplets with $\eta = 100$, in channels ranging from width, $w = [2, 5]R_0$, The crosses in black indicate the curvature of an unconfined droplet with the same parameters. The grey horizontal line, represents the curvature of an unreformed droplet, which is a circle of radius 1.

As the droplet here is confined in a channel, it sets up a gradient in pressure along the channel as it moves. The increased pressure difference across the boundary due to the induced pressure gradient in the channel affects the curvature of the active region. The shape of the droplet is determined by the normal force balance at the boundary:

$$\vec{n} \cdot \left(\Delta \left(2\eta \underline{\underline{u}} - P\underline{\underline{I}}\right)\right) \cdot \vec{n} = \frac{\gamma}{R} \tag{3.8}$$

Where $\vec{n}$ is the outward normal to the interface, $\underline{\underline{u}}$ is the strain rate tensor, $\underline{\underline{I}}$ is the identity matrix, P is the pressure, γ is the tension of the interface and R is the radius of curvature of the interface. Δ denotes the difference between the internal and external values. The additional terms to the Young-Laplace equation arise due to our droplet moving. While the velocities are equal at the interface, the gradients in velocity are not necessarily equal, resulting in a difference in the stain rate tensor. The pressure gradient and induced flow in the channel enhances the normal constraint on the left hand side of equation 3.8.

When the normal constraint on the droplet boundary is dominant over the tension then $\kappa > 1, R < R_0$ and if the tension is dominant then $\kappa < 1, R > R_0$. As the activity increases then by design the tension of the active region increases.

It follows then, that due to the constant area constraint, that if the active region has flattened then, in the absence of other effects like extreme confinement, the rest of the droplet will elongate perpendicular to the axis of motion and vice versa for high curvature active regions, acting to minimise the length of the boundary.

3.1.2.3 Droplet trajectory

While the unconfined droplets will travel in a straight line, as will the droplets in a channel with width 2, droplets in channels greater than their diameter can oscillate in the channel.

From the literature we know that the presence of walls can cause squirmers to turn towards (pushers) or away (pullers) from them depending on the squirmer type [65]. The force dipole for a pusher will act to orientate the swimmer parallel to the wall and for a puller it will orientate it perpendicularly to the wall[65]. So the force dipole acts to either repel or attract the droplet to the wall. The force quadrupole induces a rotation away from the nearest wall [98]. For microswimmers in channels oscillatory behaviour has been observed [99]. This behaviour can be explained by the interaction of the flow field with the walls. In the literature, for simulations of squirmer in channels it has been seen that weak pullers will swim along the channel centre, while weak pushers will oscillate from wall to wall in the channel [66], [98]. For strong pushers and pullers the droplet will turn to the wall and end up sliding along it.

Much of the literature focuses on the dipole field as it decays the slowest, and such is likely to dominate interaction with channel walls, especially in wider channels. However, we established in our previous chapter that the quadrupole plays a significant role in our model and such we need to consider these effects here.

We also note that in most studies of interaction of squirmers with walls or channels, the squirmers have fixed shapes and a prescribed squirmer parameter, β. As both the shape and squirmer parameter of our droplet are emergent, based on both droplet parameters and environmental parameters, our analysis is not quite so clear cut. We know from the previous chapter that whether our droplet behaves as a pusher or a puller is a function of activity and viscosity. But we also see that just changing the width or length of a channel can change the value of the stresslet, (figures 3.3, 3.12).

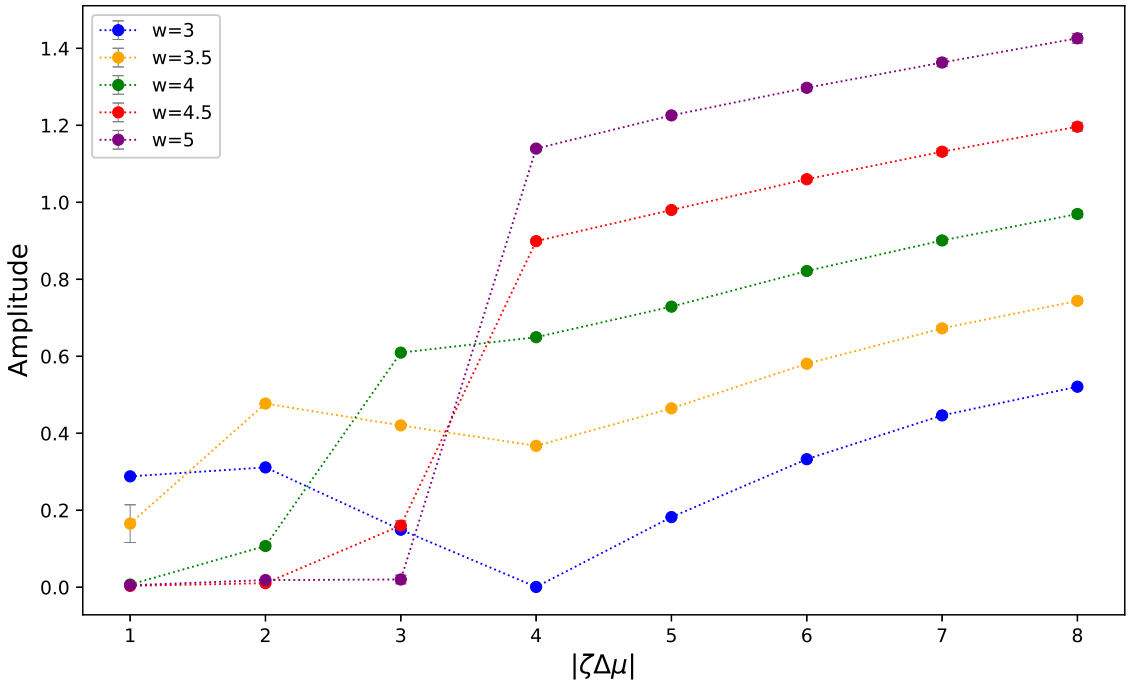

FIGURE 3.9: Steady state amplitudes, in units of R_0 for droplets in channels widths $[3, 5]R_0$. Here we have joined the points with a dotted line to guide the eye.

We measure the amplitude as the maximum distance of y coordinate for the droplet centre of mass from the channel centre line. In figure 3.9 we see that for the channel with width 5, the droplets behave as expected from the literature, with droplets with a negative stresslet S_{xx} swimming along the centre line and droplets with positive S_{xx} oscillating in the channel, The droplet stresslets are shown in figure 3.3. The channel with width $3R_0$ has oscillations for positive and negative S_{xx} and the oscillation amplitude does not increase monotonically with activity. In general the range of activities for which we see non-oscillating droplets reduces as the channel gets narrower, where the channel with width $3.5R_0$ has no droplets which swim along the centre line.

In narrower channels the pressure-gradient and background flow due to the presence of the moving droplet in the channel is greater than in wider channels. We can think of the system as a superposition of a confined passive droplet translating in a Poiseuille flow and of an active droplet in a non-periodic channel. Intuitively we can see how this may have an effect on the droplets. Most of the droplets which end up swimming along the centre line of the channel initially have small oscillations which decay. If a droplet is off-centre in a channel with a parabolic background flow, as is the case for no-slip boundary conditions, then the top and bottom of the droplet will move at different rates. This will act to turn the droplet. This could either damp or amplify oscillation, depending on the swimmer type (e.g. pusher vs. puller). Above some activity, the stresslet (and higher order moments) induced by the presence of a wall near a passive droplet in a flow, will be negligible compared to the stresslet induced by the interaction of the local droplet generated flow with the wall. At this point the droplet will behave as if it is in a non-periodic channel where there is no self-induced flow. As the channel gets wider the effect of the self-generated flow decreases, so the required activity to overwhelm this effect becomes lower.

For the case where we vary the channel length, we increased the width to $3R_0$. We chose $|\zeta\Delta\mu| = 4$ as for the channel of length $12R_0$, this did not oscillate. Increasing the length of the channel caused the droplet to begin oscillating.

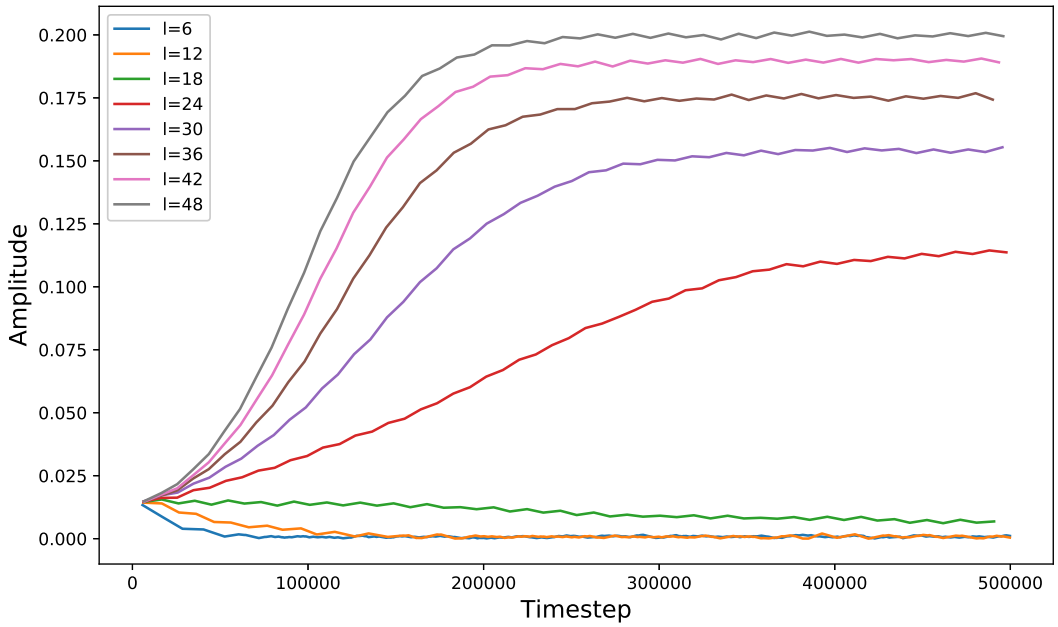

FIGURE 3.10: Amplitude, in units of R_0, of oscillations for droplets with $\eta = 100, |\zeta\Delta\mu| = 4$ in channels with width $3R_0$and varying length,l.

In figure 3.10 we see that for lengths 18 and below and oscillations are damped and the droplet swims along the centre of the channel. For longer channels the oscillations grow until they reach a steady amplitude, with amplitude increasing as the channel length increases. We know from section 3.1.1 that droplet speed, and thus the magnitude of the induced flow, decreases exponentially with channel length. In figure 3.11 we plot the steady state amplitudes as a function of length. We see that the amplitudes, A, can be fit using an exponential plateau function, where the plateau is dependent on the channel width and the droplet diameter:

$$A = \alpha\left(\frac{w}{2} - b\right)\left(1 - e^{-\frac{(l-l_o)}{10}}\right) \tag{3.9}$$

Here b is the y radius of the droplet, in line with our definition of aspect ratio. l_o is a factor to shift the fit to where the oscilations begin, and here is 18. α is a fitting parameter, for this set of parameters it is 0.6. We chose 10 for the divisor in the exponential to match the function in (4.3) as we have assumed these effects are related. The implication of this graph is that the induced flow in the channel acts to damp oscillation, for this type of swimmer. As the magnitude of induced flow decreases exponentially with length, the oscillations increase in amplitude.

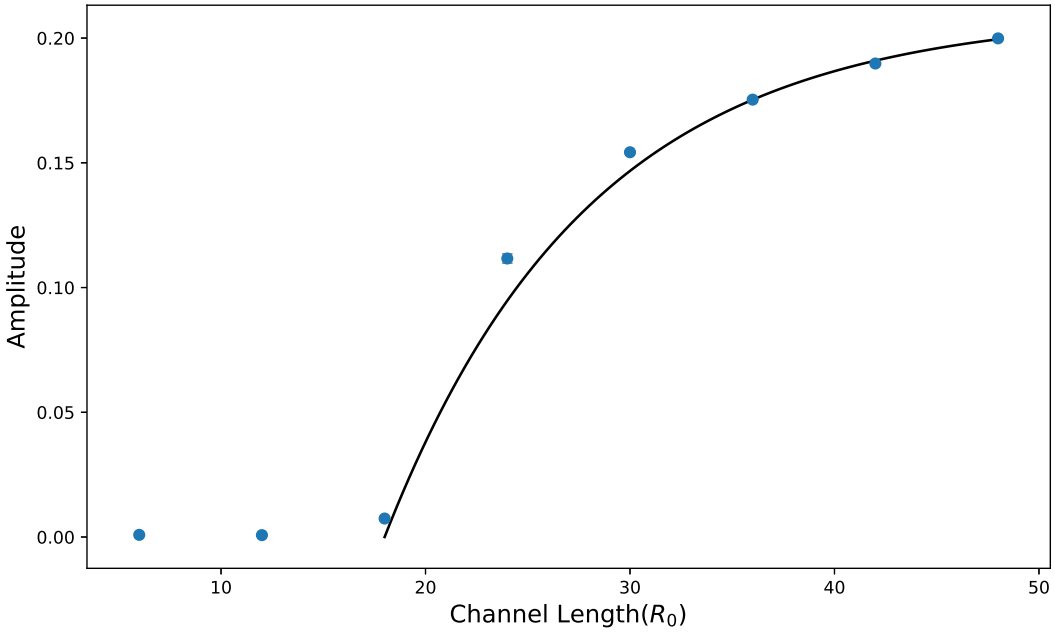

FIGURE 3.11: The amplitude of oscilations for droplets in different channel lengths. We fit the points using an exponential plateau function shown in equation 3.9. For these points the channel width= $3R_0$, the activity is -4, and η=100.

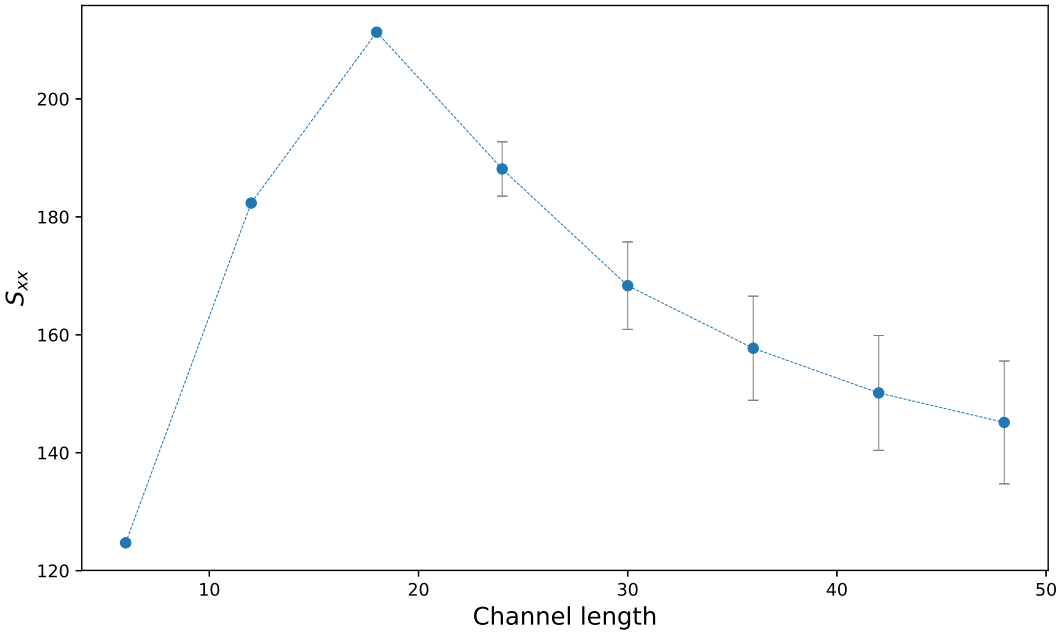

FIGURE 3.12: Stresslet, S_{xx}, for droplets with $\eta = 100, |\zeta\Delta\mu| = 4$ in channels with width $3R_0$ and varying length,l.

In figure 3.12 we see that the stresslet initially increases with channel length. Then, after the length where oscillations begin to occur, the stresslet decreases. We can

think of this turning point in S_{xx} as when the locally generated droplet forces become dominant over the forces acting on the droplet due to the induced flow in the channel.

3.1.2.3.1 Quantifying the Amplitude For droplets with positive stresslets, here $|\zeta\Delta\mu| > 3$, we see in figure 3.9 that the amplitude increases linearly with activity. We also see that the difference in amplitude between channel widths is regular, ~ 0.23, with small deviation for narrower channels due to greater droplet deformation away from a circle, and proportional to the channel width, which increases in intervals of 0.5. So the maximum amplitude is a linear function of $|\zeta\Delta\mu|$ and of channel width, for droplets with positive S_{xx}. It also increases with S_{xx}

For droplets with negative stresslets, here $|\zeta\Delta\mu| < 4$, the amplitude of oscillation does not take on an obvious pattern. We would expect, from previous theoretical work on droplets in channels [98], [66] that these droplets would swim along the centre line of the channel, however we see oscillations, as shown in figure 3.9 and discussed in 3.1.2.3.

3.1.2.3.2 Period of Oscillation The period of the oscillation changes based on channel width and on the droplet activity. For our channel where we vary the length but fix the width we see very little variation in wavelength. In figure 3.13 we plot the period of the droplets which oscillate in channels of different widths.

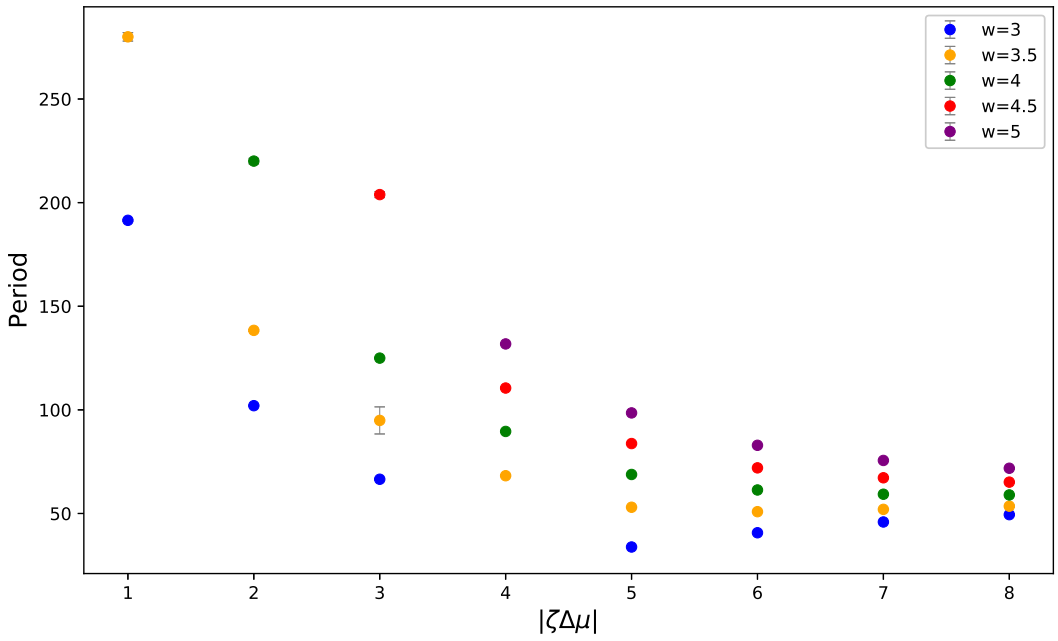

FIGURE 3.13: Plot of the period of oscillation for droplets which oscillate in channels of widths $[3, 5]R_0$, for varying activity, with $\eta = 100$.

We see that the period decays exponentially with activity. This is true regardless of the sign of S_{xx}. The droplets in narrower channels have a smaller period, than droplets in wider channels. Droplets in narrower channels have a shorter path to take before they must turn, resulting in a shorter time to complete an oscillation, and droplets with higher activity travel faster, also reducing the time to complete a period.

3.2 Summary

We have looked at the effects of confining a droplet by rigid walls on it's migratory behaviour. We placed droplets with both positive and negative stresslets in channels and varied both the length and the width of the channel.

We found in channels the width of the undeformed droplet diameter, that the velocity decays exponentially with channel length. This is due to the droplet having to push the fluid in front of it. We found that if we increased the width of the channel slightly to $3R_0$, then we saw the onset of oscillations which increased in amplitude as the channel increased in length.

For the channels which we varied in width, we saw that the centre of mass speed of the droplet decreased from the unconfined speed as the channels got narrower. We saw that confinement increases the deformation of the droplet. The narrower the channel the more deformed away from a circle the droplet was. The additional external pressure gradient, which increases as the channel gets narrower, increases the pressure jump across the boundary altering the ratio of tension and the normal constraint, and therefore the curvature.

For confined droplets in channels width $3R_0$ and above, we found that under certain circumstances droplets would oscillate in the channel, rather than swimming persistently as they did when they were unconfined. Droplets with a positive stresslet will oscillate in the channel. While droplets with a negative stresslet, which have a lower activity, experience greater effects from induced channel flow. In wider channels they will swim along the centre line. For narrower channels the induced flow from periodic confinement can induce rotation and thus oscillation in the channel.

3.A Form of Discrete Sine and Cosine Transforms.

The forms of the transforms used in section 3.1. Here there is a FFT in the x direction and either a discrete sine or cosine transform in the y direction. The form of the DST/DCTs are those listed in the FFTW (fastest fourier transform in the west) documentation [100].

Forward FFT, DST 1:

$$\hat{\rho}_{mn} = \sum_{k=0}^{Lx-1} \sum_{l=0}^{(Ly-1)-1} \rho_{kl}\, e^{\frac{2\pi imk}{Lx}} \sin\left(\frac{\pi(l+1)(n+1)}{(Ly-1)}\right) \tag{3.10}$$

Forward FFT, DST II:

$$\hat{\rho}_{mn} = \sum_{k=0}^{Lx-1} \sum_{l=0}^{(Ly-1)-1} \rho_{kl}\, e^{\frac{2\pi imk}{Lx}} \sin\left(\frac{\pi(l+\frac{1}{2})(n+1)}{(Ly-1)}\right) \tag{3.11}$$

Backward FFT, DST III:

$$\rho_{kl} = \frac{1}{Lx(Ly-1)} \sum_{m=0}^{Lx-1} \sum_{n=0}^{(Ly-1)-2} \hat{\rho}_{mn}\, e^{\frac{-2\pi imk}{Lx}} \sin\left(\frac{\pi(l+1)(n+\frac{1}{2})}{(Ly-1)}\right) \tag{3.12}$$

Forward FFT, DCT II:

$$\hat{\rho}_{mn} = \sum_{k=0}^{Lx-1} \sum_{l=0}^{(Ly-1)-1} \rho_{kl}\ e^{\frac{2\pi imk}{Lx}} \cos\left(\frac{\pi(l+\frac{1}{2})n}{(Ly-1)}\right) \tag{3.13}$$

Backward FFT, DCT III:

$$\rho_{kl} = \frac{1}{Lx(Ly-1)} \sum_{m=0}^{Lx-1} \sum_{n=0}^{(Ly-1)-1} \hat{\rho}_{mn}\ e^{\frac{-2\pi imk}{Lx}} \cos\left(\frac{\pi(l+\frac{1}{2})n}{(Ly-1)}\right) \tag{3.14}$$

Chapter 4

An active droplet confined by deformable walls

In the previous chapter we looked at the swimming behaviour of droplets in no-slip channels. Cell migration *in vivo* is highly variable depending on the external environment. Durotaxis, directional migration following a gradient in substrate stiffness, has been observed in the migration of crawling cells. The affect of the mechanical properties of a confining environment on 3D migration, has not yet been fully determined.

In this chapter we develop 2 models for deformable walls to confine a swimming droplet. We explore how changing the spring constant or elastic moduli alter the behaviour of the droplet.

4.1 Spring Lattice Walls

We construct walls from a triangular lattice of immersed boundary points. Initially we use an isotropic lattice of equilateral triangles with side length h. Each lattice point is connected with a Hookean spring which exerts a restoring force when deformed from its reference configuration. Since there is no pre-stress, this is the length of the spring, in this case h.The force exerted on a point, i by a spring is:

$$\vec{F}_{spring} = -\frac{1}{2}k(|\vec{X}_j^{Wall} - \vec{X}_i^{Wall}| - d_{ij})\frac{\vec{X}_j^{Wall} - \vec{X}_i^{Wall}}{|\vec{X}_j^{Wall} - \vec{X}_i^{Wall}|}, \tag{4.1}$$

where d_{ij} is the reference length of the spring connecting points i, j and k is the spring constant of the spring between points X_i and X_j .

We extend this model to non-uniform triangular lattices, generated using the 'DiscretizeRegion' function in Mathematica. Here d_{ij} no longer equals h. We chose parameters to give an average spring length of $\sim h$. As our springs are now different lengths in order to have a homoegeous stiffness through out the walls the spring constant is made dependant on the spring length. We use the following expression derived from the continuum model for linear elasticity [101]:

$$k_{ij} = \frac{8\mu_E}{3d_{ij}}\left(\frac{dA_i + dA_j}{2}\right) \tag{4.2}$$

where μ_E is the elastic shear modulus and dA_i is the area element associated with each point given by, $dA_i = \frac{1}{3}\sum_{T\in\mathcal{T}_i} A_T$ where $\mathcal{T}_i$ are the triangles containing point i.

The motivation for using a non-uniform mesh is that the mesh of equilateral triangles is restrictive in terms of wall geometry.For the equilateral case, the wall thickness must be a multiple of $\frac{\sqrt{3}}{2}h$ and any angles would need to be a multiple of $\frac{\pi}{3}$. A non-uniform mesh allows us to make structures in any shape. However, the assumptions involved in deriving equation (4.2) mean that it is only valid when the variance in the spring lengths from h are small. We must also note that using a spring lattice model we are restricted to looking at material with a Poisson ratio of $\frac{1}{3}$ [92].

4.1.1 Comparing equilateral and non-uniform latices

We check that using a non uniform mesh does not drastically alter the behaviour of the deformable walls, by running simulations with the same parameters and the same shape walls. With a thickness of $50\frac{\sqrt{3}}{2}h$ either side of the channel and length $12R_0$. We chose a spring constant, $k = 10000$ in simulation units,for the case of equal springs, and weight the non-uniform case equivalently.

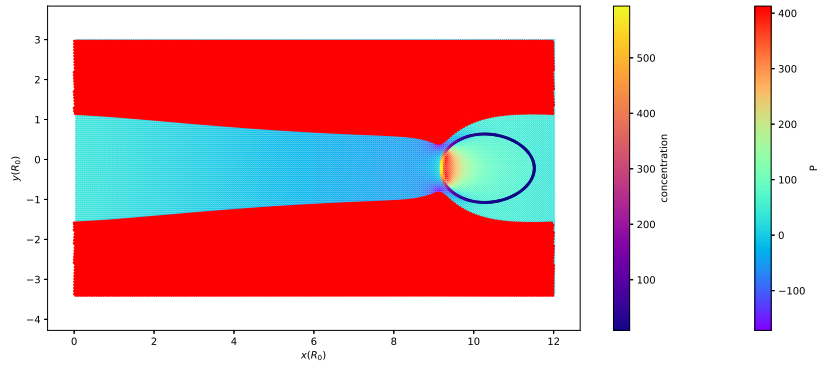

(A) Equilateral mesh

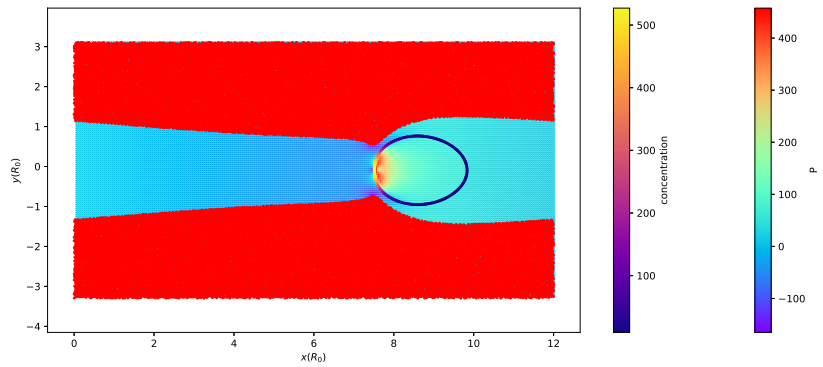

(B) Non uniform mesh

FIGURE 4.1: Droplet with $|\zeta\Delta\mu| = 10$, $\eta = 1000$, $k = 10000$. The walls are constructed from immersed boundary points in an equilateral triangle configeration in 4.1a and a non uniform configuration in 4.1b. Snapshots are taken from the final timestep in the simulation.

Figure 4.1 shows snapshots from the final point of the simulation for both spring lattice types. Due to some variation, the droplets are not at exactly the same coordinates, but we can see they have similar concentration profiles and deform the walls in a similar fashion. In order to more quantitatively judge the similarity of the simulations we plot the centre of mass speed, $|v|$, for both simulations in figure 4.2 and the minimum and maximum channel width in figure 4.3.

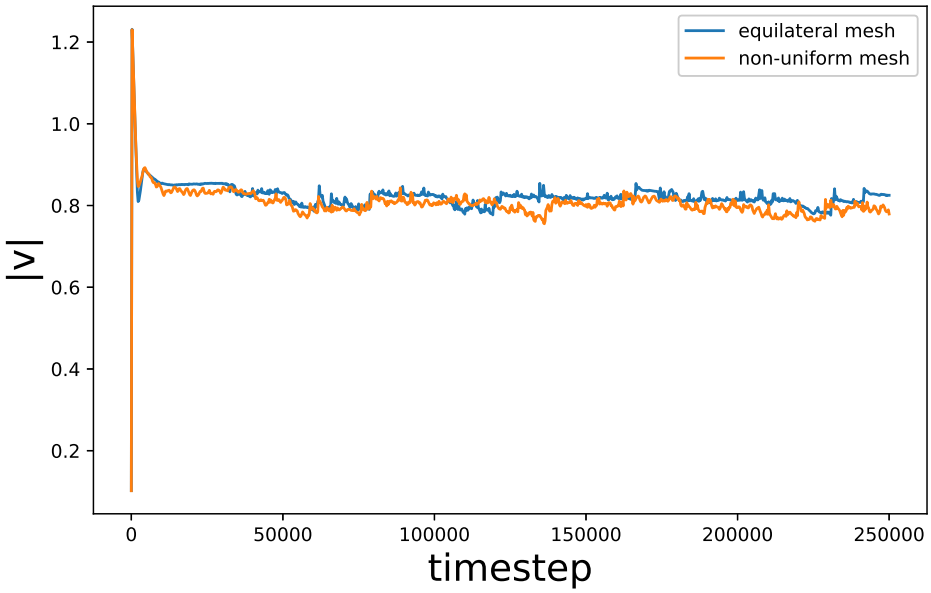

FIGURE 4.2: Centre of mass speed for active droplets in channels with equilateral triangle mesh or non-uniform triangle mesh.

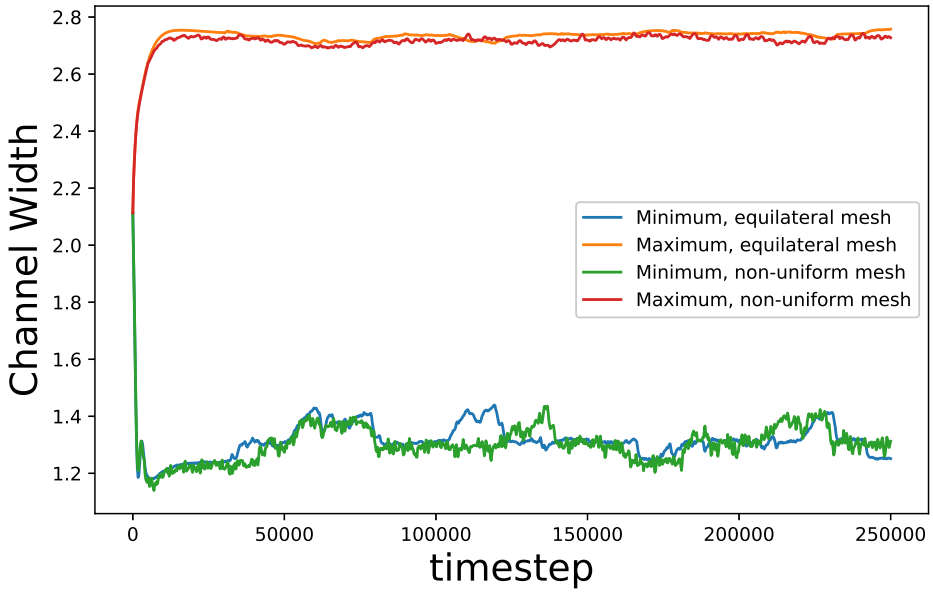

FIGURE 4.3: Minimum and maximum channel width for channels with equilateral triangle mesh or non-uniform triangle mesh., deformed by an active droplet.

We see in figures 4.2, 4.3, that while not an identical match the velocity and channel width take on the same form in both simulations with very little difference in value. We judge this to be acceptable to use to study droplet behaviour in deformable channels.

4.1.2 Varying the wall stiffness

In the previous chapter, we looked at the dynamics of active droplets in channels of length 12 and widths from 2 to 5. We take these same dimensions in order to compare our results. We look at channels length, $l = 12$, width, $w = \{2, 3, 4, 5\}$ and $\zeta\Delta\mu = \{-1, -2, -3, -4, -5\}$. All viscosity's here are 100. All values stated here are in simulation units. We choose a wall thickness of $1.5R_0$ on either side. This is a balance of needing thick enough walls to prevent underlying artefacts and needing the simulations to run in a reasonable time. The effect of wall thickness has less of an effect the stiffer the walls are, as there is less deformation for these cases.

We quote the spring constant k as the value for if all springs were the same length - as we are using a non-uniform mesh the springs are weighted based on the method expressed at the beginning of this section. We choose values of $k = [1, 10] \times 10^4$.

4.1.2.1 Droplet Velocity

4.1.2.1.1 Width $2R_0$ channel In a channel $w = 2R_0$ for rigid walls we found that there were no oscillations and the velocity increased with activity. For $\zeta\Delta\mu = -1.0$ the droplet did not reach a persistent swimming state and ended up stationary in the channel. In a deformable channel for $k = 10^4$ the droplet with $\zeta\Delta\mu = -1.0$ now swims persistently along the channel, and for $k = \{2 \times 10^4, 3 \times 10^4, 4 \times 10^4, \}$ we see some meandering behaviour where the droplet bounces from wall to wall, very slowly, but doesn't move persistently along the channel. For activities $|\zeta\Delta\mu| > 1.0$ all the droplets

swim persistently with a steady speed along the channel. In figure 4.4 we see that the droplet centre of mass speed, $|v|$, increases as k decreases. In line with what we saw in chapter 3 the main determinant of the droplet speed, in a channel, is the activity of the droplet, however we can see here that within each activity the droplet speed decays exponentially as k increases.

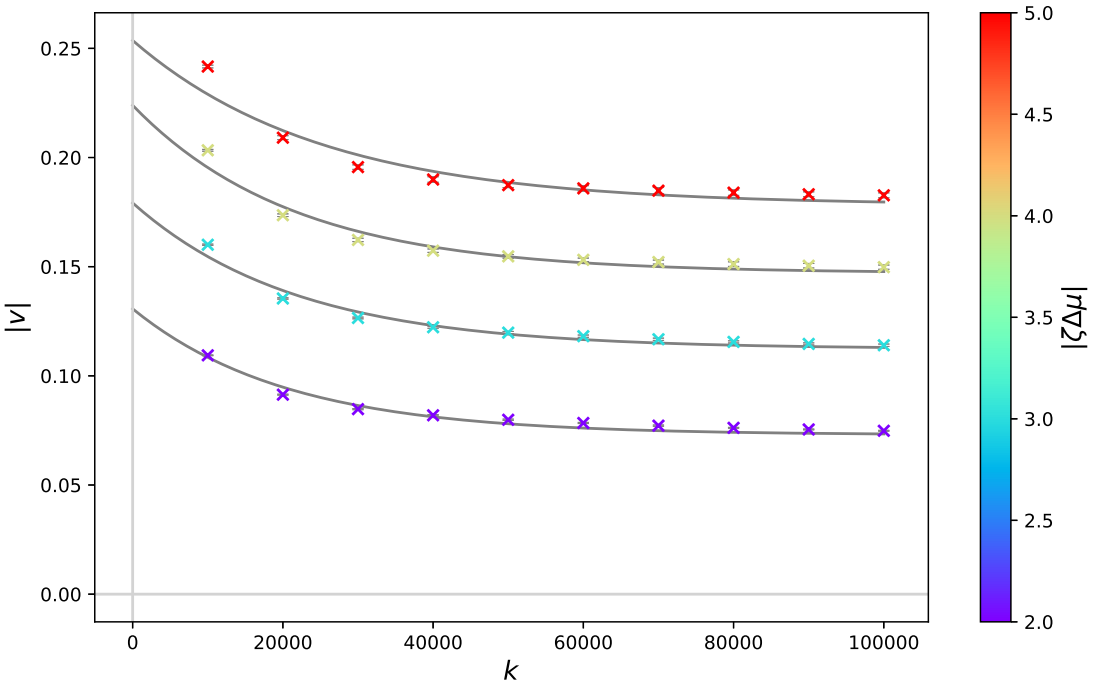

FIGURE 4.4: Centre of mass speed, $|v|$ of droplets in channels of varying stiffness, k, with width $2R_0$. The colour bar signifies the activity of the droplet, and the grey lines are fits using equation (4.3).

$$|v| = (|v|_{\text{unconfined}} - |v|_{\text{rigid}})e^{-\frac{k}{b}} + |v|_{\text{rigid}} \tag{4.3}$$

We fit equation (4.3) to our data, such that we will recover the rigid channel droplet speed, as found in section 3.1.2.1, for infinitely large k. We would get the unconfined droplet velocity for infinitely small k. This provides a reasonable fit, considering the complex nature of our system, and the fitted value of b increases with activity. Physically, we postulate $\frac{k}{b}$ is to do with the relative deformation of the droplet and the walls.

4.1.2.1.2 Channels with width $> 2R_0$ The quadrupole force moment, which contains a source dipole related part which correlated with the cell velocity, as shown in figure 2.11 in the last chapter, decays rapidly as $\frac{1}{r^3}$. The dipole force moment decays more slowly as $\frac{1}{r^2}$ [65]. So as the channels get wider the forces generated by the droplet are much smaller at the wall. We see in figure 4.5 that, for channels width $3R_0$ it's only the highest activity droplets, or the softest walls, where there is a difference in the velocity. This corresponds to simulations where the wall can be deformed by

the droplet. For channels with widths $4R_0$ and $5R_0$, the velocity profile is practially idendical for both channel widths, as such we plot only the graph for width $5R_0$ in figure 4.6. The only velocity difference we see here is for the highest activity droplet, $|\zeta\Delta\mu| = 5$.

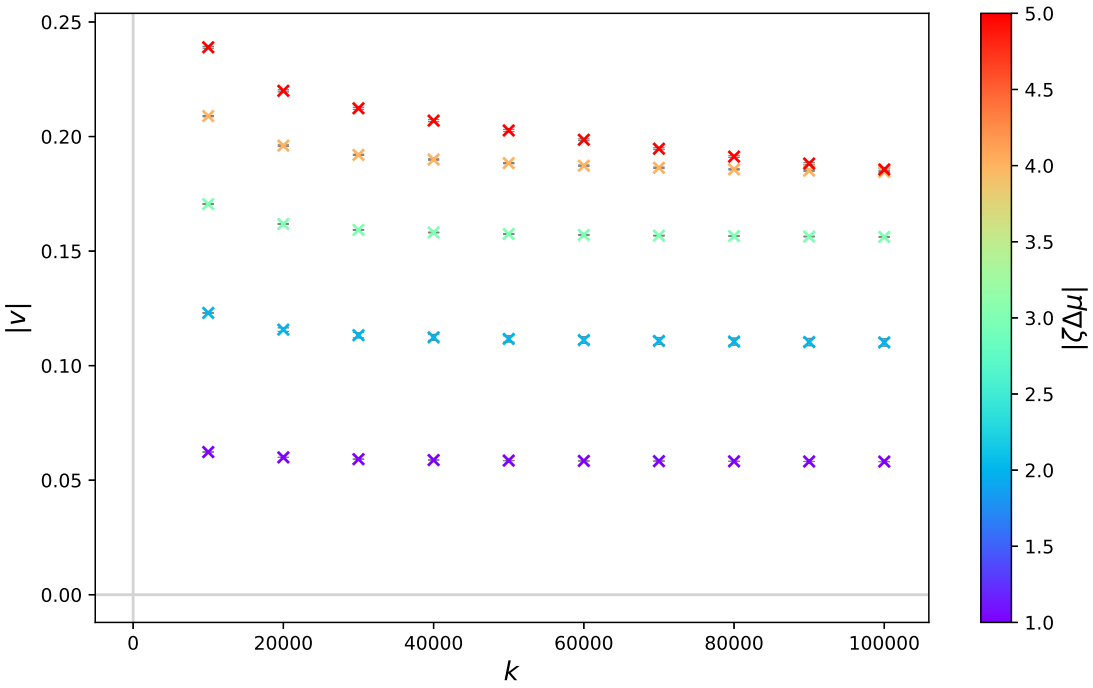

FIGURE 4.5: Centre of mass speed, $|v|$ of droplets in channels of varying stiffness, k, with width $3R_0$. The colour bar signifies the activity of the droplet.

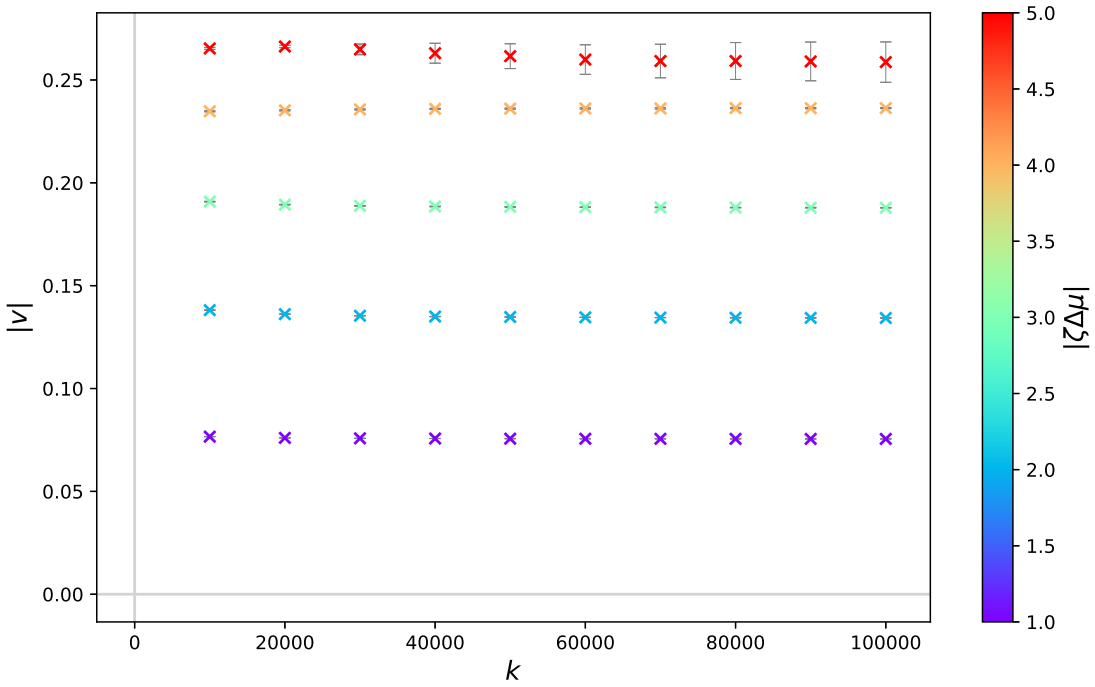

FIGURE 4.6: Centre of mass speed, $|v|$ of droplets in channels of varying stiffness, k, with width $5R_0$. The colour bar signifies the activity of the droplet.

4.1.2.2 Deformation of droplet and wall

4.1.2.2.1 Width $2R_0$ channel We look at $|\zeta\Delta\mu| > 1.0$ as these move persistently for all channel stiffness.

While all droplets for this channel width are elongated along the channel for all levels of stiffness, we find that how stretched out they are is a function of k. In figure 4.7 we plot the aspect ratio and we see that it increases with k, so the droplets in the stiffest channels have greatest aspect ratio, and the droplets in the softest channels are closer to a sphere.

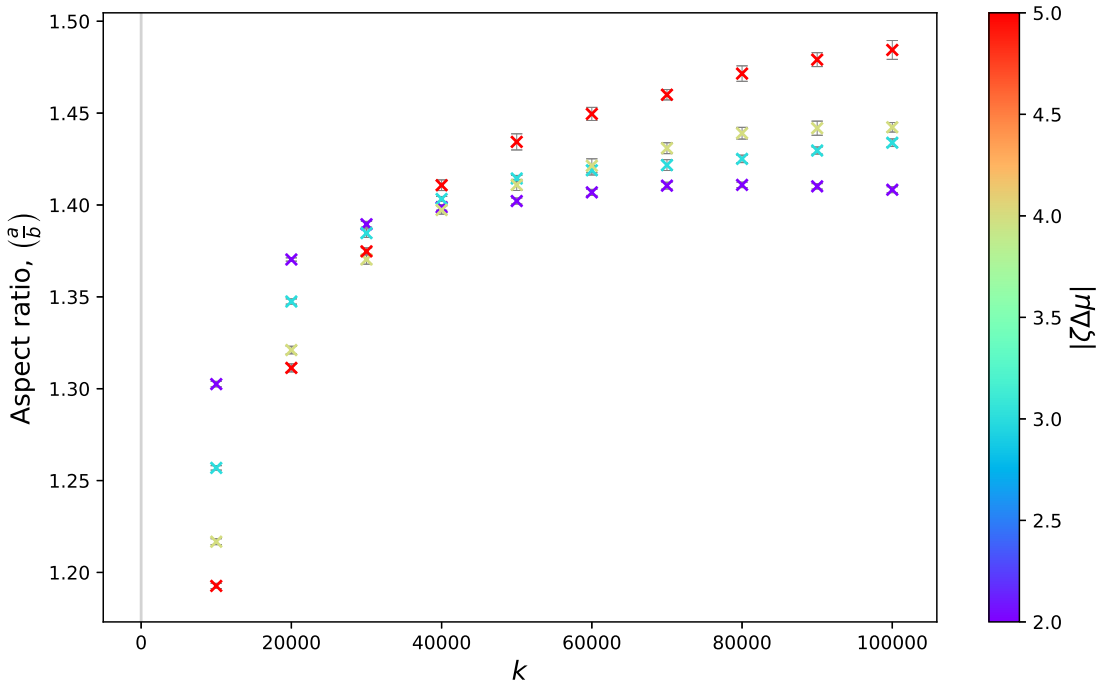

FIGURE 4.7: Aspect ratio, $\frac{a}{b}$ of droplets in channels of varying stiffness, k, with width $2R_0$. The colour bar signifies the activity of the droplet.

We also see a difference in the curvature of the active region, as we see in figure 4.8. Droplets in the most deformable channel have the lowest curvature, although it is still greater than that of a unit circle. The curvature initially steeply increases before decreasing again at a slower rate.

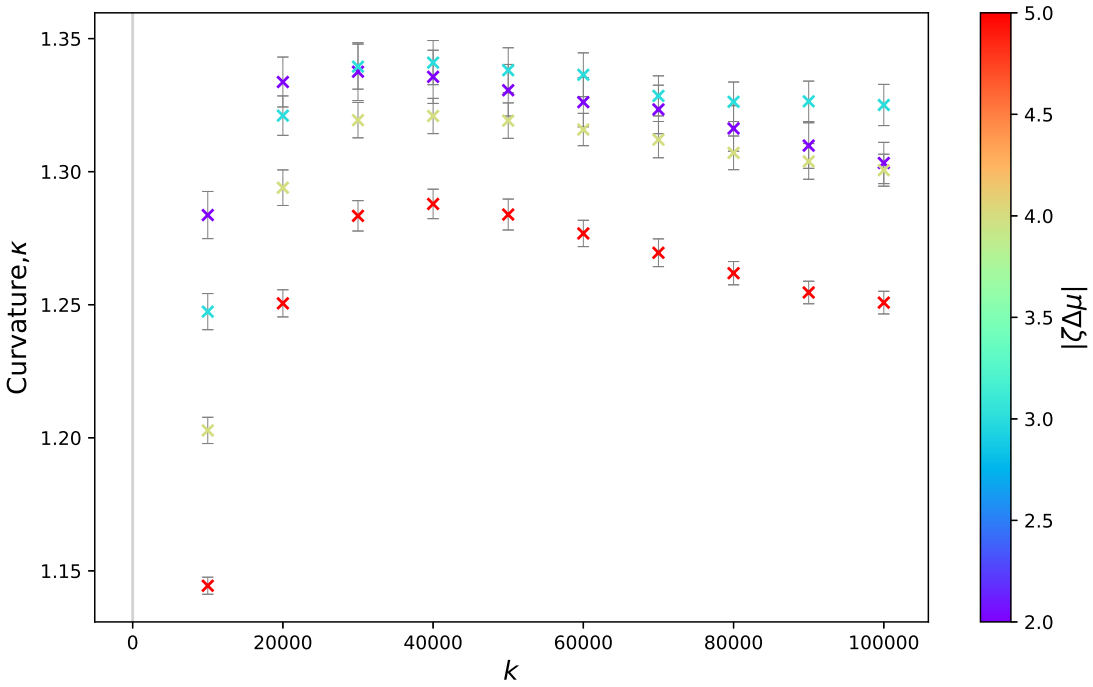

FIGURE 4.8: Curvature, κ of droplets in channels of varying stiffness, k,with width $2R_0$. The colour bar signifies the activity of the droplet.

We note that there is a maximum in the curvature, in figure 4.8, at approximately the spring constant where there is a crossover in activity dependence in aspect ratio in figure 4.7. For softer walls it is easier for the droplet generated forces to deform the walls, as the walls become stiffer we see that the aspect ratio of the droplet increases as these forces now deform the droplet instead.

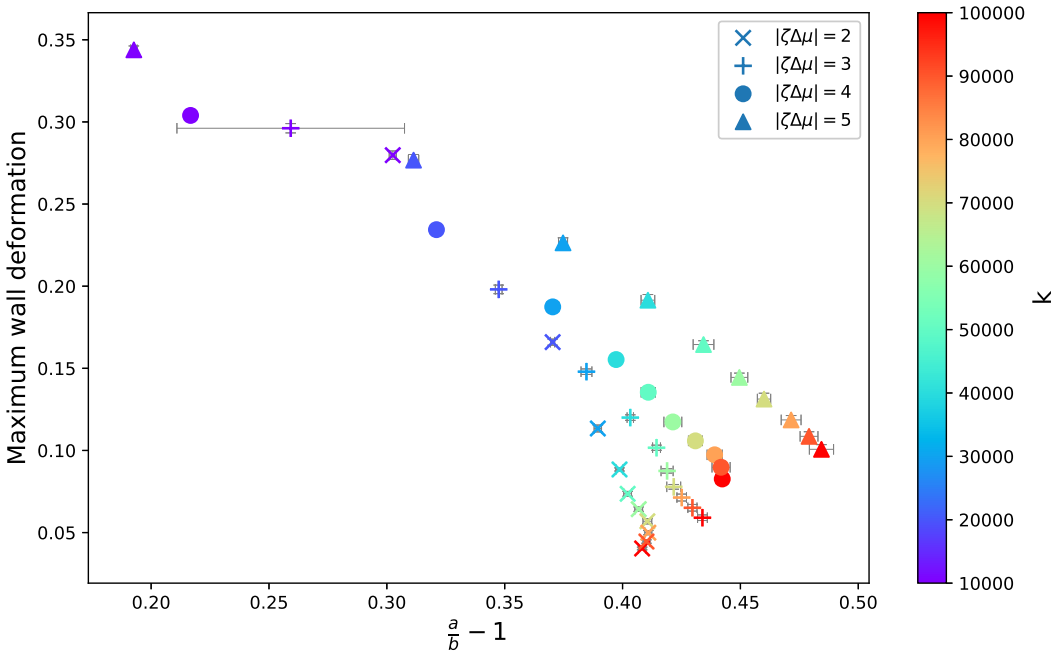

FIGURE 4.9: Maximum deformation of the wall away from the reference state against the difference between the aspect ratio $\frac{a}{b}$ and the aspect ratio of a circle: 1. The colour bar indicates the stiffness of the channel. This is for droplets with activities $\{2, 3, 4, 5\}$.

We plot the maximum wall deformation against $\frac{a}{b} - 1$,which is the difference between the aspect ratio of the droplet and the aspect ratio of a circle. In figure 4.9 we can see that, as expected, for lower droplet deformation there is higher wall deformation, and vice versa.

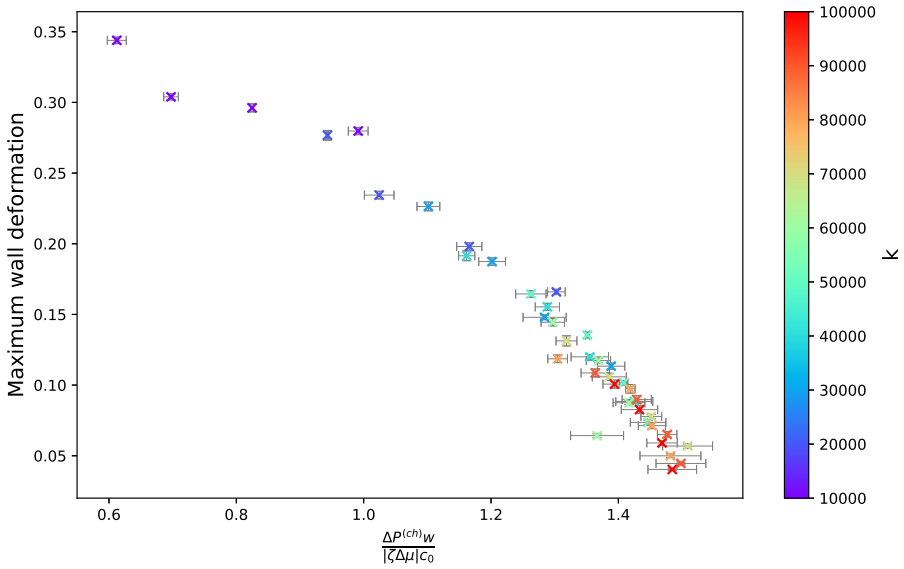

FIGURE 4.10: Maximum wall deformation against a dimensionless quantity which is a ratio of the Pressure gradient in the channel $\Delta P^{(ch)}$ times the channel width, w and $|\zeta \Delta \mu| c_0$. The colour bar shows the spring constant.

We finally relate the wall deformation to the pressure gradient in the width $2R_0$ channel. In figure 4.10 we have plotted the maximum deformation of the walls against a dimensionless quantity involving the pressure gradient along the channel scaled by the activity of the droplet. Here the initial concentration c_0 and w are constants. For large deformation this quantity is low, and for small deformation, it is high. Implying that the deformation of the walls decreases pressure build up in the channel.

4.1.2.2.2 Channels with width $> 2R_0$ Here we will look at channels width $3R_0$ and $5R_0$ as the wall and droplet deformation behaviour is very similar for channels with widths $4R_0$ and $5R_0$.

Due to the rapid decay of force moments, we see shape change of the droplet with respect to wall stiffness is minimal for activities less than 4, see figures 4.11, 4.12. These wider channels more clearly illustrate the relationship between the droplet and the wall stiffness, as the droplet is less strongly confined, so no shapes are suppressed. Also the effects of induced channel flow have less effect as the channel increases in width. Looking at activities$>$ 3in figures 4.11 and 4.14 We see that for softer walls the droplet is more circular and as wall stiffness increases the droplet aspect ratio drops below 1 as it elongates perpendicularly to its axis of motion. This implies that for soft walls most of the droplet generated forces go into deforming the walls, and the droplet shape is closer to the unconfined case. when the walls become stiffer they can no longer be deformed (as much) and the forces, instead deform the droplet. We note that were you to extrapolate the curves back to $k = 0$, due to the additional induced flow effect in the periodic channel the base shape for the droplet is slightly elongated along the channel, only slightly for width $5R_0$ (figure 4.12), but more obviously for the width $3R_0$ channel as seen in figure 4.11. we see this effect also in the curvature (figures 4.13, 4.14).

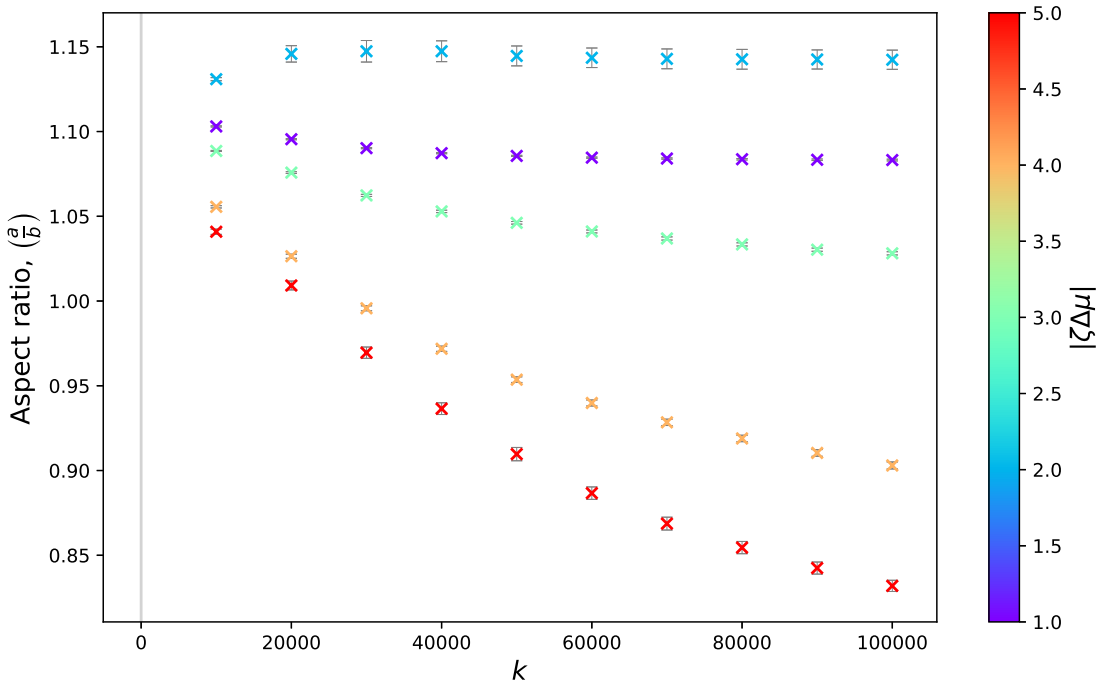

FIGURE 4.11: Aspect ratio, $\frac{a}{b}$ of droplets in channels of varying stiffness, k, with width $3R_0$. The colour bar signifies the activity of the droplet.

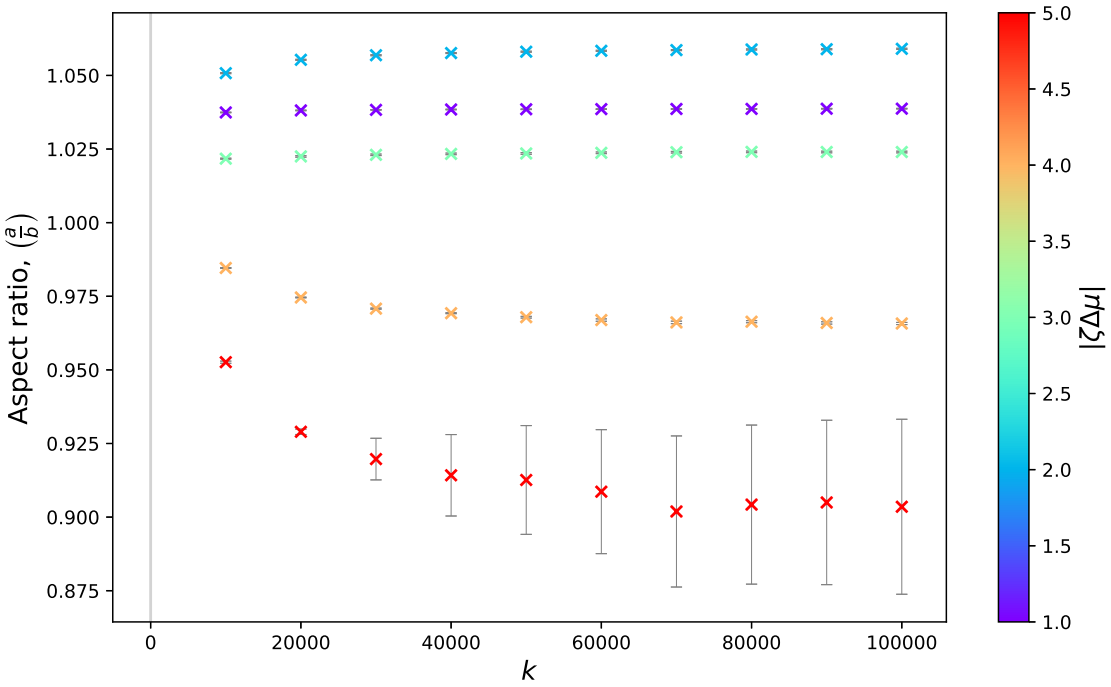

FIGURE 4.12: Aspect ratio, $\frac{a}{b}$ of droplets in channels of varying stiffness, k, with width $5R_0$. The colour bar signifies the activity of the droplet.

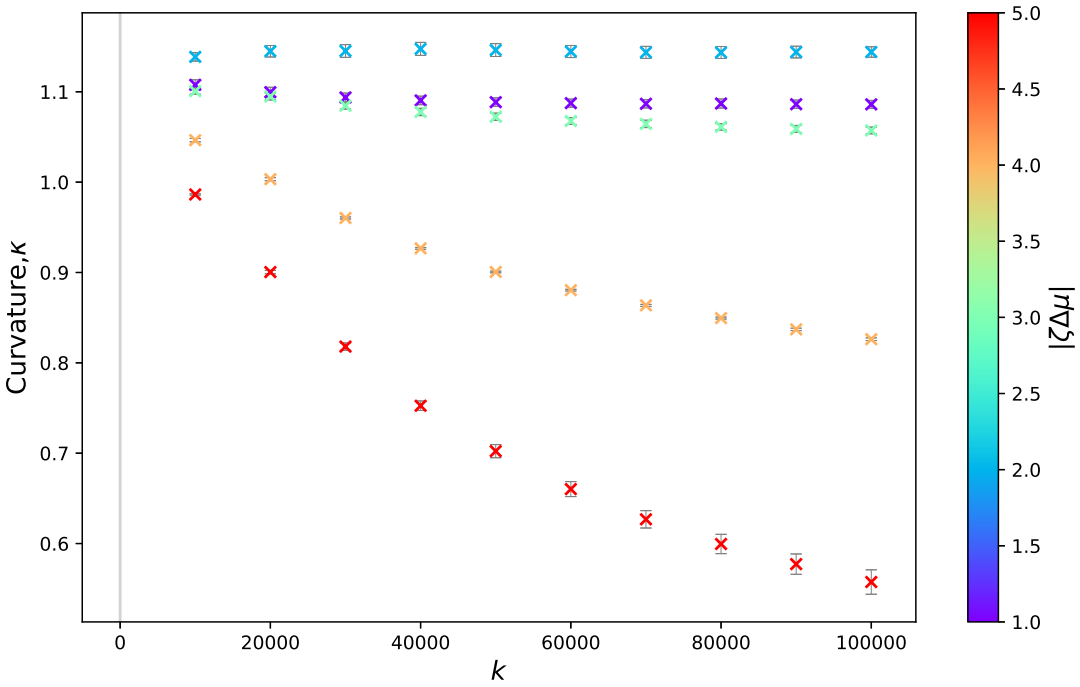

FIGURE 4.13: Curvature, κ of droplets in channels of varying stiffness, k,with width $3R_0$. The colour bar signifies the activity of the droplet.

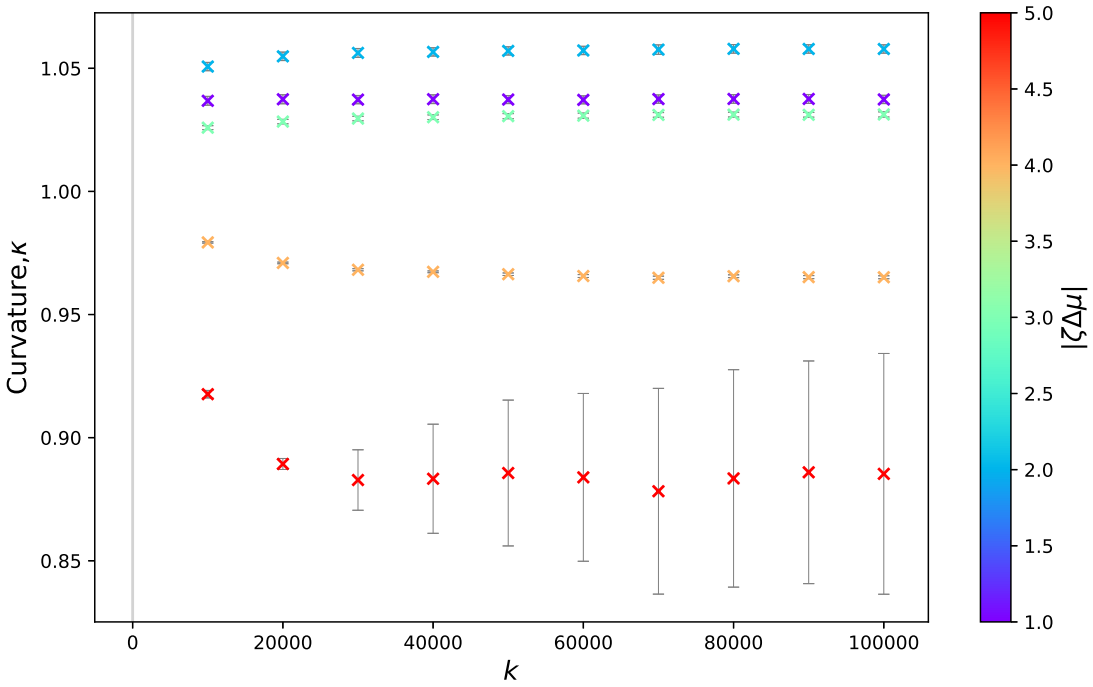

FIGURE 4.14: Curvature, κ of droplets in channels of varying stiffness, k,with width $5R_0$. The colour bar signifies the activity of the droplet.

Now that we are looking at wider channels the droplets are free to deform both along and perpendicularly to their axis of motion. We plot the maximum wall deformation against the droplet deformation away from the circle, $\frac{a}{b} - 1$, in figures 4.15 and 4.16, as we did in 4.1.2.2.1. As mentioned, droplets can now deform to have aspect ratios greater or less than one, so the gradients of the different curves don't all have the same sign of gradient. This is best demonstrated in figure 4.16, for the width $5R_0$ channel. Here we see that the relationship observed in figure 4.9 still holds, the higher the wall deformation the lower the droplet deformation away from a circle, and vice versa i.e. a positive gradient for $\left(\frac{a}{b} - 1\right) < 0$ and a negative gradient for $\left(\frac{a}{b} - 1\right) > 0$. For the channel with width $3R_0$ the case is slightly different as the flow induced by the droplet due to the periodic boundaries now is big enough to affect the droplet shape, elongating it along the droplet axis of motion. In figure 4.15 we estimate the deformation caused by the periodic induced flow, by looking at figure 4.11 and estimating the extrapolated aspect ratio at $k = 0$. In the context of this line, we see that the deformation away from this base aspect ratio is inversely proportional to deformation of the channel walls.

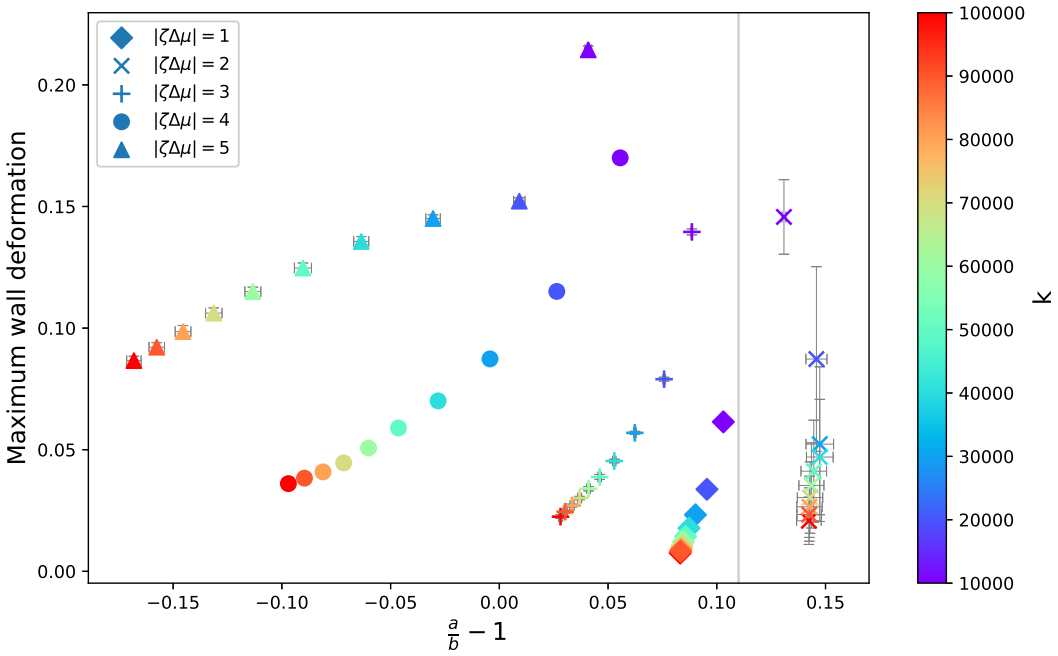

FIGURE 4.15: Maximum deformation of the wall away from the reference state, for a channel width $3R_0$, against the difference between the aspect ration $\frac{a}{b}$ and the aspect ratio of a circle: 1. The colour bar indicates the stiffness of the channel. This is for droplets with activities $\{1, 2, 3, 4, 5\}$. The grey vertical line is an estimate of the deformation caused by the periodic induced flow, from looking at figure 4.11.

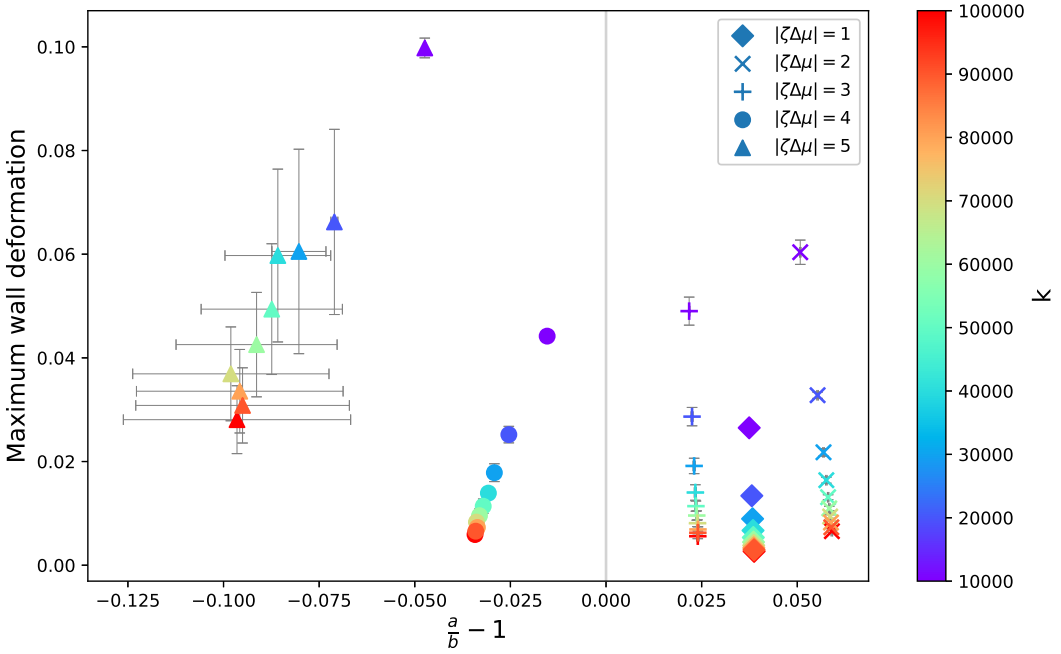

FIGURE 4.16: Maximum deformation of the wall away from the reference state, for a channel width $5R_0$, against the difference between the aspect ration $\frac{a}{b}$ and the aspect ratio of a circle: 1. The colour bar indicates the stiffness of the channel. This is for droplets with activities $\{1, 2, 3, 4, 5\}$. The grey veritical line denotes the case where the droplet is undeformed from a circle.

4.1.2.3 Droplet trajectory

In chapter 3 we found that droplets in a channel can oscillate. In figure 3.9 we can see which droplets do and do not oscillate in rigid channels. We now look at the effect of wall stiffness on droplet trajectory. The deformable wall simulations take much longer to run than the rigid walls simulations, due to the high number of immersed boundary points and increased simulation box size. As such we ran these for less time and they did not all reach steady state.
In figure 4.17 we have plotted a phase diagram of wall stiffness vs activity for channel widths $\{3R_0, 4R_0, 5R_0\}$. We have split the simulations into 4 groups; those where the droplet swims along the channel centre line, droplets which oscillate and have reached a steady amplitude, droplets which oscillate with an increasing amplitude and droplets which oscillate with a decreasing amplitude. Based on our simulations from the previous chapter, we expect that droplets with increasing oscillations will eventually reach a steady amplitude and droplets with damped oscillations will eventually swim along the centre line.

We see a difference in droplet behaviour, compared to rigid channels. Particularly in width $3R_0$ where the interaction of the droplet generated forces with the wall is higher. In figure 4.17a we can see that for activities 3 and above there are no oscillations in the channel for any stiffness (although, not shown here, if we increase k to 10^6 then we do see oscillations in line with the rigid channel case). For the wider channels in figures 4.17b and 4.17c we see a suppression of oscillation in the low k high activity regime. Essentially, when the droplet can sufficiently deform the walls such that the

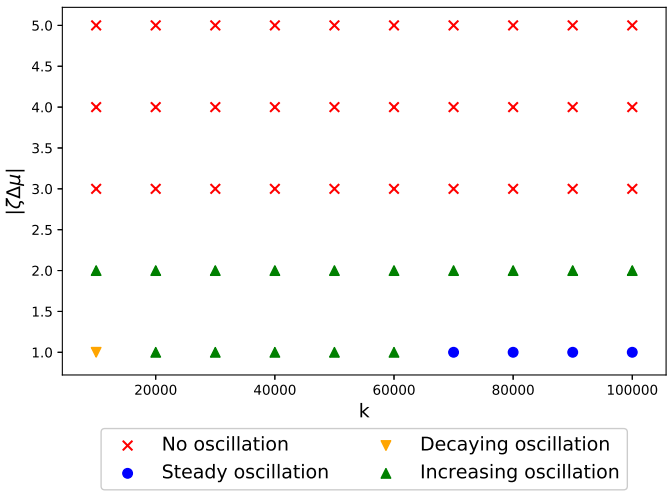

(A) Width $3R_0$

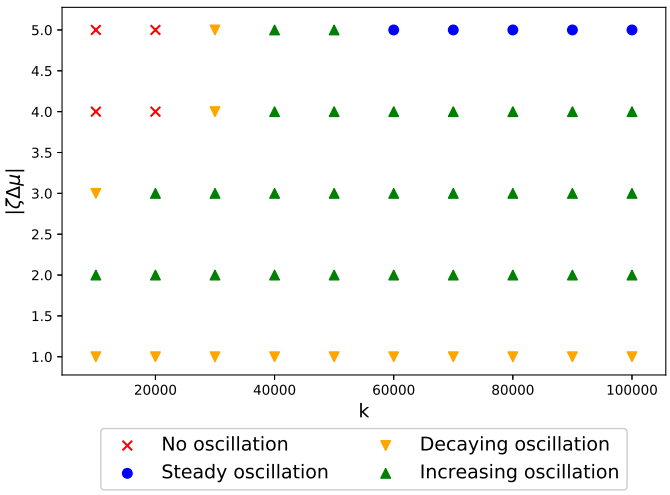

(B) Width $4R_0$

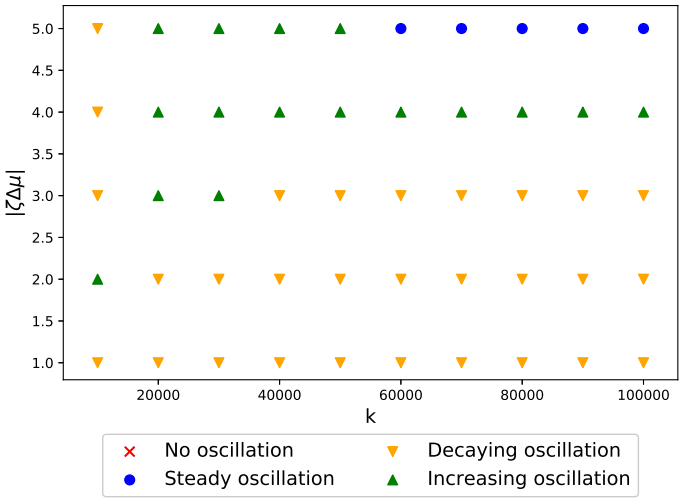

(C) Width $5R_0$

FIGURE 4.17: Phase diagrams of droplet activity $|\zeta\Delta\mu|$ against channel stiffness, k. Droplets fall in to 4 categories, no oscillation, decaying oscillation, increasing oscillation and steady amplitude oscillation.

torque generated from the asymmetry in the velocity field from interaction with a no slip wall, is small compared to the other forces, then the droplet will not oscillate.

4.1.3 Constrictions

Now that we have quantified the behaviour of an active droplet in a simple channel we now will look at what happens when the droplet encounters a constriction. We construct a constriction, using piecewise trigonometric functions to ensure no sharp angles. In figure 4.18 we show the geometry of our constriction We chose initially a constriction width the radius of the droplet, R_0, while the remainder of the channel is the width of the cell $2R_0$. The channel length remains at $12R_0$, as with all of our deformable walls simulations, the length of the main channel is $6R_0$, the length of the constriction is $4R_0$ and there is a length of R_0 over which the channel changes in width.

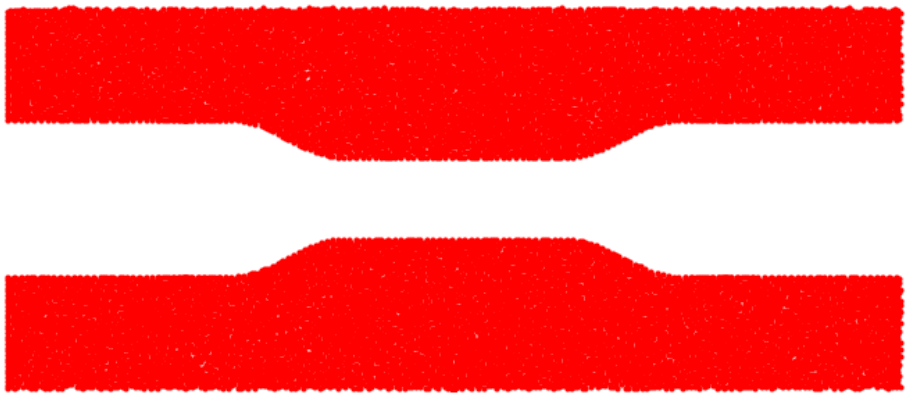

FIGURE 4.18: Diagram of the constriction geometry, the constriction width is R_0 and the main channel is width $2R_0$. The length of the constriction is $4R_0$, the length of the main channel is $6R_0$ and the length of each transition section is R_0.

We initially look at the case where we have a very rigid channel, setting $k = 10^6$. And run simulations for droplets with $\zeta\Delta\mu = \{1, 2, 3, 4, 5\}$. We then also vary the activity looking at constrictions where $k = \{1 \times 10^4, 5 \times 10^4, 1 \times 10^5\}$.

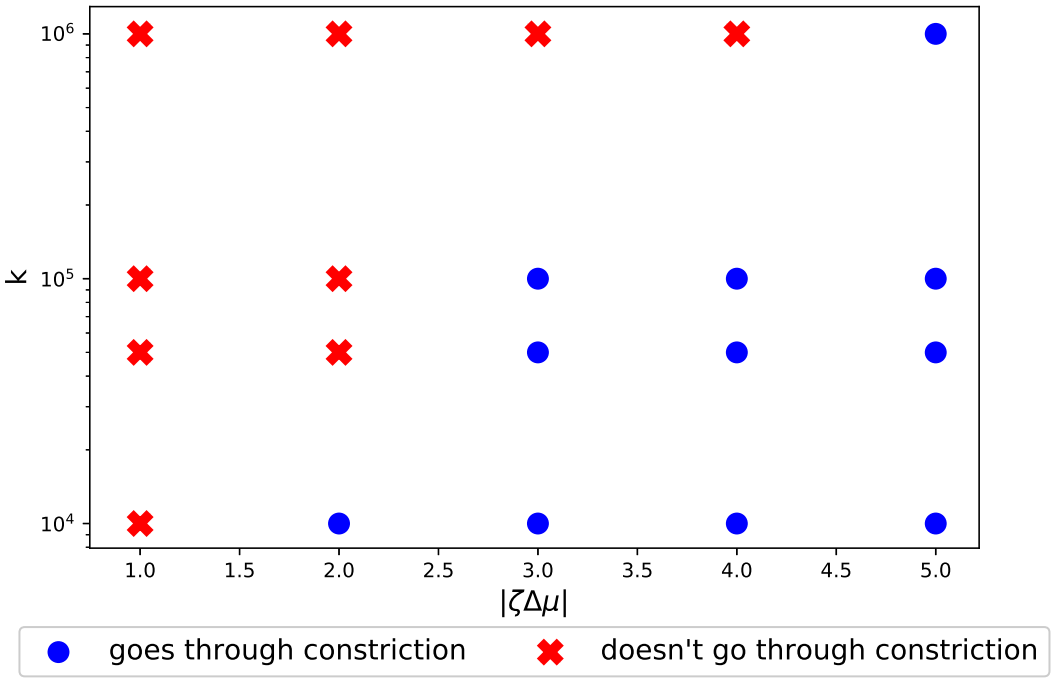

FIGURE 4.19: Phase diagram of spring constant against activity for whether a droplet goes through the constriction in the channel or not.

We find that for the case with the highest spring constant, which is close to rigid, only the highest activity droplet went through the constriction. But we see in figure 4.19, that, by decreasing the stiffness of the channel, droplets which did not previously go through the constriction, can now pass through the channel

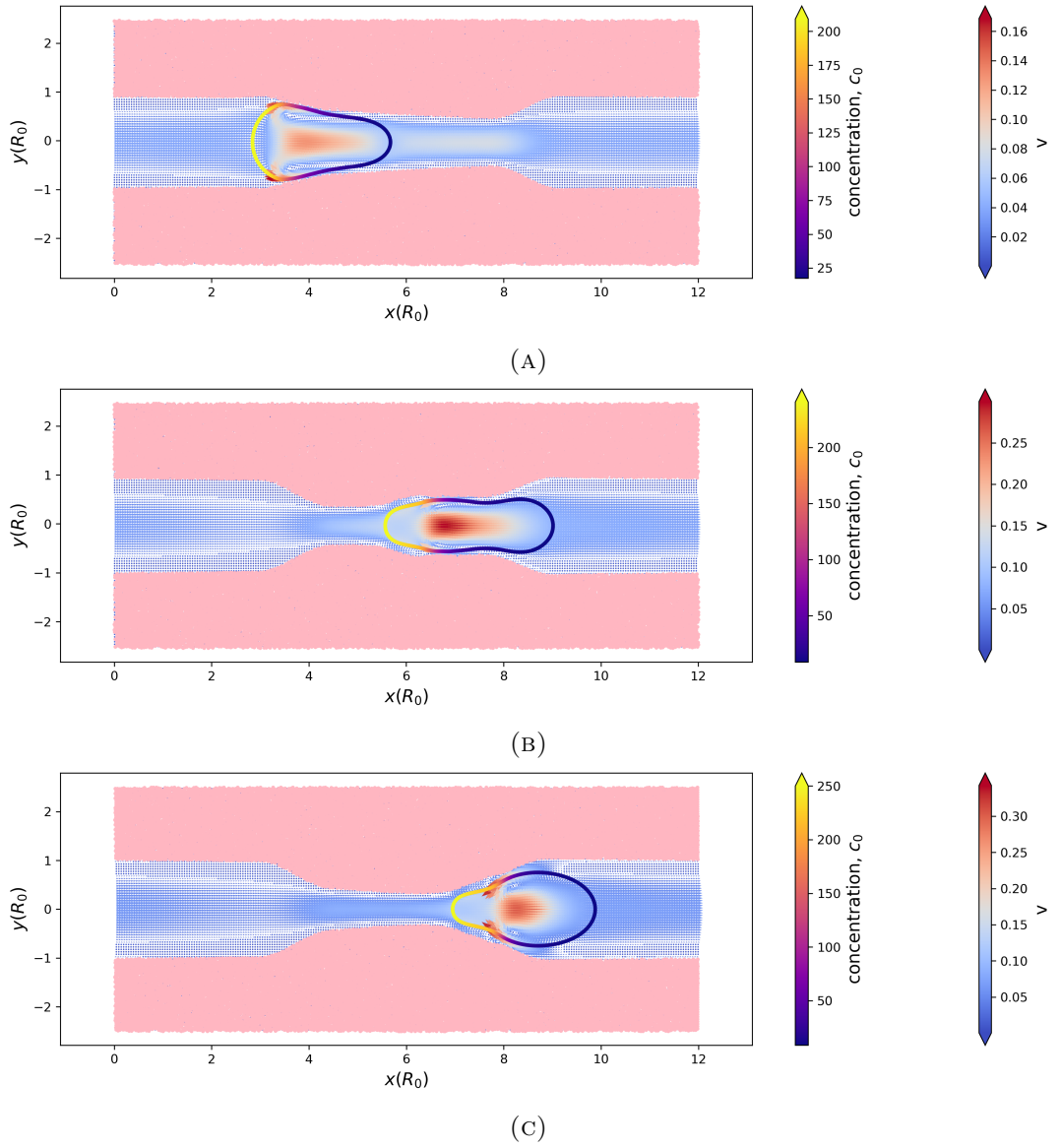

FIGURE 4.20: Snapshots of a droplet passing through a constriction with $k = 10^5$. The droplet parameters are: $\eta = 100$, $|\zeta\Delta\mu| = 3$. the red to blue colour bar shows the velocity field of the fluid and the purple to yellow colour bar shows the concentration profile on the boundary.

In figure 4.20 we show an example of a droplet passing through a slightly deformable constriction. For this droplet where $|\zeta\Delta\mu| = 3$ we see in 4.19 that for a more rigid constriction, the droplet could not pass and turned around. Here we that the droplet slightly deforms the constriction as it is entering and passing through it.

4.2 Neo-Hookean Model

In section 4.1 we used a spring lattice to model an elastic wall. We see that there are deformations of the wall which are greater than 10% of the cell radius for several different parameter combinations of activity and spring constant. This is especially the case for channels the width of the droplet, see figure 4.9. As such, the assumption of small strain no longer holds. We look to non-linear models of elasticity to address this.

Hyperelastic models are used to model materials which behave elastically when subject to finite deformation [102]. Constitutive laws for hyperelastic materials are given by an equation for the strain energy density as a function of the deformation gradient tensor. The stress-strain relationship can then be recovered by differentiating the strain energy density. There are a great variety of hyperelastic models which can roughly be classified into two groups: Phenomenological models which fit experimental data to find coefficients for the strain energy density, and micro-mechanical models which are derived from the microscopic structure of the material [103]. We know that biological tissues do not behave as linear elastic solids, and there is precedent for modeling them as hyperelastic materials [104], [105].

We chose to use the generalised neo-Hookean model, for which the strain energy density is given by [102], [101]:

$$W = \frac{\mu_E}{2}\left(\frac{\mathrm{Tr}\left(\mathcal{A}\mathcal{A}^T\right)}{J^{\frac{2}{d}}} - d\right) + \frac{\kappa_E}{2}(J-1)^2. \tag{4.4}$$

$\mathcal{A}$ is the deformation gradient tensor, J is the determinant of $\mathcal{A}$, d is the number of dimensions and μ_E, κ_E are material properties which, for small deformations, are the shear and bulk modulus respectively. This is a mechanistically derived model, where the coefficients are derived from the statistical thermodynamics of polymer chains [102]. As we are modelling cells moving through the extracellular matrix, which comprises, admittedly fairly complex, biopolymers, this seems like a good choice. The other reason for using this model is that it has a small number of parameters and for small deformation the model can be reduced to linear elasticity .

4.2.1 Method

This model, initially developed by Devendran and Peskin [106], uses the functional derivative of the strain energy density, to determine forces on immersed boundary points in the mesh. We assume a hyperelastic material, such that the constitutive law for the material can be written in terms of it's strain energy density, $W(\mathcal{A})$ as defined in equation 4.4. Here $\mathcal{A}$ is the deformation gradient tensor which maps the reference configuration to the deformed state.

$$\mathcal{A}_{ij} = \frac{\partial X_i}{\partial s_j} \tag{4.5}$$

Where X_i is the deformed state and s_i is the reference state. The use of this type of model removes the need to directly calculate the stress tensor. The total energy, E, of the material domain, Λ is:

$$E = \int_\Lambda W(\mathcal{A}) d\vec{s} \tag{4.6}$$

and so the force is given by:

$$\vec{F}^{El}(\vec{s},t) = -\frac{\delta E}{\delta \vec{X}}(\vec{s},t) \tag{4.7}$$

As stated, we have chosen a generalised neo-Hookean description of our material, the 2D expression for the strain energy density W is[101]:

$$W(\mathcal{A}) = \frac{\mu_E}{2}\left(\frac{\mathrm{tr}(\mathcal{A}\mathcal{A})}{\det(\mathcal{A})} - 2\right) + \frac{\kappa_E}{2}(\det(\mathcal{A}) - 1)^2 \tag{4.8}$$

4.2.1.1 Discretisation

In this section we follow methods outlined in [106] and [101].

For our unstructured mesh let each triangle in it's reference configuration be defined by the vectors $\tilde{\vec{s}}^{(1)} = \vec{s}^{(1)} - \vec{s}^{0}, \tilde{\vec{s}}^{(2)} = \vec{s}^{(2)} - \vec{s}^{0}$, where $0, 1, 2$ label the vertices of a triangle in the mesh, and similarly for the deformed configuration $\tilde{\vec{X}}^{(1)}, \tilde{\vec{X}}^{(2)}$. The mapping from the reference state, s_i, to the deformed state, X_i, assuming a linear deformation is given by:

$$\begin{pmatrix} \tilde{X}_x^{(1)} & \tilde{X}_x^{(2)} \\ \tilde{X}_y^{(1)} & \tilde{X}_y^{(2)} \end{pmatrix} = \mathcal{A} \begin{pmatrix} \tilde{s}_x^{(1)} & \tilde{s}_x^{(2)} \\ \tilde{s}_y^{(1)} & \tilde{s}_y^{(2)} \end{pmatrix} \tag{4.9}$$

$$\mathcal{A} = \begin{pmatrix} \tilde{X}_x^{(1)} & \tilde{X}_x^{(2)} \\ \tilde{X}_y^{(1)} & \tilde{X}_y^{(2)} \end{pmatrix} \begin{pmatrix} \tilde{s}_x^{(1)} & \tilde{s}_x^{(2)} \\ \tilde{s}_y^{(1)} & \tilde{s}_y^{(2)} \end{pmatrix}^{-1} \tag{4.10}$$

We can write equation (4.6) in a discretised form:

$$E = \sum_{T \in \mathcal{T}} W(\mathcal{A}) A_{ref}(T) \tag{4.11}$$

Where $\mathcal{T}$ denotes all the triangular elements in the mesh, and $A_{ref}(T)$ is the area of a triangle in the reference configuration., T. The force, $\vec{F}_T^{(k)}$ on a lattice point, k, exerted by triangle T is then given by:

$$\vec{F}_T^{(k)} = -\sum_{i,j=1}^{2} \frac{\partial W}{\partial \mathcal{A}_{ij}} \frac{\partial \mathcal{A}_{ij}}{\partial \vec{X}^{(k)}} A_{ref}(T), \tag{4.12}$$

and so the total force on each point, $\vec{F}^{(k)}$, is given by the sum of the forces exerted by triangles containing point k.

To calculate $\frac{\partial \mathcal{A}_{ij}}{\partial \vec{X}^{(k)}}$ we recall that $\tilde{\vec{X}}^{(i)} = \vec{X}^{(i)} - \vec{X}^{(0)}$, here $\vec{X}^{(0)} = \vec{X}^{(k)}$, and using equation (4.10) we find:

$$\frac{\partial \mathcal{A}_{ij}}{\partial X_x^{(k)}} = \begin{pmatrix} -1 & -1 \\ 0 & 0 \end{pmatrix} \begin{pmatrix} \tilde{s}_x^{(1)} & \tilde{s}_x^{(2)} \\ \tilde{s}_y^{(1)} & \tilde{s}_y^{(2)} \end{pmatrix}^{-1} \tag{4.13}$$

$$\frac{\partial \mathcal{A}_{ij}}{\partial X_y^{(k)}} = \begin{pmatrix} 0 & 0 \\ -1 & -1 \end{pmatrix} \begin{pmatrix} \tilde{s}_x^{(1)} & \tilde{s}_x^{(2)} \\ \tilde{s}_y^{(1)} & \tilde{s}_y^{(2)} \end{pmatrix}^{-1}. \tag{4.14}$$

This expression is only dependent on the reference configuration so can be precalculated at initialisation.

Then, finally, the expression for $\frac{\partial W}{\partial \mathcal{A}_{ij}}$ is given by [101]:

$$\frac{\partial W}{\partial \mathcal{A}_{ij}} = \mu_E \left(\frac{\mathcal{A}_{ij}}{\det(\mathcal{A})} - \frac{\mathrm{tr}(\mathcal{A}\mathcal{A}^T)\mathcal{A}_{ij}^{-T}}{2\det(\mathcal{A})} \right) + \kappa_E(\det(\mathcal{A}) - 1)\det(\mathcal{A})\mathcal{A}_{ij}^{-T} \tag{4.15}$$

The method described in chapter 2 is used to transfer the calculated forces to the fluid. There is a small difference in the discrete version of equation (2.33), which in this case does not contain the factor of d$\vec{s}$, as $\vec{F}^{(k)}$ is already $\mathcal{O}(d\vec{s})$ [106]. So it becomes:

$$\vec{f}_\alpha(\vec{x}, t) = \sum_k^N \vec{F}_\alpha^{(k)} \delta_h(\vec{x} - \vec{X}) \tag{4.16}$$

Where δ_h is the 2d numerical delta function, N is the number of points in the mesh, and $\vec{x}$ is the coordinate in the bulk.

4.2.2 Comparison to Spring Model

We compare our model to the spring lattice model. In order to find the equivalent values for μ_E and κ_E, we make the assumption that they are equal to the shear and bulk modulus for linear elasticity. For a 2D spring lattice the Poisson ratio, ν is 1/3, the 2D expression for the Poisson ratio is:

$$\nu = \frac{\lambda}{\lambda + 2\mu}, \tag{4.17}$$

where λ is the first Lamé coefficient, so, $\lambda = \mu$ and by definition $\kappa = 2\lambda = 2\mu$. Using equation (4.2), with $d_{ij} = h$, as our mean spring length is h, and that our triangle area is $\frac{\sqrt{3}}{4}h^2$. We also have to include a factor of area to account for the difference in immersed boundary implementation in equation (4.16). We end up with:

$$\mu = \frac{3}{16}hk \tag{4.18}$$

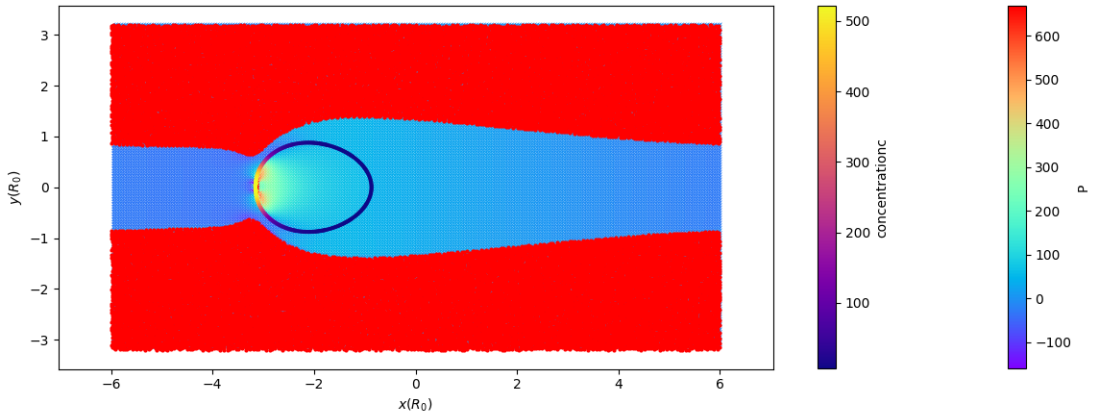

FIGURE 4.21: Droplet with activity 10, $\eta = 1000$, $k = 10000$. The walls are comprised of a non-uniform mesh of immersed boundary points, where the forces are calculated using a neo-Hookean model, the snapshot is from the final timestep of the simulation.

In figure 4.21 we show a snapshot from the final timestep of a simulation using neo-Hookean method to model the walls. We see that the deformation profile of the walls and concentration levels are similar to those in the spring lattice case. We plot the same graphs as in section 4.1.1. We see in figure 4.22, that the droplet speed, $|v|$ is slightly higher using this model. In figure 4.23 the minimum channel width is slightly smaller and the maximum channel width is slightly larger. Recall that we made the assumption of linear elasticity to convert the spring constant to a modulus. We can see in figure 4.21 that the deformation of the channel is large, so this doesn't hold, explaining the difference in behaviour.

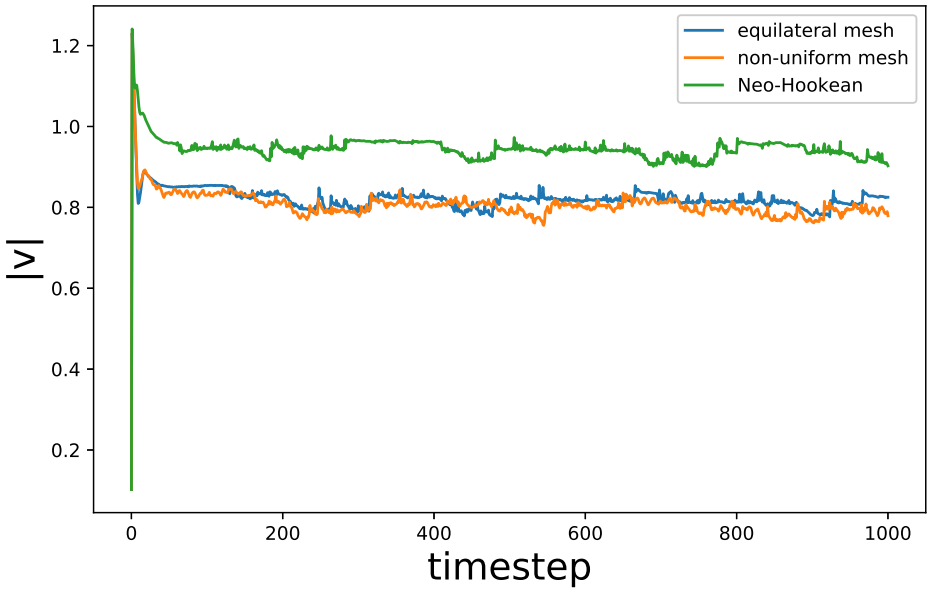

FIGURE 4.22: Centre of mass speed for active droplets in channels with equilateral or non-uniform triangular spring lattices, and for the neo-Hookean model using the same non-uniform triangular mesh.

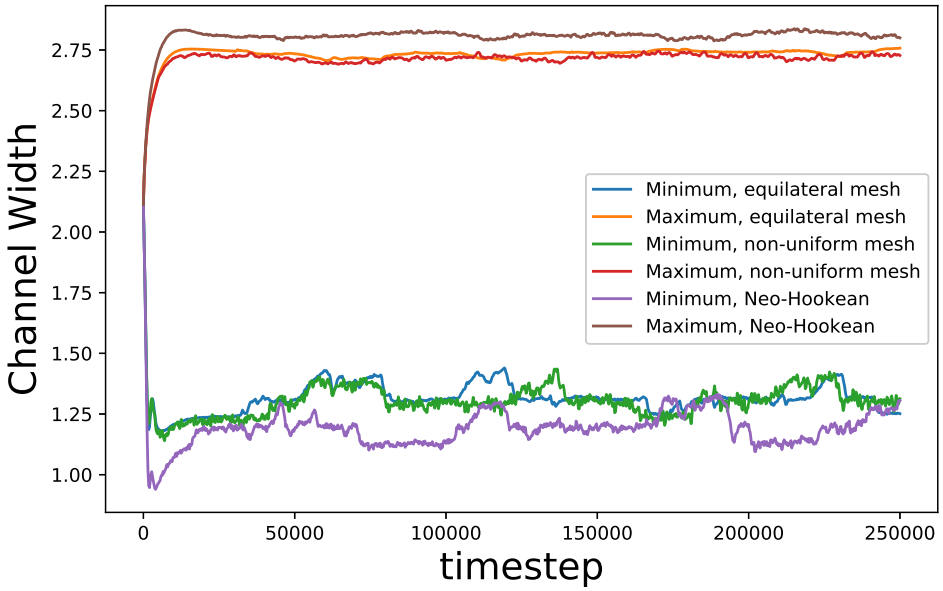

FIGURE 4.23: Minimum and maximum channel width for channels with equilateral or non-uniform triangular spring lattices, and for the neo-Hookean model using the same non-uniform triangular mesh.

4.2.3 Narrow channels, $w = R_0$

We use this model to look at highly confined droplets, as we saw larger deformation in the wall as we decreased the channel width, as such a hyperelastic model is more appropriate. In *in vivo* and in *in vitro* experiments such as cells in microchannels, cells are confined to spaces much smaller than their diameter. Here we place droplets in channels with width R_0. As with previous simulations, for comparison, we use viscosity, $\eta^{(int)} = \eta^{(ext)} = 100$ and activities, $\zeta\Delta\mu = \{1, 2, 3, 4, 5\}$. We are using the neo-Hookean wall model and we look at Elastic moduli, $E = [1000, 10000]$.

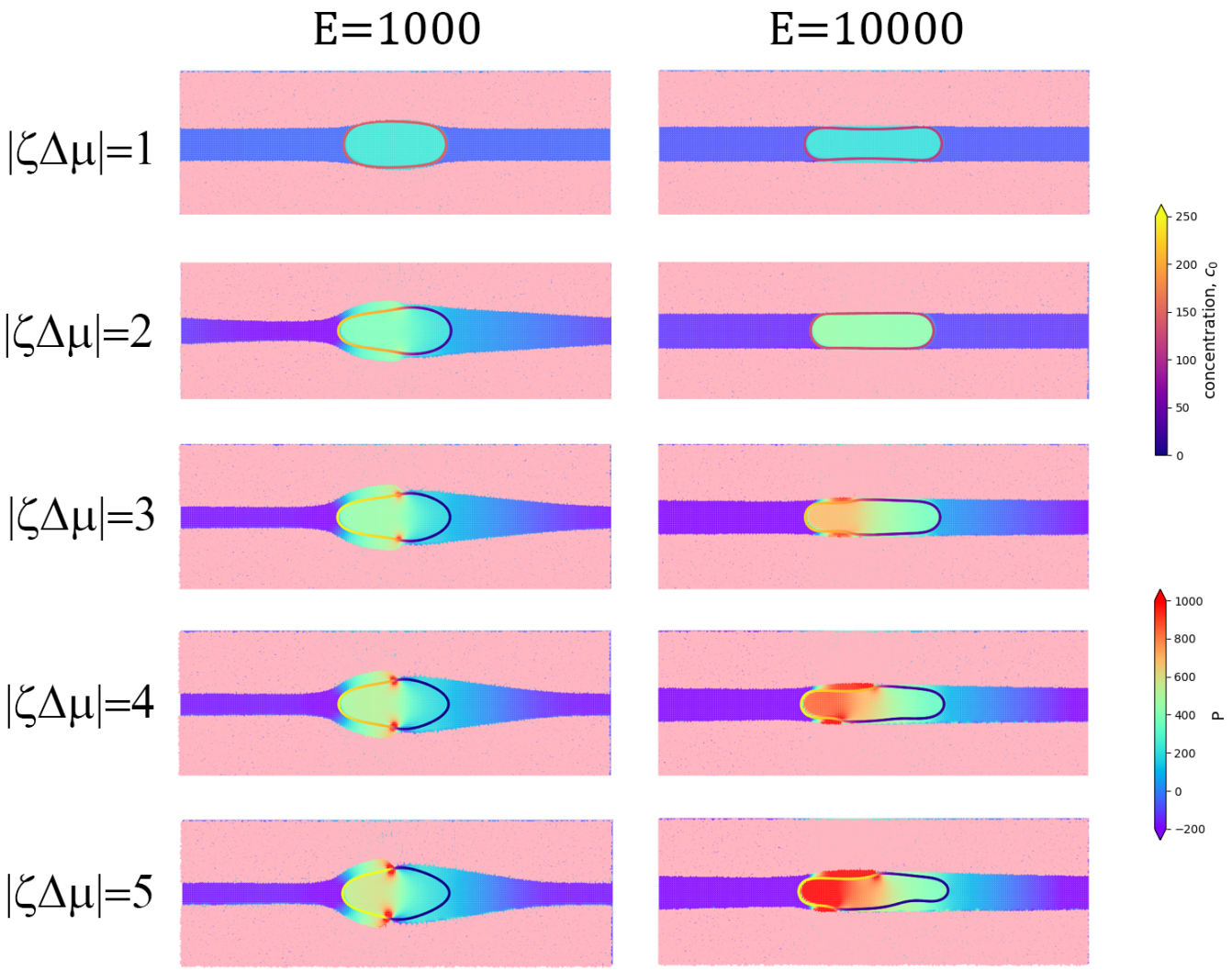

FIGURE 4.24: Simulation snapshots of droplets at steady state, where the snap shots are all recentred so the droplet centre of mass is at zero. The droplets have parameters $|\zeta\Delta\mu| = \{1, 2, 3, 4, 5\}$, $\eta = 100$, and the walls, here in pink, have an elastic modulus of either 10^3 or 10^4. The rainbow colour bar shows pressure and the purple/yellow colour scale denotes concentration on the boundary, where the yellow high concentration region is at the rear of the droplet. Channel width, $w = R_0$

In figure 4.24 we show snapshots of the droplets for softer and more rigid channels. We see that for the more rigid channel on the right, droplets require a higher activity to be motile (see figure 4.25), than the softer channel on the left. We also see that as the droplet is very constrained shape, as there is no space for it to deform. As a consequence of this droplets with activity > 3 have adopted an asymmetric shape and have offset vortices (not pictured here) rather than a symmetric pair.

It is interesting to look at the non-motile droplet for $|\zeta\Delta\mu| = 1$. In the softer channels it pushes the walls out as it tried to deform back to a circle. In the more rigid channel it does not generate enough force to deform the walls and instead the sides of the droplet bend in away from the channel walls.

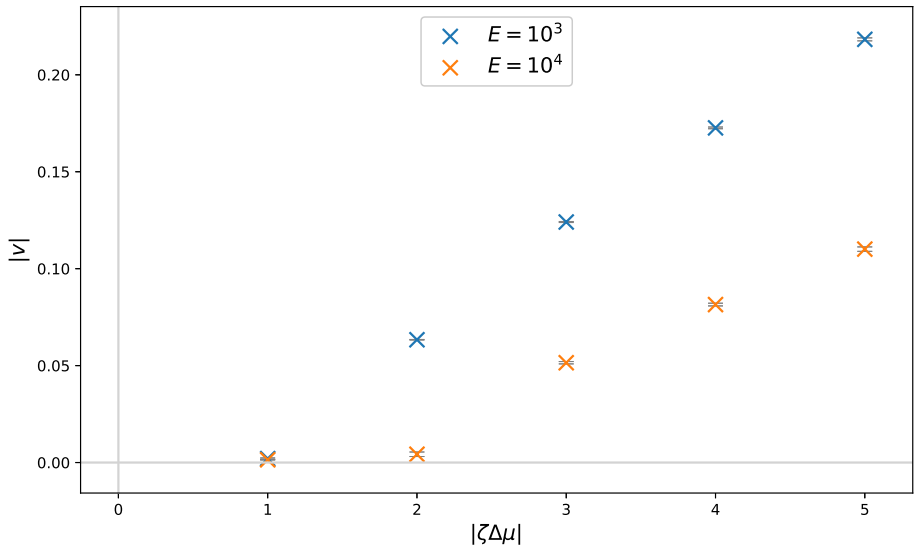

FIGURE 4.25: Centre of mass velocity for the droplet, $|v|$, against activity,$|\zeta\Delta\mu|$. For elastic moduli 10^3 and10^4.

Figure 4.25 shows the velocity of the droplets in these channels as a function of activity. The droplets in the rigid channel are slower, which is the same as what we saw in wider channels. The rigid channels also require higher activity for the droplet to move in the channel.

4.3 Summary

In this chapter we have introduced two models for deformable walls. We first used a spring lattice constructed from immersed boundary points to model a linear elastic solid. We varied the average spring constant of the walls to see how wall stiffness affected droplet motion.

We found that in more deformable channels droplets move faster and the velocity decays exponentially to a plateau at the velocity of a droplet confined by infinitely rigid

walls, as the spring constant increases. We found that there is a balance in droplet and wall deformation, which are inversely correlated. In the previous chapter we found that some droplets oscillated in channels. When we allow the walls to deform we find that for a small enough spring constant to activity ratio the oscillation's were damped by the deforming walls and droplets swam along the centre line of the channel. We constructed phase diagrams to capture the behaviour.

We then turned to changing the channel geometry and constructed a constriction for the droplets to go through. For a very high spring constant, only the droplet with the highest activity went through the constriction. The others changed direction in the channel. When we lowered the spring constant, this allowed some of the lower activity droplets to enter and pass through the constriction.

The second model for confining walls was a hyperelastic model, specifically a neo-Hookean material. We used this model to explore droplets in channels smaller than their diameter. We see that there are differences in cell shape, threshold for motion and droplet translational velocity for different values of the elastic modulus.

Chapter 5

Conclusion and Future Work

5.1 Conclusion

In Chapter 2 we have introduced a mathematical model of an active droplet for a cell migrating under amoeboid motion. We probed the system using linear stability analysis, but in order to examine the non-linear behaviour of our coupled system, we resorted to using numerical methods to solve the model. We detail our methodology using the immersed boundary method which allowed us to fully investigate a deformable active droplet.

We varied the viscosity of the fluid inside the droplet and the surrounding fluid and found the relative slip between the two fluids decreases the minimum activity threshold required for migration and also leads to deformation away from a circular shape of the droplet.

We explored how the droplets deform and the roles that the stresslet and symmetric quadrupole moments play in determining whether a droplet will elongate along or perpendicular to the axis of motion. We also looked at how the length of the active region is important in determining the balance of force moments. We grouped droplets into different clusters of behaviour based on their force moments and resultant deformation. We also considered droplets transitioning between groups.

We then mapped the swimming behaviour of our droplets to the squirmer model for a swimmer and related the squirmer parameter, β to the force moments calculated from our simulations.

In chapter 3 we looked at the effect of confining a droplet by infinitely rigid walls. We chose droplet parameters, based on findings from studying the unconfined droplet, such that we had a range of stresslets, which were positive and negative. We placed these droplets in channels of varying lengths and widths.

In channels the width of the undeformed droplet diameter, we found that the velocity decays exponentially with channel length to a non-zero plateau. This is due to the droplet having to push the fluid in front of it. For a slightly wider channel: $w = 3R_0$, as we increased the channel length we saw the onset of oscillations which increased in amplitude, tending to a plateau, as the channel increased in length.

For the channels where we varied the width, we saw that the centre of mass speed of the droplet decreased from the unconfined speed as the channels got narrower. We saw that confinement increases the deformation of the droplet. The narrower

the channel the more deformed away from a circle the droplet was. The additional external pressure gradient, which increases as the channel gets narrower, increases the pressure jump across the boundary altering the ratio of tension and the normal constraint, and therefore the curvature. As the option to deform perpendicularly to the channel is suppressed by the channel walls in narrow channels, any change in curvature necessitates the droplet elongates along the channel.

For confined droplets in channels with width $3R_0$ and above, we observed that, under certain circumstances, droplets would oscillate in the channel, rather than swimming persistently as they did when they were unconfined. Droplets with a positive stresslet (pushers) will oscillate in the channel. However droplets with a negative stresslet (pullers) , which have a lower activity, experience greater effects from induced channel flow. In wider channels these pullers will swim along the centre line. For narrower channels the induced flow from periodic confinement has a larger effect and can induce rotation and thus oscillation for pullers in the channel.

In chapter 4 we introduced two models for deformable walls. We first used a spring lattice constructed from immersed boundary points to model a linear elastic solid. We varied the average spring constant of the walls to see how wall stiffness affected droplet motion.

We found that in more deformable channels droplets move faster and the velocity decays exponentially to a plateau at the velocity of a droplet confined by infinitely rigid walls, as the spring constant increases. We found that there is a balance in droplet and wall deformation, which are inversely correlated. In channels with infinitely rigid walls we found that some droplets oscillated between the channel walls. When we allow the walls to deform we find that for a small enough spring constant to activity ratio the oscillations were damped by the deforming walls and droplets swam along the centre line of the channel. We constructed phase diagrams to capture the behaviour.

We then looked at the effects of channel geometry and constructed a constriction in the $w = 2R_0$ channel which reduced to $w = R_0$ at the narrowest point. For a very high spring constant, k, only the droplet with the highest activity went through the constriction. The others changed direction in the channel. When we lowered the spring constant, this allowed some of the lower activity droplets to enter and pass through the constriction.

The second model for confining walls was a hyperelastic model, specifically a neo-Hookean material. We used this model to explore droplets in channels smaller than their diameter, as we see large deformations relative to the droplet radius for deformable channels the width of the droplet. We see that there are differences in cell shape, threshold for motion and droplet translational velocity for different values of the elastic modulus.

This work was motivated by breast cancer cell metastasis, in particular to the bone microenvironment. A metastatic cell will encounter many different external environments as it moves through the body: Epithelial cells, the extracellular matrix (in various tissues), lymphatic or blood vessels and calcified bone to name a few. Each of these has drastically different mechanical properties. We set out to build a model of a cell confined by a generic material with tunable parameters to understand cell

migration in different confined environments. In our spring lattice model we can alter the spring constant of the channel to make the walls more or less deformable. We can also make different geometries for a droplet to encounter. In our neo-Hookean model we can vary the effective moduli and are no longer constrained in the value of Poisson ratio. Furthermore the way the walls are set up, different hyperelastic materials could easily be looked at by changing the form of the strain energy density. In [future work section] we discuss how this could be extended to include viscoelasticity or a possible active response.

Speed and persistence are often important factors in cell migration, for example when immune response cells move rapidly to their target. In chapter 2 we saw that the viscosity difference between the internal and external fluid reduced the activity threshold for persistent droplet motion and increased the translational velocity of the droplet. When the droplet is confined by no-slip walls we find that as the channel decreases in width the droplet's translational velocity decreases. This is partly because as the channel width approaches the droplet radius, R_0, the space for retrograde flow of fluid in the channel decreases and the droplet must push more fluid. But it has also been shown that even the presence of a single wall decreases droplet velocity [65]. We saw in 4 that when a droplet migrates in a channel with sufficient activity to deform the walls that it moves faster than in a rigid channel and persistently along the centre line rather than oscillating. Most work on the effects of stiffness on migration has been looking at adherent modes of migration. Our model shows that focal adhesion-free migration can still be affected by environmental stiffness and that the material properties of the environment can enhance motility. It has been seen that the presence of a tumour can alter the stiffness of the ECM [107]. Mechanical signals are used to guide collective migration in embryogenesis [108]. So by tuning the stiffness of tissues and viscosities of biological fluids it may be possible to control the speed of cell migration in a tissue, either to help or hinder.

Cell deformation is important in cell migration when navigating complex environments. Particularly for amoeboid migration where proteases are not used to break down the environment, cells need to be able to squeeze through pores and gaps in collagen networks [55]. Using the example of cancer cells again, they need to deform between endothelial cells to enter and exit the vascular system [44]. We have seen that active droplets with large viscosity differences are subject to large deformations relative to the droplet radius. For a cell with a highly viscous cytoskeleton traveling through much less viscous interstitial fluid, there is likely to be a viscosity difference. We saw a variety of shapes from our simulations, just by altering the viscosity and activity parameters. The rounded shapes were similar to breast cancer cells migrating in matrigel [57]. The kidney bean-like shape is reminiscent of the shapes of keratocytes cell fragments with their concave rears [109]. When we confine the cells we suppress some of the variety in shape, but also observe new phenomena. For example in the stiffest channels which were the radius of the cell R_0 in width in figure 4.24 we see an asymmetry in shape arise due to the incompatibility of the channel width with the size of the vortices within the droplet. We also looked at droplets traveling through constrictions and found that the balance of the deformability of the walls and the droplet determined whether the droplet would enter and pass through the constriction. We discuss in section 5.2 extending this to a variety of channel geometries.

We have constructed a general model for cells confined by a generic material and characterised the general response of droplets to different external conditions: fluid

viscosity, confinement, and deformation of the environment. The next steps are to combine these different environmental properties in order to study specific biological problems. Combining a viscosity difference with a deformable elastic environment may open up whole new regimes of cell behaviour. Introducing gradients in elastic modulus or an asymmetric geometry to the channel could also help examine the extent to which cell preference in migration can be determined mechanically. There are endless possibilities for extension to this model to help understand the mechanical effects on cell migration. In the next section we explore some of these possibilities.

5.2 Future Work

As we have seen in this thesis we have a phenomena rich system which we have barely scratched the surface of in exploring. This section details our ideas for future exploration of this system. Some of this has been implemented, but not yet fully analysed, some is more preliminary.

5.2.1 Active Droplet Model

5.2.1.1 Diffusion dynamics in the cell bulk

The numerical model has the capacity to have diffusion of active particles off and on to the boundary from the cell bulk. We did not include these dynamics in this piece of work as it would have added another layer of complexity to the model which is already fairly complex. Whitfield et al. [72] studied the effect of diffusion with the bulk, but this was only for unconfined droplets without a viscosity difference. Now that we have observed the behaviour of active droplets with a constant total concentration of active particles on the boundary, for completeness, we plan to add this behaviour back into the model to see if it drastically changes any of our results.

5.2.1.2 Combining with an active polar gel model for the cytoskeleton

Another extension to this model would be to combine the active boundary model of an active droplet with an active polar gel model. So rather than having isotropic viscous fluid within our droplet we have a polar active gel, as a model for the cytoskeleton. This functionality was built into our numerical model by Whitfield [79], but we have not used it in this project. It would be interesting to study how the combination of the active boundary model and active polar gel model for a droplet differs from the behaviour of each model individually. We would also see how confinement altered swimming behaviour for the active polar gel model.

5.2.2 Wall Model

5.2.2.1 Exploring the combined effects of viscosity and confinement

Throughout this thesis we have mainly looked at trends based on varying one set of variables at a time - eg. internal and external viscosity, wall stiffness etc. Now that we have an idea of how each of these variables affects cell migration in isolation, we will combine them to see if this reveals additional regimes of droplet behaviour. Most importantly how does a viscosity difference affect confined droplet behaviour?

5.2.2.2 Further exploration of models beyond linear elasticity

The first thing to do here is to perform a more detailed analysis of the neo-Hookean model we introduced in 4.2. We will conduct a parameter sweep across μ_E and κ_E. With this model we can also explore the effect of different Poisson ratios, unlike with the spring lattice model, which is restricted to a Poisson ratio of $\frac{1}{3}$. The way the hyperelastic version of the wall model is set up we can easily change the strain energy density to look at models of different hyperelastic materials. The current model was selected assuming that the cell was moving through a collagen matrix, as it is derived from polymer properties. However bio-polymers, like collagen are particularly complex and often hierarchical in structure, complicating network properties. A cell could be moving through any number of materials in the body, for example calcified bone, capillaries or lymphatic vessels, all of which have unique and varied mechanical properties.

Like most biological tissues, the extracellular matrix (ECM) exhibits both elastic and viscous behaviours [110]. The viscoelastic response of the ECM has been shown to influence cell migration [55]. As such, another extension to the wall model would be to implement viscoelasticity into the channel wall. We have yet to select a specific model of viscoelasticity or implementation into the system.

5.2.2.3 Active walls

As mentioned above, cells move through many heterogeneous environments in the body. One case is when our migrating cell is confined by other cells, for example in embryogenesis, intra/extravasation in cancer metastasis, or the endothelium in capilliaries. Cells are active, so when they are the confining medium they may have an active response to stress generated by the migrating cell. As such we want to extend our model for deformable walls to include activity.

5.2.2.3.1 Active boundary A first approach would be to use the existing methodology of an active boundary to create wall structures, essentially treating the walls as a long cell, where a single periodic active boundary at each side of the moving cell forms a channel. These active boundaries could be active fluid boundaries as used for the droplet. Or active elastic boundaries as flows along an epithelial/endothelial sheet, crossing cells, makes less physical sense than cortical flows for one cell. This may also be a good place to introduce the active polar gel model, by having the fluid enclosed by the periodic boundaries as an active polar liquid crystal to model active response from the cytoskeleton.

5.2.2.3.2 Active solid The other option is to model the walls as an active solid. It will probably be easier to use the spring model as a base. We plan to take the microscopic disordered 1D model for an active solid from [28] and extend it to the context of a 2D triangular mesh. The basic idea is that we would keep the underlying architecture of the mesh with springs connecting lattice points, then stochastically springs can become active based on motors binding on and off the spring. When active we would add a contractile dipole on the spring.

5.2.2.4 Gradients in stiffness

Durotaxis for cells on a surface has been studied in detail by many groups, There has been less work exploring this phenomenon *in vivo* or for confined migration [111]. As a measure of preference for stiffness of confining material we will set up a gradient in

spring constant/modulus along our channel. Initialising our droplets in an unpolarised state with homogenous concentration on the boundary we will see whether the droplet tends to move towards or away from higher stiffness regions.

We can also set different spring constants at one wall compared to the other. We predict this will primarily alter the droplet trajectory in channels wide enough to support oscillation of the droplet. For channels the diameter of a droplet or below we may see shape changes, possibly asymmetrically, as well as differences in cell velocity.

5.2.2.5 Wall Geometry

We focused mainly on simple channels in this project, as this already provided a wealth of interesting data, but one of the main advantages of our chosen computational method is that it deals well with complex geometry. We hope to extend the project to look at the effects of this.

5.2.2.5.1 Narrow Channels, ($w \leq R_0$) We touched on narrow channels towards the end of the thesis with the neo-Hookean wall model. This is probably the most biologically relevant geometry when it comes to simple channels. We need to run these simulations for a full range of viscosity, activity and elasticity parameters to get a clear picture of migration in these channels. As the droplet is confined below its diameter, we also need to think more carefully about slip and friction with the channel walls. Fai and Rycroft have developed a 'lubricated immersed boundary method' which may be useful here [112], for explicitly dealing with lubrication flows between the channel and the droplet.

5.2.2.5.2 Varied Constrictions In chapter 4 we looked at whether active droplets would go through constrictions half the diameter of the droplet. We focused on how altering the stiffness changed whether droplets could pass through the constriction or not. But we would like to also look at how changing the geometry for a channel which has a high spring constant/elastic modulus affects whether droplets will enter and pass through a constriction. We will initially make adjustments to our original constriction geometry as seen in figure 4.18. We will first adjust the width of the constriction to find the minimum width for which each parameter droplet will pass through. Next we will look at the effect of the length of the constriction. We saw for the constriction which we studied in chapter 4, that some droplets would extend into the constriction, but ultimately retracted and moved in the opposite direction. If the constriction was a shorter length such that the extended 'nose' spanned the entire constriction, would it go through? Finally, we will look at the angle of approach and exit from the constriction.

There are also some more complex geometries of constriction that we would like to explore. Firstly a sharp intrusion into the channel, essentially two triangles above and below with a small gap between them, as seen in figure 5.1. This is a crude model for a valve like structure which could be pushed out of the way by a droplet, as seen in figure 5.1b. Following this shapshot this droplet does move through the constriction and continue along the channel.

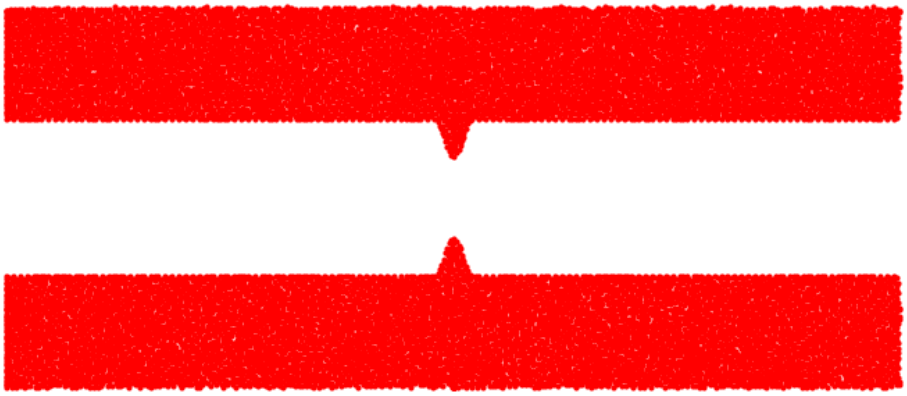

(A) Wall geometry

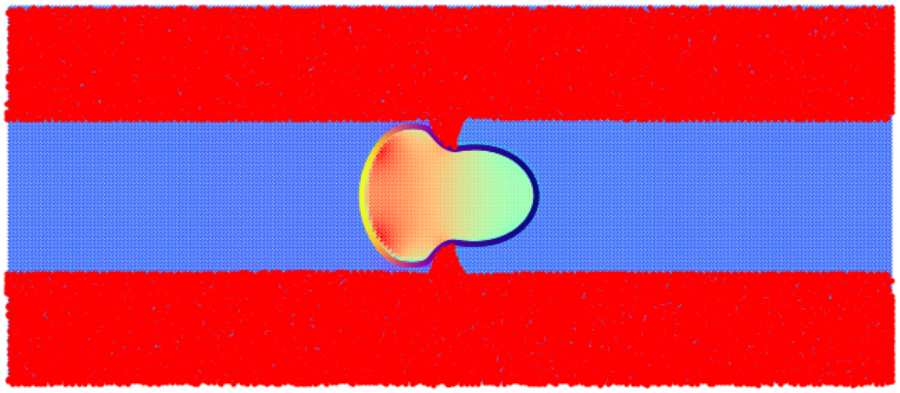

(B) Example snapshot

FIGURE 5.1: (a) shows the initial configuration of the sharp intrusion channel geometry, (b) shows an example snapshot of an active droplet pushing between the wall intrusions. Here the colourmap indicates pressure with red being high pressure regions (excluding the red wall points) and purple indicating low pressure regions. Here, $\eta^{(int)} = 500, \eta^{(ext} = 10, |\zeta\Delta\mu| = 2$.

Another interesting geometry would be an asymmetric ratchet like channel. Le Berre et al. characterised cell migration in asymmetric geometries and developed a model for migration in a ratchet geometry [113], finding that bias in migration could be explained by elastic interactions with the environment. If we initialise each droplet in a homogeneous, unpolarised state, does the geometry of the channel alter which direction droplet will travel? We have initially constructed a smooth asymmetry in the channel from trigonometric functions, as seen in figure 5.2, but we would extend this to sharper ratchets. In this case the droplet swims to the left in the direction of the least steep wall gradient.

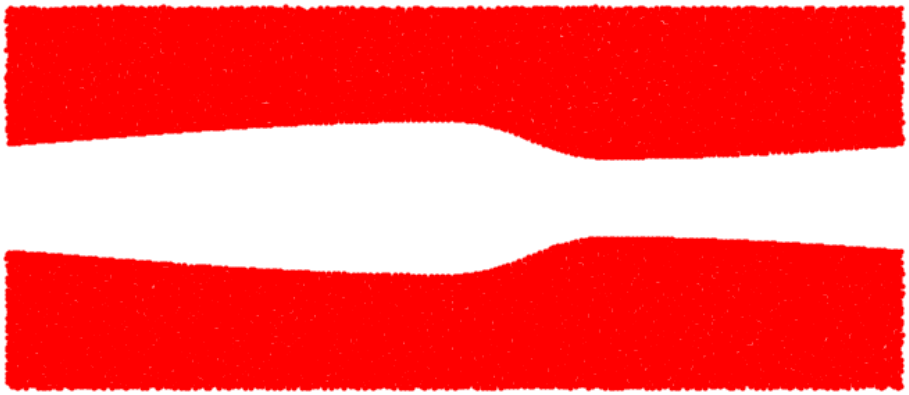

(A) Wall geometry

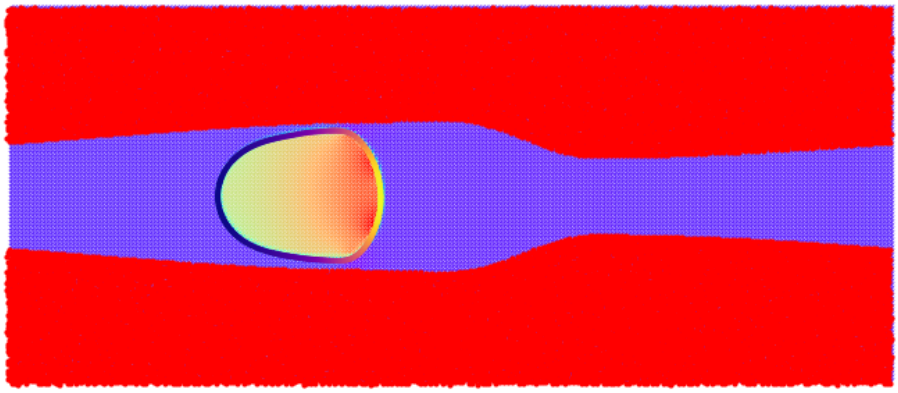

(B) Example snapshot

FIGURE 5.2: (a) The initial configuration of the asymmetric channel geometry, (b) shows an example snapshot of an active droplet moving from right to left. Here the colourmap indicates pressure with red being high pressure regions (excluding the red wall points) and purple indicating low pressure regions. The concentration on the boundary is indicated by a yellow to purple colour map, where the yellow at the cell rear indicates the high concentration region. Here, $\eta^{(int)} = 500, \eta^{(ext} = 10, |\zeta\Delta\mu| = 2$.

Following on from the work on narrow channels, we can also look at constrictions in narrow channels, where the minimum channel width is $\frac{1}{4}R_0$. In figure 5.3b we see an example of a droplet entering a narrow constriction.

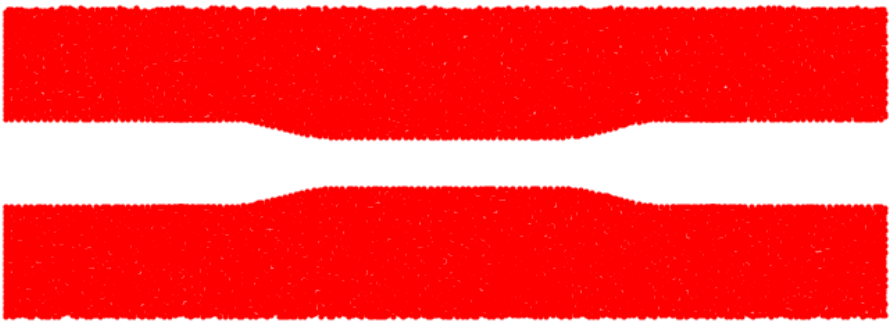

(A) Wall geometry

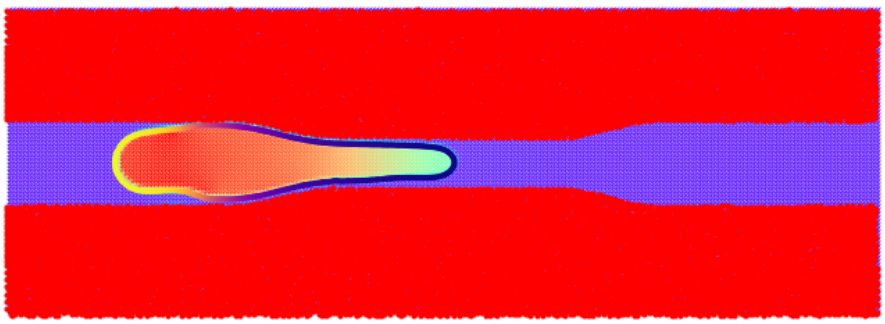

(B) Example snapshot

FIGURE 5.3: (a) shows the initial configuration of the narrow constriction geometry, (b) shows an example snapshot of an active droplet entering a constriction. Here the colourmap indicates pressure with red being high pressure regions (excluding the red wall points) and purple indicating low pressure regions. Here, $\eta^{(int)} = 100, \eta^{(ext} = 1, |\zeta \Delta\mu| = 1$.

Finally, we plan to explore channels with a regular sinusoidal deformation pattern, similar to those studied in [114]. We plan to place our droplet in 'wavy' channels of various wavelengths. We see in the deformable channel case in section 4.1.2.1.1, that when the droplet deforms the channel behind it for softer walls, there is increased droplet translational velocity. It would be interesting to see whether the interaction of our active droplet with a rigid wavy channel would enhance or hinder its motion.

5.2.2.6 Branching channels

One of the important questions in cell migration is how a cell chooses it's path. In order to examine possible mechanical mechanisms we propose using branched channels in our simulations. In [115] Zanotelli et al. place cells in branched channels constructed from collagen with different channel widths. They find that where cell preferentially adhere to one wall of the feeder channel they will pick the branch attached to that

wall, when cells touch both walls of the feeder channel they choose the wider branch $\sim 70\%$ of the time. In [116], Moreau et al. use a minimal model and branched channel experiments to look at the effect of hydraulic resistance on cell preference, this is a measure of how much force it requires to move fluid through an environment at a given speed. They show that neutrophils will follow the path of least hydraulic resistance. In our simulations we could change the width of each branch for a wide variety of widths, but also vary the stiffness as another method of exploring whether an active droplet has an affinity with higher or lower stiffness regions.

5.2.3 Other features

Aside from building on elements already existing in the model there are also some additional features we would like to add.

5.2.3.1 Addition of a nucleus

The nucleus plays an important role in cell mechanics and in migration [56]. We want to add a nucleus into our active droplet. Following work by Estabrook et al.[117] we want to eventually place the droplet with a nucleus in a constriction to see whether the nucleus will stop cells passing through constrictions of certain sizes. This is something we have done some initial work on. We have two models for the nucleus depending on whether we want to model the nucleus as an active shell or and elastic solid object, as discussed in the next two sections.

5.2.3.1.1 Elastic shell For the elastic shell model, we simply use a passive elastic immersed boundary inside our droplet, and make the internal fluid highly viscous to resist flow.

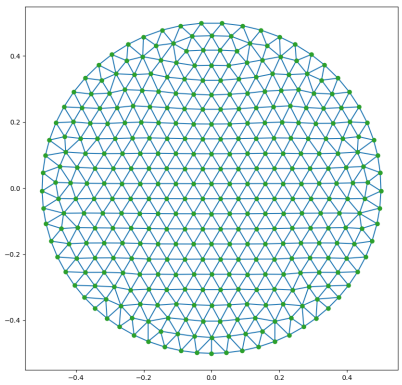

FIGURE 5.4: Triangulation of the mesh for the elastic solid nucleus

5.2.3.1.2 Elastic solid For the elastic solid, we use the same model as for the walls. We create a triangular mesh in the shape of a circle, as seen in figure 5.4 and place this inside the droplet. We chose a radius of $\frac{1}{2}R_0$. We have run some preliminary simulation for this case. We find that if we just place the nucleus object free floating in the droplet it will be funneled to one of the vortices within the cell, pushing it off centre. This in turn causes the droplet to swim in circles due to the asymmetry in the

vortices. We can see in figure 5.5 that the profile of the streamlines either side of the droplet is not symmetric, which it was peviously in droplets without the nucleus.

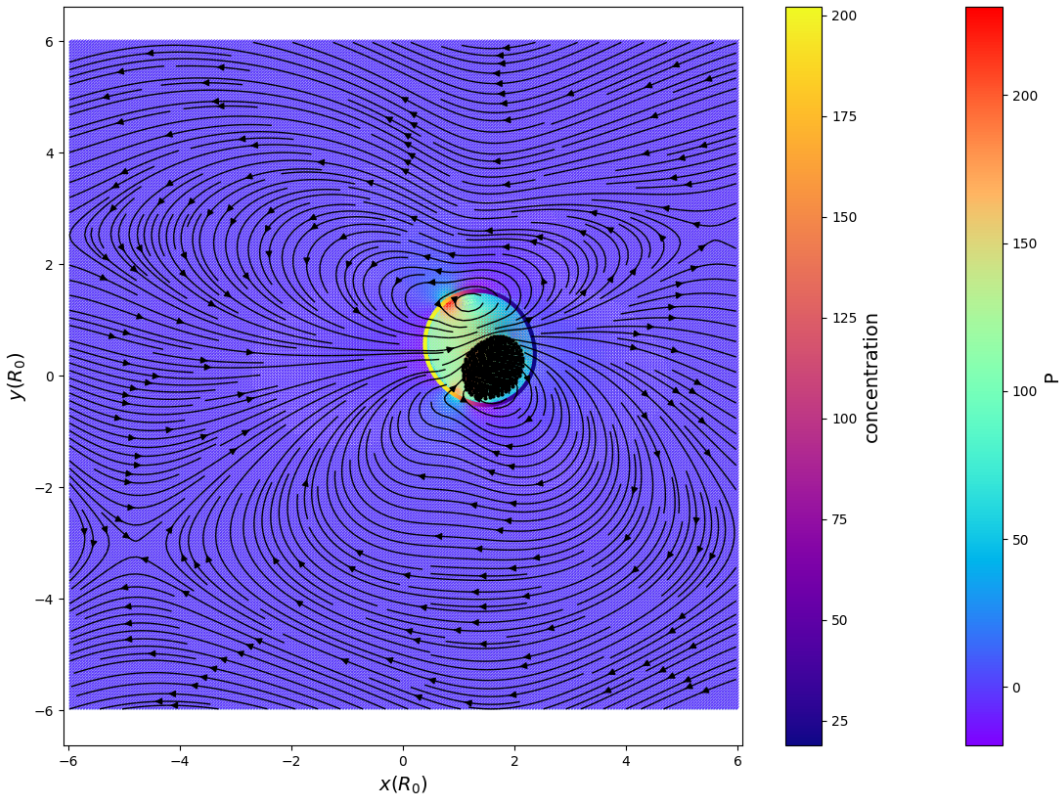

FIGURE 5.5: Example snapshot of an active droplet with an elastic solid nucleus object inside. The colourbar denotes pressure, and the black lines are streamlines.

5.2.3.2 Multiple droplets

We talk in the thesis, about the self interaction of the droplet with itself due to periodic boundaries being like interacting with a droplet in front and behind itself. But what if we had explicit multiple droplets? The interaction of squirmers and other microswimmers with each other leads to a rich space of phenomena. Our droplets are deformable, which is uncommon in these studies, so looking at the deformation of droplets as they interact would be interesting. How droplets with differing internal viscosity interact with each other, and how this differs from the identical case, or for different base tensions. We know that one of the differences between epithelial cells and metastatic cancer cells is that the cancerous cells are more deformable [44]. A full study of collective migration using multiple droplets would be technically possible, but the required time and computational resources required would make this unfeasible, with the current code.

5.2.3.3 3D model in channel

Given additional time and resources, it would be interesting to extend this model to the 3D case. As seen in Whitfield and Hawkins [72] linear stability analysis of the deformation of 3D active droplets, different and more varied deformations are observed compared to the 2D case. The implicit assumption of axisymmetry in the

3rd dimension is removed for the full 3D case opening up numerous possibilities. It also opens up the possibility of more complex wall geometry and confinement.

Appendix A

Discussion of parameters

Here we describe our choice of parameters for the model and discuss the reasoning behind them. For the grid spacing for the hydrodynamic stokes solver we used a grid spacing of $h = 0.05$ and a grid size of multiples of 120 points as this has 3 prime factors which helps to speed up the FFT algorithm. The spacing of boundary points for the droplet was $ds = h/2$ and the spacing of lattice points for walls is $< h >$. The timestep used is, $\Delta t = 10^-3$. We use the undeformed droplet radius, R_0, the droplet viscosity $\eta^{(int)}$ and the bare droplet boundary tension, γ_0, to set the time, length and energy scales in the system.

A.1 Droplet parameters

Parameter	Simulation value	SI Units
Undeformed droplet radius, R_0	1	10μm
Internal viscosity, $\eta^{(int)}$	$[10, 10^3]$	$[10^2, 10^4]$ Pas
External viscosity $\eta^{(ext)}$	$[10, 10^3]$	$[10^2, 10^4]$ Pas
Boundary diffusion constant, D	0.1	$1\mu\text{m}^2\text{s}^-1$
Initial concentration, c_0	100	$10\mu\text{m}^-1$
Bare Tension, γ_0	10	$100\text{Pa}\mu\text{m}$
Activity, $\zeta\Delta\mu$	$[-15, 0.1]$	$[-1.5 \times 10^4, -10^2]$ Paμm^2

Table A.1: Droplet Parameters

A.1.1 Radius

This project was motivated by the migration of breast cancer cells, specifically the MDA-MB-231 cell line. The measured diameter of these cells is $\sim 20\mu$m [118], as such we chose a value of 10 μm for the droplet radius R_0.

A.1.2 Viscosity

We have 2 viscosities in our system, the internal droplet viscosity $\eta^(int)$ which is the viscosity of the actin-cytoskeleton of the cell. The external viscosity represents the medium in which the cell is moving in. For cells moving in the extracellular matrix the composition of the microenvironment will heavily affect the viscosity of the fluid in which the collagen networks are embedded, and it will be highly dependent on the tissue type. The GAGs present in the ECM form a hydrogel like substance [4]. As discussed in section 2.3. We take a value of 10^4 Pas from [88] as our upper limit and set the lower limit to 10^2. We use the same range for the external viscosity, although constraining it to not be larger than the internal viscosity. These values are at the

high end of estimated realistic values but have the advantage of increased stability in the simulations.

A.1.3 Tension, γ_0

Here γ_0 models the tension of the membrane and actin cortex without the presence of myosin. The measured tension of the cortex differs between cell types upto 2 orders of magnitude from $\sim 10\text{pN}\mu\text{m}^{-1}$ to $\sim\ 1000\text{pN}\mu\text{m}^{-1}$[13]. In [119], tension of fibroblasts was measured with micropipette aspiration, to be $\sim 400\text{pN}\mu\text{m}^{-1}$. When the cells were treated with blebbistatin the tension decreased to $\sim 200\text{pN}\mu\text{m}^{-1}$. From this and bearing in mind that cancer cells are softer than non-cancerous cells we choose a value of $100\text{pN}\mu\text{m}^{-1}$ as out base cell tension.

A.1.4 Concentration

To estimate the concentration of active particles - here representing myosin filaments - we make the assumption that there is one myosin filament per 100 nm, which is the approximate mesh size for the cortex [13]. This gives us a concentration of $10\mu\text{m}^{-}1$.

A.2 Wall Parameters

Parameter	Simulation value	SI Units
Spring constant, k	$[10^4, 10^6]$	$[10^3, 10^5]$ Paμm
Effective elastic modulus, E	$[10^3 - 10^4]$	$[10^3 - 10^4]$ Pa

Table A.2: Wall Parameters

The wall models were built to be a general model for an elastic material, as such we chose spring constants k which exhibited a range of stiffness, such that we had rigid and deformable cases.

Appendix B

Predicting tumour outgrowth from initial cancer cell populations

The following work was published in [1] to model the probability of a tumour developing based on some initial population of cancer cells. We reproduce it here:

We are interested in how initial cell population size affects the probability of developing a tumour. We define the probability of all cancer cells eventually dying out as $P(\text{Extinction})$ and then the probability of a tumour growing is $P(\text{Tumour}) = 1 - P(\text{Extinction})$. We obtain a simple expression for the probability of a tumour in terms of the birth and death rates of a cell as time goes to infinity. In the following we present three methods which give the same expression for $P(\text{Tumour})$ and then in section B.4 we compare our theoretical prediction with our experimentally observed data.

B.1 Continuous time Markov chain

The first method we present treats the population dynamics as a continuous time Markov process. In other words, we assume that the number of cells at time $t + \delta t$ depends only on the birth and death rates and the number of cells at time t i.e. it is independent of previous steps in the process. We define $N(t)$ as the random variable describing the state of the system, which is the number of individuals (cells) in a population at time t. We denote the birth rate for an individual as λ and the death rate as μ. We consider a small time step δt within which the probability of each individual giving birth is $\lambda\delta t + o(\delta t)$ and $\mu\delta t + o(\delta t)$ for the probability of death. $o(\delta t)$ is the probability of more than one event occurring during the interval δt which is always smaller than the probability of one event happening. Finally, the probability of an individual neither reproducing nor dying in the time δt is $1 - (\lambda + \mu)\delta t + o(\delta t)$ [120]. From these probabilities we can construct the difference equation for the probability $p_{n\,m}(t)$ of a population with initial $N(0) = n$ cells having $N(t) = m$ cells at time t as:

$$p_{n\,m}(t + \delta t) = \lambda(m-1)p_{n\,(m-1)}(t)\delta t + \mu(m+1)p_{n\,(m+1)}(t)\delta t + (1 - (\lambda + \mu)m)p_{n\,m}(t)\delta t + o(\delta t) \quad \text{(B.1)}$$

In the limit $\delta t \to 0$, we obtain the differential Kolmogorov forward equation [121]:

$$\frac{\mathrm{d}p_{n\,m}(t)}{\mathrm{d}t} = \lambda(m-1)p_{n\,(m-1)}(t) + \mu(m+1)p_{n\,(m+1)}(t) - (\lambda + \mu)m\,p_{n\,m}(t) \quad \text{(B.2)}$$

$$\frac{\mathrm{d}p_{n\,0}(t)}{\mathrm{d}t} = \mu\,p_{n\,1}(t) \quad \text{(B.3)}$$

We can write (B.2) and (B.3) in matrix form where $p_{n\,m}$ forms a matrix of transition probabilities [122].
The probability generating function Π_n, for a population with initial condition $N(0) = n$ is defined as [123]:

$$\Pi_n(z,t) = \sum_{m=0}^{\infty} p_{n\,m}(t) z^m, \tag{B.4}$$

where z is some real number of cells. Writing out the summation we can see:

$$\begin{aligned} \Pi_n(z,t) &= p_{n\,0}(t) + p_{n\,1}(t)z + p_{n\,2}(t)z^2 ... \\ \Rightarrow \Pi_n(0,t) &= p_{n\,0}(t) = P(N(t) = 0). \end{aligned} \tag{B.5}$$

So to find the extinction probability of our population we first find an expression for Π_n.
We multiply equation B.2 by z^m and sum over $0 \leq m < \infty$ and use the following expression to obtain a differential equation for Π_n.

$$\frac{\partial \Pi_n}{\partial z} = \sum_{m=1}^{\infty} m\, p_{n\,m} z^{m-1}, \tag{B.6}$$

giving,

$$\frac{\partial \Pi_n(z,t)}{\partial t} = (\lambda z^2 - (\lambda + \mu)z + \mu)\frac{\partial \Pi_n(z,t)}{\partial z}. \tag{B.7}$$

We recognise that this is in the form of a Lagrange partial differential equation and write the auxiliary equation:

$$\frac{\mathrm{d}z}{f} = \frac{\mathrm{d}t}{g} = \frac{\mathrm{d}\Pi_n}{h}, \tag{B.8}$$

where $g = 1, h = 0$ and $f = -(\lambda z^2 - (\lambda + \mu)z + \mu)$.

In the case that $\lambda \neq \mu$, using our initial condition $N(0) = n$, then $p_{n\,m}(0) = \delta_{nm}$ and $\Pi_n(z,0) = \sum_{m=0}^{\infty} p_{n\,m}(0) z^m = z^n$, we obtain an expression for Π_n :

$$\Pi_n(z,t) = \left(\frac{\mu(1-z) - (\mu - \lambda z)e^{(\mu-\lambda)t}}{\lambda(1-z) - (\mu - \lambda z)e^{(\mu-\lambda)t}} \right)^n. \tag{B.9}$$

Repeating this process for $\lambda = \mu$ we get:

$$\Pi_n(z,t) = \left(\frac{\lambda t - z\lambda t + z}{\lambda t - z\lambda t + 1} \right)^n. \tag{B.10}$$

Equation (B.5) gives us an expression for the probability of our population size going to zero:

$$P(N(t) = 0) = \begin{cases} \left(\dfrac{\mu - \mu e^{(\mu-\lambda)t}}{\lambda - \mu e^{(\mu-\lambda)t}} \right)^n, & \text{if } \lambda \neq \mu \\ \left(\dfrac{\lambda t}{\lambda t + 1} \right)^n, & \text{if } \lambda = \mu. \end{cases} \tag{B.11}$$

When $t \to \infty$:

$$P(\text{Extinction}) = \lim_{t\to\infty} P(N(t) = 0) = \begin{cases} 1, & \text{if } \lambda \leq \mu \\ \left(\frac{\mu}{\lambda}\right)^n, & \text{if } \lambda > \mu. \end{cases} \tag{B.12}$$

An equivalent solution when treating time discretely can be obtained using a random walk method.

B.2 Branching Process

The second method we present is to consider our system as a branching process. At each generation a cell has the probability of producing 0, 1 or 2 offspring and then dying. We are only interested in the size of the new generation. This maps onto a situation where at each discrete time step a cell either dies, does nothing or reproduces. For a population initially consisting of $N(0) = n = 1$ cell:

$$P(\text{Extinction}) = \Theta = \lim_{t\to\infty} P\left(N(t) = 0 \middle| N(0) = 1\right). \tag{B.13}$$

Let the probability of $0, 1, 2$ offspring be denoted by p_0, p_1, p_2, then intuitively we can see that the probability of the lineage of a cell dying out is equal to the probability of the initial cell dying, p_0, plus the probability of producing 1 offspring and all of that offspring's lineage dying, $p_1\Theta$, plus the probability of the cell producing 2 offspring who's lineages both die $p_2\Theta^2$. This results in a recursive equation in Θ (for a more detailed derivation see [124]).

$$\Theta = p_0 + p_1\Theta + p_2\Theta^2 + \dots \tag{B.14}$$

We recognise that the right hand side of (B.14) is in the form of the probability generating function for Θ, $\Pi(\Theta)$.
The probability of extinction is given by the smallest root of equation (B.14). $\Theta = 1$ is always a root, but not necessarily the smallest [124]. In our case we find roots:

$$\Theta_1 = 1 \qquad \Theta_2 = \frac{p_0}{p_2}. \tag{B.15}$$

The probability of extinction for $n = 1$ initial cell is certain if the probability of death is greater or equal to the probability of birth, otherwise it is given by $\frac{p_0}{p_2}$.
If we assume independence of events, for a population with n cells at $t = 0$ (i.e. $N(0) = n$) then:

$$P(\text{Extinction}) = \lim_{t\to\infty} P\left(N(t) = 0 \middle| N(0) = n\right) = \Theta^n. \tag{B.16}$$

Redefining $p_0 = \mu, p_2 = \lambda$ to be consistent with the notation used in section B.1, we recover our result given in equation (B.12):

$$P(\text{Extinction}) = \begin{cases} 1, & \text{if } \lambda \leq \mu \\ \left(\frac{\mu}{\lambda}\right)^n, & \text{if } \lambda > \mu. \end{cases} \tag{B.17}$$

B.3 Combinatorial probability series

The final method we present is to build up a series in which each term is the probability that all cells die given a certain number, n_r, of births. Each term is given by the negative binomial distribution for n_r births before n_d deaths, given by;

$$P(n_r, n_d) = \frac{(n_r + n_d - 1)!}{n_r!(n_d - 1)!} p_d^{n_d} (1 - p_d)^{n_r},$$

where p_d is the probability of death. We assume that every cell eventually either dies or gives birth, hence $p_r = 1 - p_d$ is the probability of birth.
We want to calculate the probability, $P(\text{Extinction})$, that all cells eventually die in a cluster of initial size n cells. If there are n_r births then extinction of the cluster requires $n_d = n + n_r$ deaths. However, the number of ways this can occur requires conditions on the order of births and deaths. If there are n_r births these must occur before all the cells have died. We consider the process in stages. Firstly we consider the number of ways of having n_{r_1} births before n deaths i.e. the number of ways to have n_{r_1} births before the original number n of cells in the cluster have died:

$$\Omega(n_{r_1}, n) = \frac{(n_{r_1} + n - 1)!}{n_{r_1}!(n - 1)!}. \tag{B.18}$$

Since initially the only deaths possible are those of the initial n cells we need to multiply this by the fraction of deaths that are those of original cells i.e. by $n/(n+n_r)$. Next we count the number of ways of having the remaining $(n_r - n_{r_1})$ births before the next n_r deaths.

$$\Omega(n_r - n_{r_1}, n_r) = \frac{(2n_r - n_{r_1} - 1)!}{(n_r - n_{r_1})!(n_r - 1)!}. \tag{B.19}$$

After these n_r births and $n + n_r - 2$ deaths, the final two events must be deaths. Combining this with equations (B.18) and (B.19) and summing over the possible values of the number of births in the initial stage, n_{r_1} from zero to the total number of births, n_r gives;

$$P(\text{Extinction}|n_r \text{ births}) = \sum_{n_{r_1}=0}^{n_r} \frac{n}{n + n_r} \Omega(n_{r_1}, n)\Omega(n_r - n_{r_1}, n_r) p_d^{n+n_r} (1 - p_d)^{n_r}.$$

The total extinction probability is then given by the sum of this over the possible values of n_r from zero to infinity;

$$\begin{aligned} P(\text{Extinction}) &= \sum_{n_r=0}^{\infty} \sum_{n_{r_1}=0}^{n_r} \frac{n}{n + n_r} \Omega(n_{r_1}, n)\Omega(n_r - n_{r_1}, n_r) p_d^{n+n_r} (1 - p_d)^{n_r} \\ &= \sum_{n_r=0}^{\infty} \frac{n(2n_r + n - 1)!}{n_r!(n_r + n)!} p_d^{n+n_r} (1 - p_d)^{n_r} \\ &= {}_2F_1\left(\frac{n}{2}, \frac{n+1}{2}, n + 1, 4p_d(1 - p_d)\right) p_d^n, \end{aligned} \tag{B.20}$$

where ${}_2F_1$ is the hypergeometric function. The hypergeometric function in equation (B.20) can be transformed to **Goursat1881**

$$P(\text{Extinction}) = {}_2F_1(n, n{+}1, n{+}1, p_d))p_d^n = (1{-}p_d)^{-n}p_d^n = \left(\frac{p_d}{p_r}\right)^n = \left(\frac{\mu}{\lambda}\right)^n. \quad \text{(B.21)}$$

Recognising that $\frac{p_d}{p_r} = \frac{\mu}{\lambda}$ we recover the same result as in section B.1 and B.2.

B.4 Comparing our predictions to data

From our calculations above we know for long time scales the probability of a tumour is zero if the death rate of the cells is greater than or equal the birth rate. If the birth rate is greater than the death rate we have:

$$P(\text{Tumour}) = 1 - \left(\frac{\mu}{\lambda}\right)^n. \quad \text{(B.22)}$$

In Figure B.1(a) we plot this tumour probability as a function of the initial number of cells, n. Notably the curve is sub-linear, with a rapid increase at small values of n and levelling off at larger values of n where the probability of a tumour tends towards certainty, i.e. $P(\text{Tumour}) = 1$, for large enough n. To simplify the notation to that used in the main text of this article, we redefine the ratio of death over birth rates as $\frac{\mu}{\lambda} = A$. We do not know what the value of this ratio of rates is experimentally. However, in the following we use the experimental data we do have to compare to equation B.22.

From our data the mean number of tumour cells for 6 week old mice is $m_y = 103 \pm 10$ and the mean number of tumour cells for 12 week old mice is $m_o = 36 \pm 3$, where here the error is the standard error of the mean. Using data from the supplementary information in [125], the fraction of 6 week mice with a tumour is 0.9, compared to 0.2 in 12 week mice. The number of mice used in the study is not stated so we assume a ± 0.05 error on the quoted fractions. Using this data we can solve equation B.22 for $A = \frac{\mu}{\lambda}$ i.e.

$$1 - A_y^{m_y} = 0.9 \quad \text{(B.23)}$$

$$1 - A_o^{m_o} = 0.2, \quad \text{(B.24)}$$

giving $A_y = 0.978, A_o = 0.994$. If we could completely explain the tumour probability with cell population statistics alone then we would expect $A_y = A_o$. There is, however, a degree of uncertainty in our numbers, so we plot in Figure B.1(a) the curves obtained from solving for A_y, A_o including an upper and lower bound based on errors. We see there is no overlap in these regions.

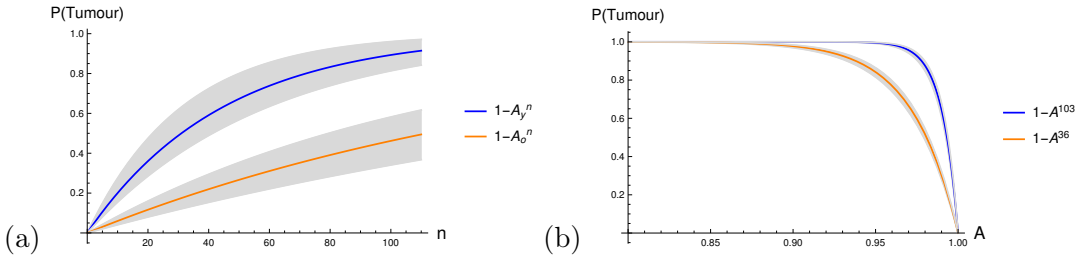

FIGURE B.1: (a) Plot of the probability of a tumour against the initial number of cells, n. Upper and lower bounds found by calculating the ratio of death over birth rates, $A = \frac{\mu}{\lambda}$, from equations (B.23-B.24) using $m_o = 36 \pm 3, m_y = 103 \pm 10$ and assuming an uncertainty of ± 0.05 on P(Tumour). Here $A_y = 0.978, A_o = 0.994$. The upper (blue) curve corresponds to 6 week old mice and the lower (orange) curve to 12 week old mice. (b) Plot of the probability of a tumour against the ratio of death over birth rates, $A = \frac{\mu}{\lambda}$. Upper and lower bounds calculated using $m_y = 103 \pm 10, m_o, = 36 \pm 3$.

In Figure B.1(b) we plot our expression for P(Tumour) against the ratio of death to birth rate, $A = \frac{\mu}{\lambda}$, for the initial populations m_y, m_o. We see that the ratio of death to birth here is only the same when it is certain that there will be a tumour or not, i.e. for P(Tumour) $= 1$ or 0.

In the analysis we have presented in Figure B.1 we assumed that all the tumour cells observed in the mouse bone are able to proliferate and die with the same rates. However, there is evidence that only a subset of the population of MDA-MB-231 DTCs have the ability to form metastatic tumours in the bone. We also note that stochastic effects will be more prominent for small numbers of initial cells. Taking the figure 11% from [126], we again solve for A_y, A_o, and plot the resultant curves in Figure B.2(a). We see a much steeper initial curve which plateaus to certainty of a tumour much earlier than in the case of the total population in Figure B.1(a), indicating greater sensitivity to the initial number of cells. Comparing figures B.1(b) and B.2(b), it can

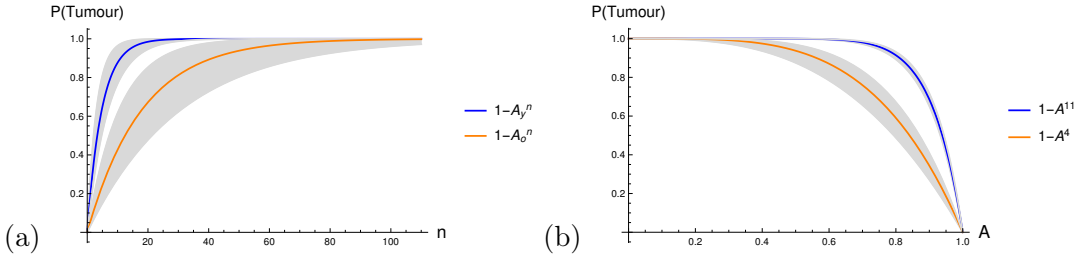

FIGURE B.2: (a) Plot of the probability of a tumour against the initial number of cells, n. Upper and lower bounds calculated using $m_y = 11 \pm 2, m_o, = 4 \pm 1$, where errors have been rounded up to the next integer and assuming an uncertainty of ± 0.05 on P(Tumour). Here $A_y = 0.811, A_o = 0.946$. (b) Plot of the probability of a tumour against the ratio of death and birth rates. Upper and lower bounds calculated using $m_y = 11 \pm 2, m_o, = 4 \pm 1$.

be seen that differences in tumour probability between the cases with different initial number of cells (blue/orange curves) appear for a much lower death to birth rate ratio, A, in the sub-population (Fig B.2(b)) compared to the total population of initial cells

(Fig B.1(b)). This demonstrates the prominence of stochastic effects for small numbers of cells.
We briefly considered if cell were in clusters, but as we have assumed all birth and death events are independent only the initial number matters regardless of the spatial configuration they are in.
Comparing our model to the data indicates that the tumour probabilities we see cannot be explained by statistics alone and that there may be some additional environmental factor or interdependence of events.

References

[1] R. Hughes, X. Chen, N. Cowley, P. D. Ottewell, R. J. Hawkins, K. D. Hunter, J. K. Hobbs, N. J. Brown and I. Holen, 'Osteoblast-derived paracrine and juxtacrine signals protect disseminated breast cancer cells from stress', *Cancers*, vol. 13, no. 6, p. 1366, 2021.

[2] D. A. Fletcher and R. D. Mullins, 'Cell mechanics and the cytoskeleton', *Nature*, vol. 463, no. 7280, pp. 485–492, 2010.

[3] H. Lodish, A. Berk, C. A. Kaiser, C. Kaiser, M. Krieger, M. P. Scott, A. Bretscher, H. Ploegh, P. Matsudaira *et al. Molecular cell biology*. Macmillan, 2008.

[4] B. Alberts. *Molecular Biology of the Cell with CD*. Garland, 2008.

[5] C. Leduc and S. Etienne-Manneville, 'Intermediate filaments in cell migration and invasion: the unusual suspects', *Current opinion in cell biology*, vol. 32, pp. 102–112, 2015.

[6] E. W. Flitney, E. R. Kuczmarski, S. A. Adam and R. D. Goldman, 'Insights into the mechanical properties of epithelial cells: the effects of shear stress on the assembly and remodeling of keratin intermediate filaments', *The FASEB Journal*, vol. 23, no. 7, pp. 2110–2119, 2009.

[7] M. L. Gardel, K. E. Kasza, C. P. Brangwynne, J. Liu and D. A. Weitz, 'Mechanical response of cytoskeletal networks', *Methods in cell biology*, vol. 89, pp. 487–519, 2008.

[8] P. M. Steinert, 'Structure, function, and dynamics of keratin intermediate filaments', *Journal of Investigative Dermatology*, vol. 100, no. 6, pp. 729–734, 1993.

[9] E. J. van Bodegraven and S. Etienne-Manneville, 'Intermediate filaments against actomyosin: the david and goliath of cell migration', *Current Opinion in Cell Biology*, vol. 66, pp. 79–88, 2020.

[10] M. Schliwa and G. Woehlke, 'Molecular motors', *Nature*, vol. 422, no. 6933, pp. 759–765, 2003.

[11] P. Chugh and E. K. Paluch, 'The actin cortex at a glance', *Journal of Cell Science*, vol. 131, no. 14, jcs186254, 2018.

[12] P. Chugh, A. G. Clark, M. B. Smith, D. A. Cassani, K. Dierkes, A. Ragab, P. P. Roux, G. Charras, G. Salbreux and E. K. Paluch, 'Actin cortex architecture regulates cell surface tension', *Nature cell biology*, vol. 19, no. 6, pp. 689–697, 2017.

[13] G. Salbreux, G. Charras and E. Paluch, 'Actin cortex mechanics and cellular morphogenesis', *Trends in cell biology*, vol. 22, no. 10, pp. 536–545, 2012.

[14] M. C. Marchetti, J. Joanny, S. Ramaswamy, T. Liverpool, J. Prost, M. Rao and R. A. Simha, 'Hydrodynamics of soft active matter', *Reviews of Modern Physics*, vol. 85, no. 3, p. 1143, 2013.

[15] E. D. Korn, M.-F. Carlier and D. Pantaloni, 'Actin polymerization and atp hydrolysis', *Science*, vol. 238, no. 4827, pp. 638–645, 1987.

[16] M. A. Rould, Q. Wan, P. B. Joel, S. Lowey and K. M. Trybus, 'Crystal structures of expressed non-polymerizable monomeric actin in the adp and atp states', *Journal of Biological Chemistry*, vol. 281, no. 42, pp. 31 909–31 919, 2006.

[17] J. Condeelis, 'Life at the leading edge: the formation of cell protrusions', *Annual review of cell biology*, vol. 9, no. 1, pp. 411–444, 1993.

[18] C. S. Peskin, G. M. Odell and G. F. Oster, 'Cellular motions and thermal fluctuations: the brownian ratchet', *Biophysical journal*, vol. 65, no. 1, pp. 316–324, 1993.

[19] A. Mogilner and G. Oster, 'Cell motility driven by actin polymerization', *Biophysical journal*, vol. 71, no. 6, pp. 3030–3045, 1996.

[20] P. M. Bendix, G. H. Koenderink, D. Cuvelier, Z. Dogic, B. N. Koeleman, W. M. Brieher, C. M. Field, L. Mahadevan and D. A. Weitz, 'A quantitative analysis of contractility in active cytoskeletal protein networks', *Biophysical journal*, vol. 94, no. 8, pp. 3126–3136, 2008.

[21] K. Takiguchi, 'Heavy meromyosin induces sliding movements between anti-parallel actin filaments', *Journal of biochemistry*, vol. 109, no. 4, pp. 520–527, 1991.

[22] K. Kruse, A. Zumdieck and F. Jülicher, 'Continuum theory of contractile fibres', *EPL (Europhysics Letters)*, vol. 64, no. 5, p. 716, 2003.

[23] K. Kruse and F. Jülicher, 'Self-organization and mechanical properties of active filament bundles', *Physical Review E*, vol. 67, no. 5, p. 051 913, 2003.

[24] A. E. Carlsson, 'Contractile stress generation by actomyosin gels', *Physical Review E*, vol. 74, no. 5, p. 051 912, 2006.

[25] M. Lenz, T. Thoresen, M. L. Gardel and A. R. Dinner, 'Contractile units in disordered actomyosin bundles arise from f-actin buckling', *Physical review letters*, vol. 108, no. 23, p. 238 107, 2012.

[26] M. Lenz, M. L. Gardel and A. R. Dinner, 'Requirements for contractility in disordered cytoskeletal bundles', *New journal of physics*, vol. 14, no. 3, p. 033 037, 2012.

[27] T. B. Liverpool, M. C. Marchetti, J.-F. Joanny and J. Prost, 'Mechanical response of active gels', *EPL (Europhysics Letters)*, vol. 85, no. 1, p. 18 007, 2009.

[28] R. J. Hawkins and T. B. Liverpool, 'Stress reorganization and response in active solids', *Physical review letters*, vol. 113, no. 2, p. 028 102, 2014.

[29] T. M. Svitkina, A. B. Verkhovsky, K. M. McQuade and G. G. Borisy, 'Analysis of the actin–myosin ii system in fish epidermal keratocytes: mechanism of cell body translocation', *The Journal of cell biology*, vol. 139, no. 2, pp. 397–415, 1997.

[30] O. Medalia, I. Weber, A. S. Frangakis, D. Nicastro, G. Gerisch and W. Baumeister, 'Macromolecular architecture in eukaryotic cells visualized by cryoelectron tomography', *Science*, vol. 298, no. 5596, pp. 1209–1213, 2002.

[31] E. Paluch, C. Sykes, J. Prost and M. Bornens, 'Dynamic modes of the cortical actomyosin gel during cell locomotion and division', *Trends in cell biology*, vol. 16, no. 1, pp. 5–10, 2006.

[32] S. Wang and P. G. Wolynes, 'Active contractility in actomyosin networks', *Proceedings of the National Academy of Sciences*, vol. 109, no. 17, pp. 6446–6451, 2012.

[33] P. G. De Gennes and J. Prost. *The physics of liquid crystals*, 83. Oxford university press, 1995.

[34] F. Juelicher, K. Kruse, J. Prost and J.-F. Joanny, 'Active behavior of the cytoskeleton', *Physics Reports*, vol. 449, no. 1, pp. 3–28, 2007.

[35] J.-F. Joanny and J. Prost, 'Active gels as a description of the actin-myosin cytoskeleton', *HFSP journal*, vol. 3, no. 2, pp. 94–104, 2009.

[36] K. Kruse, J.-F. Joanny, F. Jülicher, J. Prost and K. Sekimoto, 'Asters, vortices, and rotating spirals in active gels of polar filaments', *Physical review letters*, vol. 92, no. 7, p. 078 101, 2004.

[37] K. Kruse, J.-F. Joanny, F. Jülicher, J. Prost and K. Sekimoto, 'Generic theory of active polar gels: a paradigm for cytoskeletal dynamics', *The European Physical Journal E*, vol. 16, no. 1, pp. 5–16, 2005.

[38] B. Fabry, G. N. Maksym, J. P. Butler, M. Glogauer, D. Navajas and J. J. Fredberg, 'Scaling the microrheology of living cells', *Physical review letters*, vol. 87, no. 14, p. 148 102, 2001.

[39] R. B. Bird, R. C. Armstrong, O. Hassager and C. F. Curtiss. *Dynamics of polymeric liquids*. Wiley New York, 1977, vol. 1.

[40] C. Frantz, K. M. Stewart and V. M. Weaver, 'The extracellular matrix at a glance', *Journal of cell science*, vol. 123, no. 24, pp. 4195–4200, 2010.

[41] T. J. McKee, G. Perlman, M. Morris and S. V. Komarova, 'Extracellular matrix composition of connective tissues: a systematic review and meta-analysis', *Scientific reports*, vol. 9, no. 1, pp. 1–15, 2019.

[42] P. Fratzl. 'Collagen: structure and mechanics, an introduction', in *Collagen*, Springer, 2008, pp. 1–13.

[43] E. Sahai, 'Mechanisms of cancer cell invasion', *Current opinion in genetics & development*, vol. 15, no. 1, pp. 87–96, 2005.

[44] R. Weinberg. *The biology of cancer*. Garland science, 2013.

[45] G. R. Mundy, 'Metastasis: metastasis to bone: causes, consequences and therapeutic opportunities', *Nature Reviews Cancer*, vol. 2, no. 8, pp. 584–593, 2002.

[46] K. Vleminckx, L. Vakaet, M. Mareel, W. Fiers and F. Van Roy, 'Genetic manipulation of e-cadherin expression by epithelial tumor cells reveals an invasion suppressor role', *Cell*, vol. 66, no. 1, pp. 107–119, 1991.

[47] A. Satelli and S. Li, 'Vimentin in cancer and its potential as a molecular target for cancer therapy', *Cellular and molecular life sciences*, vol. 68, no. 18, pp. 3033–3046, 2011.

[48] M. R. Rogel, P. N. Soni, J. R. Troken, A. Sitikov, H. E. Trejo and K. M. Ridge, 'Vimentin is sufficient and required for wound repair and remodeling in alveolar epithelial cells', *The FASEB Journal*, vol. 25, no. 11, pp. 3873–3883, 2011.

[49] K. Seltmann, A. W. Fritsch, J. A. Käs and T. M. Magin, 'Keratins significantly contribute to cell stiffness and impact invasive behavior', *Proceedings of the National Academy of Sciences*, vol. 110, no. 46, pp. 18 507–18 512, 2013.

[50] K. Nabeshima, T. Inoue, Y. Shimao and T. Sameshima, 'Matrix metalloproteinases in tumor invasion: role for cell migration', *Pathology international*, vol. 52, no. 4, pp. 255–264, 2002.

[51] K. Paňková, D. Rösel, M. Novotn and J. Brábek, 'The molecular mechanisms of transition between mesenchymal and amoeboid invasiveness in tumor cells', *Cellular and molecular life sciences*, vol. 67, no. 1, pp. 63–71, 2010.

[52] D. A. Lauffenburger and A. F. Horwitz, 'Cell migration: a physically integrated molecular process', *Cell*, vol. 84, no. 3, pp. 359–369, 1996.

[53] R. J. Petrie and K. M. Yamada, 'Fibroblasts lead the way: a unified view of 3d cell motility', *Trends in cell biology*, vol. 25, no. 11, pp. 666–674, 2015.

[54] E. K. Paluch, I. M. Aspalter and M. Sixt, 'Focal adhesion–independent cell migration', *Annual review of cell and developmental biology*, vol. 32, pp. 469–490, 2016.

[55] K. M. Yamada and M. Sixt, 'Mechanisms of 3d cell migration', *Nature Reviews Molecular Cell Biology*, vol. 20, no. 12, pp. 738–752, 2019.

[56] A. Fruleux and R. J. Hawkins, 'Physical role for the nucleus in cell migration', *Journal of Physics: Condensed Matter*, vol. 28, no. 36, p. 363 002, 2016.

[57] R. Poincloux, O. Collin, F. Lizárraga, M. Romao, M. Debray, M. Piel and P. Chavrier, 'Contractility of the cell rear drives invasion of breast tumor cells in 3d matrigel', *Proceedings of the National Academy of Sciences*, vol. 108, no. 5, pp. 1943–1948, 2011.

[58] R. J. Hawkins, R. Poincloux, O. Bénichou, M. Piel, P. Chavrier and R. Voituriez, 'Spontaneous contractility-mediated cortical flow generates cell migration in three-dimensional environments', *Biophysical Journal*, vol. 101, no. 5, pp. 1041–1045, 2011.

[59] R. J. Petrie, N. Gavara, R. S. Chadwick and K. M. Yamada, 'Nonpolarized signaling reveals two distinct modes of 3d cell migration', *Journal of Cell Biology*, vol. 197, no. 3, pp. 439–455, 2012.

[60] R. J. Hawkins, M. Piel, G. Faure-Andre, A. Lennon-Dumenil, J. Joanny, J. Prost and R. Voituriez, 'Pushing off the walls: a mechanism of cell motility in confinement', *Physical review letters*, vol. 102, no. 5, p. 058 103, 2009.

[61] V. Ruprecht, S. Wieser, A. Callan-Jones, M. Smutny, H. Morita, K. Sako, V. Barone, M. Ritsch-Marte, M. Sixt, R. Voituriez *et al.*, 'Cortical contractility triggers a stochastic switch to fast amoeboid cell motility', *Cell*, vol. 160, no. 4, pp. 673–685, 2015.

[62] E. M. Purcell, 'Life at low reynolds number', *American journal of physics*, vol. 45, no. 1, pp. 3–11, 1977.

[63] M. Lighthill, 'On the squirming motion of nearly spherical deformable bodies through liquids at very small reynolds numbers', *Communications on pure and applied mathematics*, vol. 5, no. 2, pp. 109–118, 1952.

[64] H. Lamb. *Hydrodynamics*. University Press, 1924.

[65] E. Lauga. *The Fluid Dynamics of Cell Motility*. Cambridge University Press, 2020, vol. 62.

[66] P. Ahana and S. P. Thampi, 'Confinement induced trajectory of a squirmer in a two dimensional channel', *Fluid Dynamics Research*, vol. 51, no. 6, p. 065 504, 2019.

[67] E. Tjhung, D. Marenduzzo and M. E. Cates, 'Spontaneous symmetry breaking in active droplets provides a generic route to motility', *Proceedings of the National Academy of Sciences*, vol. 109, no. 31, pp. 12 381–12 386, 2012.

[68] C. A. Whitfield, D. Marenduzzo, R. Voituriez and R. J. Hawkins, 'Active polar fluid flow in finite droplets', *The European Physical Journal E*, vol. 37, no. 2, pp. 1–15, 2014.

[69] W. Marth, S. Praetorius and A. Voigt, 'A mechanism for cell motility by active polar gels', *Journal of The Royal Society Interface*, vol. 12, no. 107, p. 20 150 161, 2015.

[70] L. Giomi and A. DeSimone, 'Spontaneous division and motility in active nematic droplets', *Physical review letters*, vol. 112, no. 14, p. 147 802, 2014.

[71] L. J. Ruske and J. M. Yeomans, 'Morphology of active deformable 3d droplets', *Physical Review X*, vol. 11, no. 2, p. 021 001, 2021.

[72] C. A. Whitfield and R. J. Hawkins, 'Instabilities, motion and deformation of active fluid droplets', *New Journal of Physics*, vol. 18, no. 12, p. 123 016, 2016.

[73] A. Farutin, J. Etienne, C. Misbah and P. Recho, 'Crawling in a fluid', *Physical review letters*, vol. 123, no. 11, p. 118 101, 2019.

[74] M. Schmitt and H. Stark, 'Marangoni flow at droplet interfaces: three-dimensional solution and applications', *Physics of Fluids*, vol. 28, no. 1, p. 012 106, 2016.

[75] ——, 'Swimming active droplet: a theoretical analysis', *EPL (Europhysics Letters)*, vol. 101, no. 4, p. 44 008, 2013.

[76] N. Yoshinaga, 'Spontaneous motion and deformation of a self-propelled droplet', *Physical Review E*, vol. 89, no. 1, p. 012 913, 2014.

[77] M. Morozov and S. Michelin, 'Self-propulsion near the onset of marangoni instability of deformable active droplets', *Journal of Fluid Mechanics*, vol. 860, pp. 711–738, 2019.

[78] C. Pozrikidis. *Modeling and simulation of capsules and biological cells*. CRC Press, 2003.

[79] C. A. Whitfield. 'Modelling spontaneous motion and deformation of active droplets', PhD thesis, University of Sheffield, 2015.

[80] C. S. Peskin, 'The immersed boundary method', *Acta numerica*, vol. 11, pp. 479–517, 2002.

[81] J. M. McDonough, 'Lectures in computational fluid dynamics of incompressible flow: mathematics, algorithms and implementations', 2007.

[82] A. J. Chorin, 'Numerical solution of the navier-stokes equations', *Mathematics of computation*, vol. 22, no. 104, pp. 745–762, 1968.

[83] R. Temam, 'Sur l'approximation de la solution des équations de navier-stokes par la méthode des pas fractionnaires (ii)', *Archive for rational mechanics and analysis*, vol. 33, no. 5, pp. 377–385, 1969.

[84] H. v. Helmholtz, 'Lxiii. on integrals of the hydrodynamical equations, which express vortex-motion', *The London, Edinburgh, and Dublin Philosophical Magazine and Journal of Science*, vol. 33, no. 226, pp. 485–512, 1867.

[85] C. S. Peskin, 'Flow patterns around heart valves: a numerical method', *Journal of computational physics*, vol. 10, no. 2, pp. 252–271, 1972.

[86] M.-C. Lai, Y.-H. Tseng and H. Huang, 'An immersed boundary method for interfacial flows with insoluble surfactant', *Journal of Computational Physics*, vol. 227, no. 15, pp. 7279–7293, 2008.

[87] T. E. Tezduyar, 'Finite element methods for flow problems with moving boundaries and interfaces', *Archives of Computational Methods in Engineering*, vol. 8, no. 2, p. 83, 2001.

[88] F. Wottawah, S. Schinkinger, B. Lincoln, R. Ananthakrishnan, M. Romeyke, J. Guck and J. Käs, 'Optical rheology of biological cells', *Physical review letters*, vol. 94, no. 9, p. 098 103, 2005.

[89] P. Canadas, V. M. Laurent, C. Oddou, D. Isabey and S. Wendling, 'A cellular tensegrity model to analyse the structural viscoelasticity of the cytoskeleton', *Journal of Theoretical Biology*, vol. 218, no. 2, pp. 155–173, 2002.

[90] M. R. Mofrad, 'Rheology of the cytoskeleton', *Annual Review of Fluid Mechanics*, vol. 41, pp. 433–453, 2009.

[91] C. Pozrikidis *et al. Boundary integral and singularity methods for linearized viscous flow*. Cambridge university press, 1992.

[92] S. Kim and S. J. Karrila. *Microhydrodynamics: principles and selected applications*. Courier Corporation, 2013.

[93] S. E. Spagnolie and E. Lauga, 'Hydrodynamics of self-propulsion near a boundary: predictions and accuracy of far-field approximations', *ArXiv preprint arXiv:1211.6996*, 2012.

[94] Y. Itin and S. Reches, 'Decomposition of third-order constitutive tensors', *Mathematics and Mechanics of Solids*, p. 10 812 865 211 016 530, 2020.

[95] S. Kinoshita. *Pattern formations and oscillatory phenomena*. Newnes, 2013.

[96] O. S. Pak and E. Lauga, 'Generalized squirming motion of a sphere', *Journal of Engineering Mathematics*, vol. 88, no. 1, pp. 1–28, 2014.

[97] B. P. Flannery, W. H. Press, S. A. Teukolsky and W. Vetterling, 'Numerical recipes in c', *Press Syndicate of the University of Cambridge, New York*, vol. 24, no. 78, p. 36, 1992.

[98] J. de Graaf, A. J. Mathijssen, M. Fabritius, H. Menke, C. Holm and T. N. Shendruk, 'Understanding the onset of oscillatory swimming in microchannels', *Soft Matter*, vol. 12, no. 21, pp. 4704–4708, 2016.

[99] S. Jana, S. H. Um and S. Jung, 'Paramecium swimming in capillary tube', *Physics of fluids*, vol. 24, no. 4, p. 041 901, 2012.

[100] M. Frigo and S. G. Johnson. *Fftw*, 2003. [Online]. Available: https://www.fftw.org/fftw3.pdf (visited on 19/07/2021).

[101] W. Strychalski, C. A. Copos, O. L. Lewis and R. D. Guy, 'A poroelastic immersed boundary method with applications to cell biology', *Journal of Computational Physics*, vol. 282, pp. 77–97, 2015.

[102] A. F. Bower. *Applied mechanics of solids*. CRC press, 2009.

[103] P. Steinmann, M. Hossain and G. Possart, 'Hyperelastic models for rubber-like materials: consistent tangent operators and suitability for treloar's data', *Archive of Applied Mechanics*, vol. 82, no. 9, pp. 1183–1217, 2012.

[104] C. Wex, S. Arndt, A. Stoll, C. Bruns and Y. Kupriyanova, 'Isotropic incompressible hyperelastic models for modelling the mechanical behaviour of biological tissues: a review', *Biomedical Engineering/Biomedizinische Technik*, vol. 60, no. 6, pp. 577–592, 2015.

[105] G. Chagnon, M. Rebouah and D. Favier, 'Hyperelastic energy densities for soft biological tissues: a review', *Journal of Elasticity*, vol. 120, no. 2, pp. 129–160, 2015.

[106] D. Devendran and C. S. Peskin, 'An immersed boundary energy-based method for incompressible viscoelasticity', *Journal of Computational Physics*, vol. 231, no. 14, pp. 4613–4642, 2012.

[107] B. A. Krajina, B. L. LeSavage, J. G. Roth, A. W. Zhu, P. C. Cai, A. J. Spakowitz and S. C. Heilshorn, 'Microrheology reveals simultaneous cell-mediated matrix stiffening and fluidization that underlie breast cancer invasion', *Science Advances*, vol. 7, no. 8, eabe1969, 2021.

[108] E. H. Barriga, K. Franze, G. Charras and R. Mayor, 'Tissue stiffening coordinates morphogenesis by triggering collective cell migration in vivo', *Nature*, vol. 554, no. 7693, pp. 523–527, 2018.

[109] A. B. Verkhovsky, T. M. Svitkina and G. G. Borisy, 'Self-polarization and directional motility of cytoplasm', *Current Biology*, vol. 9, no. 1, 11–S1, 1999.

[110] A. Elosegui-Artola, 'The extracellular matrix viscoelasticity as a regulator of cell and tissue dynamics', *Current Opinion in Cell Biology*, vol. 72, pp. 10–18, 2021.

[111] A. Shellard and R. Mayor, 'Durotaxis: the hard path from in vitro to in vivo', *Developmental cell*, 2020.

[112] T. G. Fai and C. H. Rycroft, 'Lubricated immersed boundary method in two dimensions', *Journal of Computational Physics*, vol. 356, pp. 319–339, 2018.

[113] M. Le Berre, Y.-J. Liu, J. Hu, P. Maiuri, O. Bénichou, R. Voituriez, Y. Chen and M. Piel, 'Geometric friction directs cell migration', *Physical review letters*, vol. 111, no. 19, p. 198 101, 2013.

[114] A. Reversat, F. Gaertner, J. Merrin, J. Stopp, S. Tasciyan, J. Aguilera, I. De Vries, R. Hauschild, M. Hons, M. Piel *et al.*, 'Cellular locomotion using environmental topography', *Nature*, vol. 582, no. 7813, pp. 582–585, 2020.

[115] M. R. Zanotelli, A. Rahman-Zaman, J. A. VanderBurgh, P. V. Taufalele, A. Jain, D. Erickson, F. Bordeleau and C. A. Reinhart-King, 'Energetic costs regulated by cell mechanics and confinement are predictive of migration path during decision-making', *Nature communications*, vol. 10, no. 1, pp. 1–12, 2019.

[116] H. D. Moreau, C. Blanch-Mercader, R. Attia, M. Maurin, Z. Alraies, D. Sanséau, O. Malbec, M.-G. Delgado, P. Bousso, J.-F. Joanny *et al.*, 'Macropinocytosis overcomes directional bias in dendritic cells due to hydraulic resistance and facilitates space exploration', *Developmental cell*, vol. 49, no. 2, pp. 171–188, 2019.

[117] I. D. Estabrook, H. R. Thiam, M. Piel and R. J. Hawkins, 'Calculation of the force field required for nucleus deformation during cell migration through constrictions', *PLoS computational biology*, vol. 17, no. 5, e1008592, 2021.

[118] S. Connolly, K. McGourty and D. Newport, 'The in vitro inertial positions and viability of cells in suspension under different in vivo flow conditions', *Scientific reports*, vol. 10, no. 1, pp. 1–13, 2020.

[119] J.-Y. Tinevez, U. Schulze, G. Salbreux, J. Roensch, J.-F. Joanny and E. Paluch, 'Role of cortical tension in bleb growth', *Proceedings of the National Academy of Sciences*, vol. 106, no. 44, pp. 18 581–18 586, 2009.

[120] B. J. Morgan, 'Four approaches to solving the linear birth-and-death (and similar) processes', *International Journal of Mathematical Education in Science and Technology*, vol. 10, no. 1, pp. 51–64, 1979.

[121] A. Kolmogoroff, 'Über die analytischen methoden in der wahrscheinlichkeitsrechnung', *Mathematische Annalen*, vol. 104, no. 1, pp. 415–458, 1931.

[122] E. J. McCoy. *Continuous time markov processes*. [Online]. Available: http://wwwf.imperial.ac.uk/~ejm/M3S4/NOTEScurrent.PDF (visited on 09/04/2020).

[123] G. Grimmett, G. R. Grimmett, D. Stirzaker *et al. Probability and random processes*. Oxford university press, 2001.

[124] M. Kimmel and D. E. Axelrod. *Branching Processes in Biology*. Springer New York, 2002. DOI: 10.1007/b97371. [Online]. Available: https://doi.org/10.1007%2Fb97371.

[125] P. D. Ottewell, N. Wang, H. K. Brown, K. J. Reeves, C. A. Fowles, P. I. Croucher, C. L. Eaton and I. Holen, 'Zoledronic acid has differential antitumor activity in the pre-and postmenopausal bone microenvironment in vivo', *Clinical Cancer Research*, vol. 20, no. 11, pp. 2922–2932, 2014.

[126] Y. Kang, P. M. Siegel, W. Shu, M. Drobnjak, S. M. Kakonen, C. Cordón-Cardo, T. A. Guise and J. Massagué, 'A multigenic program mediating breast cancer metastasis to bone', *Cancer cell*, vol. 3, no. 6, pp. 537–549, 2003.